

NMR Investigations on Alkali Intercalated Carbon Nanotubes

Von der Fakultät für Mathematik und Physik
der Universität Stuttgart
zur Erlangung der Würde eines
Doktors der Naturwissenschaften (Dr. rer. nat.)
genehmigte Abhandlung

Vorgelegt von
Michael Schmid
aus Horb-Mühlingen

Prüfungsausschuss:

Vorsitzender:	Prof. Dr. A. Muramatsu
Hauptberichter:	Prof. Dr. M. Mehring
Mitberichter:	Prof. Dr. H. Schweizer
Tag der Einreichung:	08. August 2005
Tag der mündlichen Prüfung:	07. September 2005

2. Physikalisches Institut der Universität Stuttgart
2005

Die Naturwissenschaften braucht der Mensch zum Erkennen, den Glauben zum Handeln. Religion und Naturwissenschaft schließen sich nicht aus, wie heutzutage manche glauben und fürchten, sondern sie ergänzen und bedingen einander. Für den gläubigen Menschen steht Gott am Anfang, für den Wissenschaftler am Ende aller Überlegungen.

Max Planck (1858-1947)

Die vorliegende Arbeit wurde am 2. Physikalischen Institut der Universität Stuttgart unter Anleitung von Prof. Dr. M. Mehring, am Max-Planck Institut für Festkörperforschung, Stuttgart unter Anleitung von Dr. habil. S. Roth und am Laboratoire des Colloïdes, Verres et Nanomatériaux LCVN, Montpellier unter Anleitung von Dr. C. Goze-Bac angefertigt.

Preface

Carbon has been studied and used for centuries and carbon science was long thought to be a mature field. Diamond (3D) and graphite (2D) are two natural crystalline forms of pure carbon. In 1985, Harold Kroto from the University of Sussex, James Heath, Sean O'Brien, Robert Curl and Richard Smalley from Rice University, discovered C_{60} and the **fullerenes** [1]. Fullerenes are allotropes of pure carbon where the carbon atoms form a closed, hollow cage. Kroto, Curl, and Smalley were awarded the 1996 Nobel Prize in chemistry for their roles in the discovery of this class of compounds.

One of the most exciting properties among the fullerene molecules family is the superconductivity of alkali intercalated solid materials A_3C_{60} (where A is an alkali metal) with transition temperatures among the highest known apart from the high-Tc cuprates [2, 4–7].

Since a short while, fullerenes are under extensive study for potential medical use binding specific antibiotics to the structure to target resistant bacteria (e.g. blocking the HIV virus), target certain cancer cells such as melanoma or as contrast agents for X-ray and magnetic resonance imaging [8–10].

Carbon nanotubes which consist of rolled graphene sheets built from sp^2 hybridized carbon atoms were first discovered in the early 1970s by Morinobu Endo [11]. Unfortunately this report did not cause a great impact because at this time scientists were more interested in micron-size carbon fibers. It started to have impact when Sumio Iijima in 1991 found carbon nanotubes accidentally during the arc-evaporation synthesis of fullerenes [12]. He observed that the sample contained helical carbon microtubules (now called nanotubes) and nanoparticles. From that point, carbon nanotubes attract scientists from various disciplines due to their fascinating electronic, mechanical and thermal properties.

Worth mentioning are for example their electronic properties: carbon nanotubes can behave like a metal or a semiconductor depending on their chirality and metallic nanotubes are nearly one dimensional ballistic conductors. These electronic properties may be further modified via chemical intercalation of alkali metals, which tunes the Fermi level and plays an important role in superconductivity of graphite and C_{60} . All in all, carbon nanotubes are believed to have very promising applications

in future as stated by Richard Smalley: *'These nanotubes are so beautiful that they must be useful for something'*.

Since the invention of lithium-ion batteries, carbon based materials such as natural graphite, carbon fibers, and pyrolytic carbon were investigated as possible candidates for the use as battery anode materials [13,14]. In 1990, Sony was the first company to commercialize lithium-ion batteries. At present multi-walled carbon nanotubes (MWNT) of 10 nm to 100 nm in diameter (*Endo fibers*) are in regular use to prolong the lifetime of these batteries. Recently, new progress have been reported for the use of single-walled carbon nanotubes (SWNT) as battery anode materials [15].

These examples show how alkali intercalation in SWNT is able to bring fascinating properties applicable in commercial high-end products.

In the present work, the structural and electronic properties of **alkali intercalated SWNT** are investigated using **nuclear magnetic resonance** (NMR). High resolution NMR techniques have proven to be a remarkably versatile tool for the elucidation of key properties of graphite, alkali-graphite intercalation compounds (GIC) and C₆₀ fullerenes, addressing static and dynamic structural properties as well as characteristics of electronic structures [4, 16, 17, 19].

In the first two chapters of this work, the fundamentals of carbon nanotubes and NMR are introduced. After a brief presentation of the spatial and electronic properties of SWNT, the most important structural properties of alkali intercalated graphite are discussed. In the NMR chapter emphasis is put on the origin of shift interactions in NMR as well as relaxation theory due to electron-nuclear couplings and molecular dynamics. Finally, basic ¹³C NMR shifts in SWNT are presented and discussed.

Chapter 3 deals with **Li intercalation in SWNT bundles**. After presenting the applied wet chemical Li intercalation technique, it is shown how ¹³C NMR can be used to determine the density of states at the Fermi level for various intercalated samples. Afterwards, ⁷Li NMR is used to determine the intercalation sites in the SWNT bundles. Li-C hybridization effects as well as free thermally activated Li diffusion are treated. In order to clarify the role of the cointercalated solvent THF, temperature dependent ¹H NMR measurements are presented and discussed.

Cs intercalated SWNT are in the centre of attention of chapter 4. First, a new preparation method for obtaining well defined Cs intercalation stoichiometries is shown, followed by ^{13}C NMR measurements in order to elucidate the electronic properties of the system.

Electron charge transfer limitations are discussed in context with hybridized and diffusing Cs^+ cations intercalated in the interstitial channels of SWNT bundles. In connection with ^{133}Cs NMR measurements, electron charge transfer limitations are discussed in context with hybridized as well as diffusing Cs^+ cations. The obtained results are compared with NMR investigations in alkali intercalated graphite.

Contents

Preface	i
Contents	v
List of Symbols and Abbreviations	ix
1 Properties of Carbon Nanotubes and Graphite	1
1.1 Spatial Properties of Carbon Nanotubes	2
1.1.1 Production and Purification of SWNT	4
1.1.2 SWNT Bundeling	5
1.1.3 SWNT Intercalation	6
1.2 Electronic Structure of Carbon Nanotubes	7
1.2.1 Bandstructure	7
1.2.2 Tomonaga-Luttinger Liquid Theory	8
1.3 Spatial Structure of Graphite – Intercalation	10
2 Fundamentals of NMR	13
2.1 Spin Interactions and Spectra	13
2.1.1 Magic Angle Spinning	14
2.1.2 Magic Angle Turning	14
2.1.3 Chemical Shift	17
2.1.4 Knight Shift	17
2.1.5 Quadrupolar Interactions	21
2.1.6 Spectra Under Molecular Motion	26
2.2 Relaxation Effects in NMR	28
2.2.1 Hyperfine Relaxation	28
2.2.2 Scalar Spin-Spin Coupling	30
2.2.3 Dynamic Relaxation - Weak Collision	31
2.2.4 Dynamic Relaxation - Strong Collision	33
2.2.5 Stimulated Echo	34
2.3 ¹³ C NMR Shifts in Carbon Nanotubes	36
2.3.1 Spectra and Sample Purity	36
2.3.2 Shift Interactions in SWNT	38

3	Lithium Intercalated SWNT	41
3.1	Sample Preparation and Experimental Conditions	41
3.2	^{13}C NMR	43
3.2.1	Spectra	43
3.2.2	$1/T_1$ Relaxation Rate	46
3.3	^7Li NMR	54
3.3.1	Spectra	54
3.3.2	$1/T_1$ Relaxation Rate	57
3.4	^1H NMR	60
3.4.1	Spectra	60
3.4.2	$1/T_1$ Relaxation Rate	62
3.4.3	Structural THF Arrangement	64
3.4.4	Negative Line Shifts	67
3.5	Comparison of ^1H and ^7Li NMR $1/T_1$ Relaxation Rates	68
3.6	Summary	70
4	Cesium Intercalated SWNT	73
4.1	Sample Preparation and Experimental Conditions	73
4.2	^{13}C NMR	74
4.2.1	Static Spectra	74
4.2.2	MAS	76
4.2.3	MAT	76
4.2.4	$1/T_1$ Relaxation Rate	80
4.2.5	Discussion of ^{13}C NMR Data	83
4.3	^{133}Cs NMR	85
4.3.1	Nutation Experiments	85
4.3.2	$\pi/2 - \beta$ Experiments	86
4.3.3	General Considerations of the Static Spectra	86
4.3.4	α -Line FWHM	88
4.3.5	α -Line, $1/T_2^\alpha$ Relaxation Rate	90
4.3.6	α -Line, $1/T_1^\alpha$ Relaxation Rate	92
4.3.7	β -Line, Spectral Analysis	94
4.3.8	β -Line, $1/T_1^\beta$ Relaxation Rate	96
4.3.9	β -Line, $1/T_2^\beta$ Relaxation Rate	98
4.3.10	β -Line, Stimulated Echo Relaxation	100
4.3.11	Temperature Dependence of α - and β -Line Shifts	103
4.3.12	Comparison with ^{133}Cs NMR of Cs-GIC	105

4.4 Summary and Discussion	107
Summary	111
Zusammenfassung	115
Bibliography	121
List of Figures	137
List of Tables	139
Lebenslauf	141
Danksagung	143

Symbols and Abbreviations

Symbols meant to represent vectors, matrices or tensors are typed in bold face.

α	type of alkali ion
α	pulse angle
A_{IS}	strength of spin-spin coupling
A_{dip}	dipolar hyperfine coupling constant
a_{iso}	isotropic hyperfine coupling constant
β	pulse angle
β	type of alkali ion
β_{opt}	optimum pulse rotation angle for quadrupolar echoes
C	quadrupolar echo amplitude factor
$\gamma(t)$	angular MAT rotor position
γ_e	electron gyromagnetic ratio
γ_n	nuclear spin gyromagnetic ratio
d_{ii}	(<i>ii</i>)-component of the dipolar hyperfine coupling tensor
$\delta\nu_{rf}$	excitation bandwidth
$\delta\nu_{probe}$	probe bandwidth
ΔE	activation energy
δ_{iso}	isotropic shift
δ	shift tensor
e	elementary charge
$n(\varepsilon_F)$	density of states at the Fermi level
η	asymmetry parameter
$f(\omega)$	lineshape function
F_1	frequency axis of isotropic chemical shift in MAT
F_2	frequency axis of static anisotropic powder pattern in MAT
G	FID intensity
g	Lande factor
$G(t)$	autocorrelation function
$\zeta_{1/2}$	evolution and acquisition spectral widths (MAT)
\mathcal{H}	Hamiltonian
\mathbf{H}_0	vector of the applied magnetic field
\hbar	Planck's constant
\mathbf{I}	nuclear-spin vector
I	spin quantum number
I	intensity
$\hat{I}_{X/Y/Z}$	operators of the nuclear spin I

J	spin-spin coupling constant
$J(\omega)$	spectral density
\mathbf{K}	Knight shift tensor
K_{ii}	elements of the anisotropic Knight shift tensor
K_{iso}	isotropic Knight shift
$K_a(t)$	memory function
k_B	Boltzmann factor
M	magnetization
m	slope of a line
M_n	n th moment of a lineshape function
μ_0	vacuum permeability constant
μ_B	Bohr magneton
$ m\rangle$	eigenstates of the Zeeman Hamiltonian
N_A	Avogadro's number
$\delta\nu$	FWHM
$p_{1/2}$	rf-pulse
Φ	precession angle
ψ	wave function
σ_{ii}	shift tensor elements
σ	chemical shift tensor
S_K	Korringa enhancement factor
τ	time delay
τ_{1e}	electron spin-lattice relaxation time
τ_0	correlation time at infinite temperature
τ_{c0}	correlation time at T=1 K
τ_c	correlation time
T	integral number of MAT rotor periods
T	temperature
T_1	spin-lattice relaxation time
T_2	spin-spin relaxation time
$T_{1\rho}$	spin-lattice relaxation time in the rotating frame
T_1^{stim}	decay time of the stimulated echo
t_a	time for data acquisition
ϑ_{magic}	magic angle
\mathbf{V}	electric field gradient tensor
χ_s	reduced Pauli spin-susceptibility
ω_{rf}	Rabi frequency
ω_{iso}	resonance angular frequency of the isotropic shift
ω_0	Larmor frequency
ω_Q	quadrupole frequency
ω_r	MAS spinning frequency

1D/2D/3D	one-/two-/three-dimensional
bcc	body-centered cubic
BPP	Bloembergen, Purcell and Pound (theory)
CSA	chemical shift anisotropy
CVD	chemical vapor deposition
DFT	density functional theory
DMF	dimethylformamide
DOS	density of states
EFG	electric field gradient
FID	free induction decay
FWHM	full width at half maximum
GIC	graphitic intercalation compounds
MAS	magic angle spinning
MAT	magic angle turning
MWNT	multi-walled carbon nanotube
NMR	nuclear magnetic resonance
PEO	poly(ethylene oxide)
ppm	parts per million (10^{-6})
SDS	dodecylsulfate
SEM	scanning electron microscope
SWNT	single-walled carbon nanotube
TEM	tunneling electron microscope
THF	tetrahydrofuran
TLL	Tomonaga-Luttinger liquid
TMS	tetra methyl silan
XRD	X-ray diffraction

Constants and Factors

g	$=2.002319304386$
h	$=6.626076 \cdot 10^{-34} \text{ Js} = 4.135667 \cdot 10^{-15} \text{ eVs}$
\hbar	$=h/2\pi = 1.054571596 \cdot 10^{-34} \text{ Js}$
k_B	$=1.380658 \cdot 10^{-23} \text{ JK}^{-1} = 8.617347 \cdot 10^{-5} \text{ eVK}^{-1}$
μ_B	$=\gamma_e \hbar/g = 9.274015 \cdot 10^{-24} \text{ Am}^2$
μ_n	$=5.050787 \cdot 10^{-27} \text{ Am}^2$
μ_0	$=1.25663706 \cdot 10^{-6} \text{ mkg s}^{-2} \text{ A}^{-2} = 4\pi 10^{-7} \text{ T}^2 \text{ m}^3/\text{J}$
N_A	$=6.0221415 \cdot 10^{22} \text{ mol}^{-1}$
e	$=1.60217653 \cdot 10^{-19} \text{ C}$

Chapter 1

Properties of Carbon Nanotubes and Graphite

In the following chapter, single-walled carbon nanotubes (SWNT) are introduced. The description is limited to aspects, that are of importance for understanding the experiments in the present work.

For more far-reaching information on preparation of carbon nanotubes as well as the various physical properties of SWNT refer to various monographs in literature [12, 49–52].

Possible fields of SWNT application and current progress are generally discussed in Ref. [52–58]. The nanometer dimensions of the carbon nanotubes together with the unique electronic structure of a two-dimensional graphene sheet make the electronic properties of these one-dimensional carbon nanotubes highly unusual (*quantum wires*). Specialized SWNT applications in nano- and microelectronics are treated in Ref. [59–66]. Furthermore, SWNT are expected to have very good mechanical properties because of the carbon-carbon chemical bond in the graphene layer. This bond is probably the strongest chemical bond ever known in nature. Applications using the outstanding mechanical properties of SWNT are discussed in Ref. [67–70].

After a brief introduction of the spatial SWNT structure, the resultant electronic bandstructure is described. Finally, the most important structural properties of alkali intercalated graphite are introduced.

1.1 Spatial Properties of Carbon Nanotubes

As illustrated in Fig. 1.1 SWNT can be viewed as single graphene sheets rolled into a cylinder with typical diameters in the range of 1-2 nm and length up to several hundred micrometers. These quasi one-dimensional cylindrical tubulus can either have open ends or closed caps at each end, such that the caps can be joined together to form a fullerene. There also exist so-called multi-walled carbon nanotubes (MWNT), which can be seen as several coaxially aligned SWNT.

It is convenient to specify carbon nanotubes in terms of the chiral vector $\mathbf{w} = n\mathbf{a}_1 + m\mathbf{a}_2$ (Fig. 1.2). \mathbf{a}_1 and \mathbf{a}_2 are unit basis vectors on the graphene honeycomb lattice and the integers (n, m) uniquely determine the tubule diameter d_t and the chiral angle Θ . A nanotube with a chiral angle $\Theta = 0^\circ$ is called a 'zigzag tube', whereas a nanotube with $\Theta = 30^\circ$ is called an 'armchair' tube. A nanotube with a general chiral angle with $0 < |\Theta| < 30^\circ$ is called a 'chiral' tube (see Fig. 1.3). The SWNT diameter is given by $d_t = a\sqrt{n^2 + m^2 + nm}/\pi = |\mathbf{w}|/\pi$ with a being the length of the graphene unit vector ($a = 2.46 \text{ \AA}$) [50].

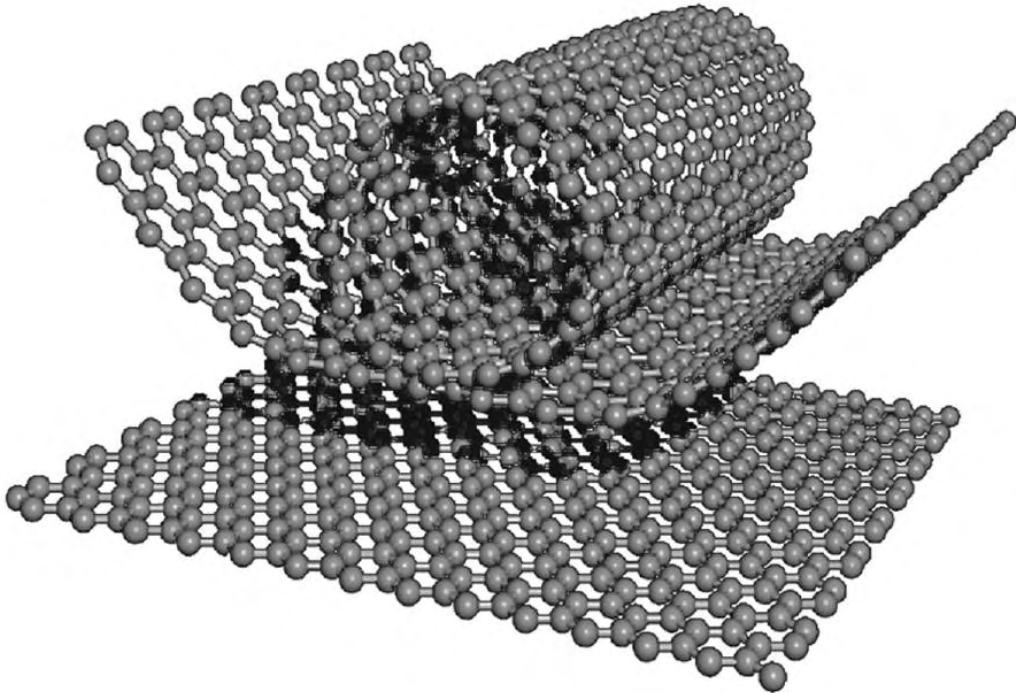


Figure 1.1: Schematic of a graphene layer, rolled up in order to form a carbon nanotube [58].

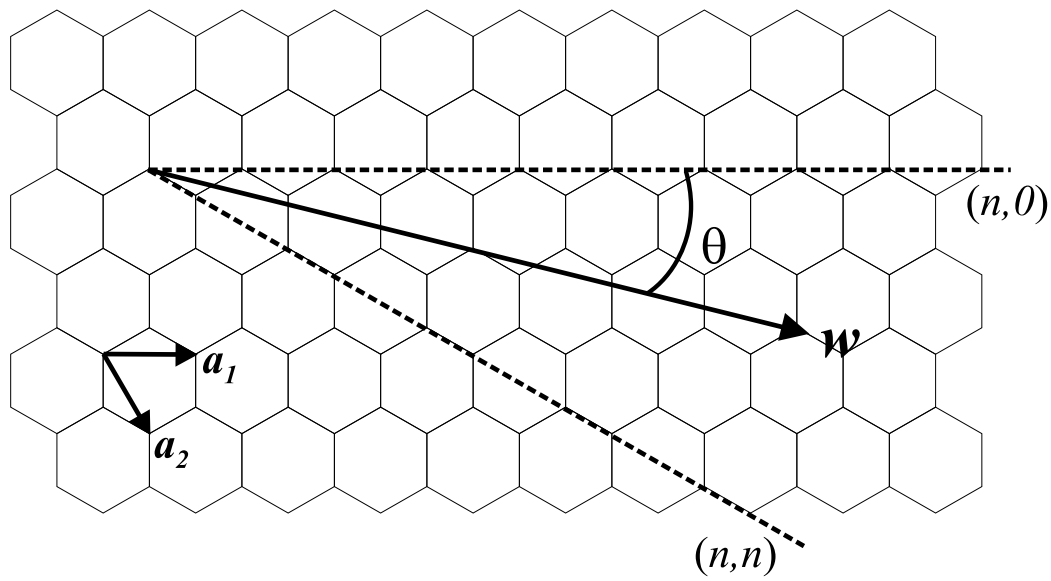


Figure 1.2: 2D graphene sheet. The chiral vector \mathbf{w} is defined with respect to the zigzag axis. \mathbf{a}_1 and \mathbf{a}_2 are unit basis vectors on the graphene honeycomb lattice [71].

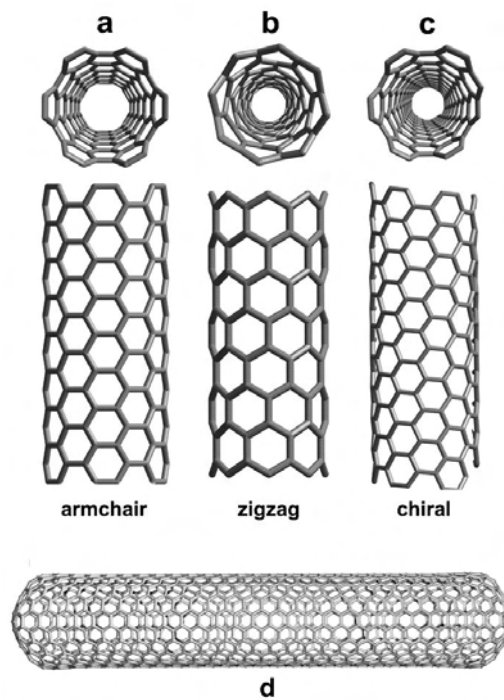


Figure 1.3: Molecular models of SWNTs exhibiting different chiralities: (a) armchair configuration, (b) zigzag arrangement, and (c) chiral conformation. (d) Molecular model of a SWNT that is capped by six pentagons in each nanotube end [57].

1.1.1 Production and Purification of SWNT

Carbon nanotubes are produced by different methods [50] like arc-burning of graphite rods [72], laser ablation of graphitic targets [73] and chemical vapor deposition (CVD) of hydrocarbons [64, 74].

In the arc discharge method, a vapor is created by an electric arc between two carbon electrodes and nanotubes self-assemble from the resulting carbon vapor.

In the laser ablation technique, a high-power laser beam impinges on a graphite laser vaporization target inside a furnace. Nanotubes are formed and flowing argon gas sweeps the nanotubes to a cooled collector.

In the CVD method, nanotube growth involves heating catalyst nanoparticles placed at well-defined surface sites in a reactor with flowing hydrocarbon gases. Carbon nanotubes grow from the particles via catalytic dissociation of the hydrocarbon molecules. With CVD, true scalability is possible what favors commercial production. This method also makes it possible to control the growth of the tubes and to construct nanometer sized devices [63, 64, 74].

The SWNT in the present work are made by arc-burning of a carbon rod consisting of graphite and either Ni/Y metal catalysts or non magnetic Pt/Rh catalysts.

Generally, the catalysts are needed to preferably favor the formation of SWNT than the formation of fullerenes or other kinds of carbon allotropes. However, the production yield of pristine SWNT is claimed to be less than 40-50%. Metal catalyst nanoparticles and carbon impurities mask the intrinsic properties of the SWNT and purification or special sample part selection of the as-grown material is needed. Pt/Rh catalysts have the advantage of being non-ferromagnetic materials which favors their use in NMR experiments [34, 75].

Common to all SWNT production techniques is a wide diameter and length distribution of as produced SWNT, which can be poorly controlled. Separation of nanotubes according to diameter and chirality is not considered under the topic of purification [76]. Nevertheless, length and diameter separation of nanotubes is required for many applications [53, 54], which is still an unsolved problem and considerable challenge.

Various methods for the purification of pristine SWNT exist in literature [77–81]. Removal of amorphous carbon by oxidation in air, as well as chemical oxidation and

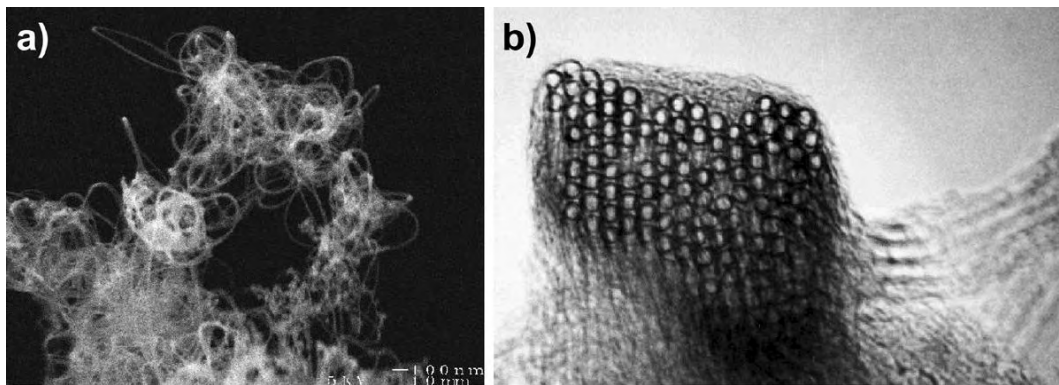


Figure 1.4: (a) SEM image of a SWNT bundles produced using the laser ablation technique; (b) TEM image of the cross section of a SWNT bundle showing various tubes of the same diameter (e.g., 1.38 Å) [57].

subsequent removal of metal catalysts are claimed to be very efficient purification techniques. However, they also induce defects in the SWNT by removing end caps or chemically functionalization of the reactive surface of the tubular carbon cylinders [82].

1.1.2 SWNT Bundeling

As shown in Fig. 1.4, due to van der Waals interactions between individual tubes, SWNT favor to bundle to ropes of ten up to hundreds of nanotubes, forming a regular triangular lattice. For typical samples of pristine SWNT with a mean nanotube diameter of 1.2 Å, the lattice constant is about $a = 17$ Å, which corresponds to the natural interlayer spacing found in natural graphite.

Separation of the bundled SWNT into individual nanotubes is only achievable by sonication dispersing of SWNT bundles in solutions of aqueous micellar suspensions [83]. The reason for using micellar suspensions is to apply a coating on the individual SWNT surfaces to prevent reaggregation. Typical solutions are dimethyl formamide (DMF) or sodium dodecyl sulfate (SDS).

However, the individual SWNT only exist stable in micellar suspensions or after highly diluted adsorption on a silicon surface. Filtering the solution through a Teflon filter membrane will always result in a reaggregation of the individual tubes to bundles. Therefore it is impossible to perform any experiments on bulk samples of individual SWNT.

One possibility to avoid any bundling of SWNT is the usage of freestanding individual nanotubes on a substrate [64]. However, this always requires the substrate to be included in the experimental investigations.

1.1.3 SWNT Intercalation

Similarly to graphite [16, 17, 31, 84–98] and C_{60} [3, 4, 19, 99–103], it was shown that SWNT bundles can be intercalated with various electron donors or acceptors through physisorption or chemisorption [104–138, 140, 141]. Preferable binding sites of intercalants are located at the external surface of a SWNT bundle and the interstitial channels of the triangular bundle lattice. If the ends of the nanotubes are open, the interior of the tubes provides additional intercalation sites [110, 111, 142–144].

Theoretical calculations on alkali metal intercalations can be found in Ref. [70, 142, 143, 145–160].

Three common techniques are known to intercalate alkali metals in SWNT, wet chemical intercalation, electrochemical intercalation and vapor phase intercalation.

- **Wet chemical intercalation** is mainly used to intercalate Li in SWNT by using solutions of aromatic hydrocarbons and SWNT [125, 161]. The advantage of this method is the controllability of the intercalated sample stoichiometry by tuning the redox potential and therefore choosing appropriate kinds of aromatic hydrocarbons. The disadvantage is a cointercalation of solvent molecules.
- **Electrochemical intercalation** is typically performed with Li as intercalant. The reason is the application of Li in new secondary Li-ion batteries [13, 15, 123, 129, 137, 138, 140, 162–173]. Electrochemical intercalation allows to simultaneously study a variety of electrochemical testing techniques as well as performing conventional spectroscopy techniques like NMR.
- **Vapor phase intercalation** is performed following the two-bulb method by applying a temperature gradient between the alkali metal and the host sample [174]. Many alkali metals like K, Rb and Cs are usually intercalated using this simple sample preparation technique [96, 104, 110, 111, 116, 122, 124, 175]. In materials like C_{60} it was shown, that controlling the amounts of used alkali metal and host carbon material enables to prepare intercalated materials in well defined stoichiometries.

In case of carbon nanotubes such a kind of stoichiometry control should be rather difficult, since SWNT always contain impurities like metal catalysts, graphite and amorphous carbons in unknown amounts.

Most of intercalation works have been devoted to alkali metals. After reaction with heavy alkali metals like Rb or Cs, the saturation composition of the intercalated SWNT was reported to be MC_8 ($M=Rb, Cs$) [104, 122, 176–179].

1.2 Electronic Structure of Carbon Nanotubes

1.2.1 Bandstructure

Due to the basic interconnection between graphene and single-walled carbon nanotubes, the electronic structure of a SWNT can be obtained from the energy dispersion relations of two-dimensional graphite [50, 180–185]. By using periodic boundary conditions in the direction of the chiral vector \boldsymbol{w} , the wave vector associated with this direction becomes quantized, whereas the vector along the nanotube axis remains continuous for an infinite long nanotube. Therefore, the one dimensional energy bands of carbon nanotubes correspond to cross sections of the energy dispersion relation in graphene.

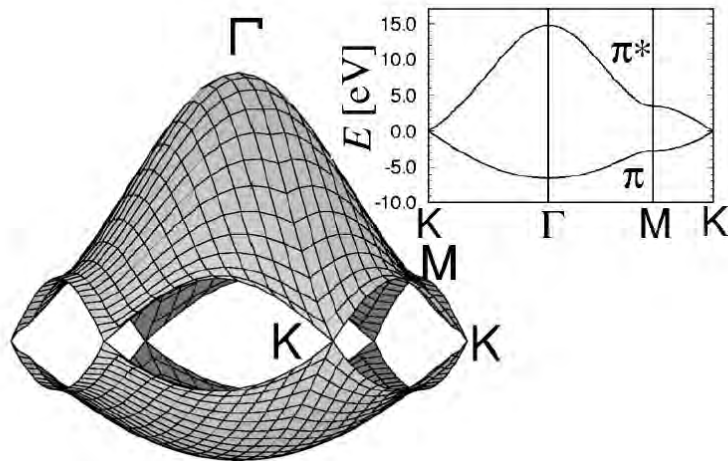


Figure 1.5: Energy dispersion relations for the π and π^* bands in 2D graphite. Inset: Energy dispersion along the high symmetry directions of the 2D Brillouin zone [180].

As illustrated in Fig. 1.5, the dispersion relation of graphene shows K points, where the π and π^* energy bands are degenerate. If for a particular (n, m) nanotube, the cutting line passes through a K point, the one dimensional energy bands have a zero energy gap and the density of states at the Fermi level has a finite value. This corresponds to a metallic carbon nanotube.

If, however, the cutting line does not pass through a K point, the carbon nanotube is expected to have a finite energy gap between valence and conduction band, which corresponds to a semiconducting carbon nanotube.

The density of states (DOS) of semiconducting (10,0) and metallic (9,0) SWNT calculated by tight binding approximation is shown in Fig. 1.6. The DOS does not consist of one smooth band, but shows a number of side-bands with spikes. These spikes are called *van Hove singularities*.

The side-bands are the characteristic signatures of the one-dimensional nature of conduction within the nanotube 1D system. The singularities arise from a linear crossing of π and π^* bands near the Fermi level with $dE/dk = 0$. The spacing of the van Hove singularities is determined by diameter and chirality of the SWNT. For larger-diameter tubes, the singularities move close together and merge, thereby making the DOS resemble that of a graphene layer.

All armchair (n, n) nanotubes are real metals with zero energy gap. (n, m) nanotubes with $(n - m) = 3j$, where j is a nonzero integer, show metallic character with a tiny band gap of several meV. The small band gap is due to the curvature of the SWNT. Considering finite temperatures, such a small energy gap can be neglected. All SWNT with $n - m = 3j \pm 1$ are large gap (~ 1 eV for $d_t \sim 0.7$ nm) semiconductors.

Therefore, about one third of all carbon nanotubes are metallic. All other (n, m) combinations correspond to semiconducting carbon nanotubes with energy gaps in the range of several hundred meV.

1.2.2 Tomonaga-Luttinger Liquid Theory

The electronic properties of conventional three-dimensional metals are successfully described by the Fermi-liquid theory. This theory deals with properties of many-fermion systems at low temperatures in the so-called normal state, which means that the system is not subject to a symmetry breaking phase transition.

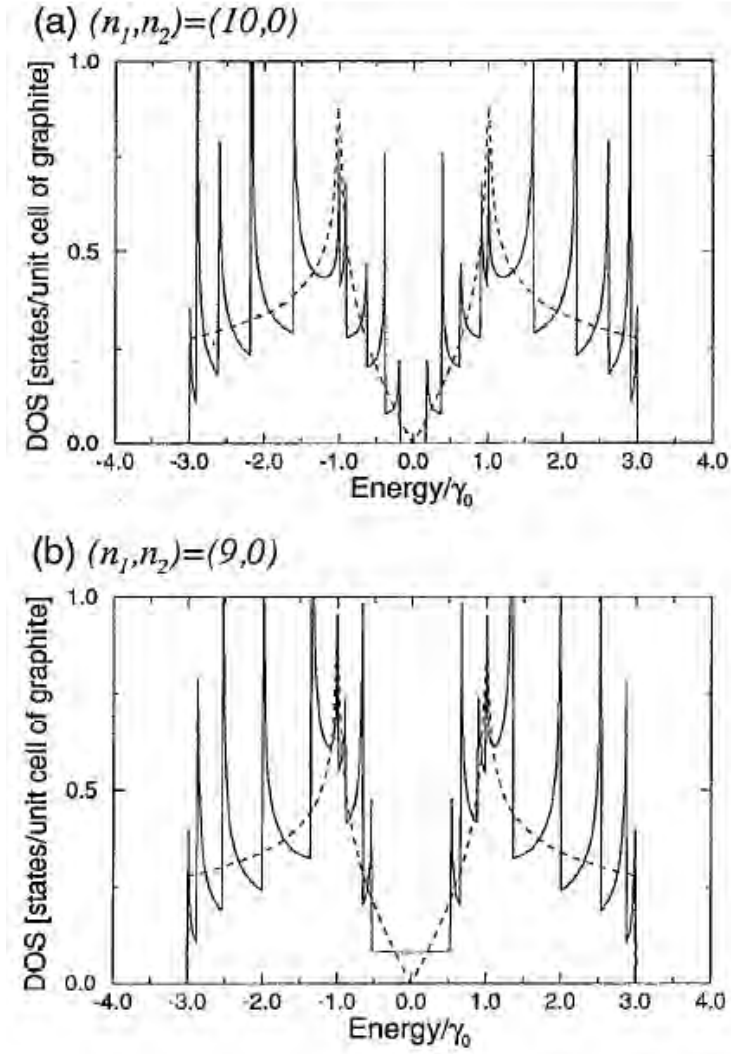


Figure 1.6: Calculated electronic density of states of (a) semiconducting (10,0) and (b) metallic (9,0) SWNT [182]. The dashed line indicates the density of states of graphene. The spike-like peaks are 'van Hove singularities' that are characteristic of one-dimensional materials.

In case the dimensionality of such a system is reduced to one, electron-electron interactions start to play a dominant role leading to a behavior significantly different from that of conventional Fermi liquids. The electrons exist in a state called a *Tomonaga-Luttinger liquid* (TLL), a one-dimensional correlated electron state characterized by a Luttinger parameter g that measures the strength of the interaction between electrons [186,187]. Strong repulsive interactions are characterized by $g \ll 1$, whereas $g = 1$ for the non-interacting electron gas [188].

Metallic SWNT are considered to be ideal one-dimensional systems for realizing TLL states [186, 187, 189–192]. The long-range Coulomb interaction between electrons is expected to yield a TLL state in SWNT with $g \sim 0.28$ [192]. A crucial point of the TLL theory is, that the electron density of states (DOS) near the Fermi level $n(\varepsilon_F)$ shows a power law dependence $n(\varepsilon_F) \propto \varepsilon^{(\alpha)}$, where α depends on the size of Coulomb interaction and can be expressed as $\alpha = (g - g^{-1} - 2)/8$.

1.3 Spatial Structure of Graphite – Intercalation

Carbon atoms in graphite are arranged in planes (*graphene sheets*), where each plane consists of a two-dimensional network of hexagons with a carbon-carbon distance of 1.42 Å. The carbon-carbon bonding can be described by a planar sp^2 hybridization with the remaining perpendicular p_z orbitals providing delocalized electrons around the network of *benzene rings*.

Graphitic intercalation compounds (GIC) are formed by the insertion of atomic or molecular layers of different chemical species, called the intercalant, between the graphitic planes of the graphite host material. A remarkable feature of GIC is the occurrence of the staging phenomenon. Staging means, that the intercalant species are arranged in well-defined layers between the graphitic planes.

Upon intercalation, the distance d_s between graphite layers sandwiching an intercalate layer, is increased. The interplanar spacing can vary from $d_s = 3.35$ Å in pure graphite up to 12.4 Å for big stage I intercalants like Li-THF complexes. In stage I Li-GIC without cointercalation of THF (tetrahydrofuran), $d_s \sim 3.7$ Å and in stage I Cs-GIC, $d_s \sim 5.9$ Å [16, 92].

The schematics of Cs intercalation in graphite is shown in Fig. 1.7. The stoichiometry CsC_8 corresponds to stage I, since the Cs atoms are located between every pair of graphite layers. CsC_{24} has a Cs layer after every second graphite plane (stage II). For Cs, this pattern is possible to extend in a well defined way up to stage VI.

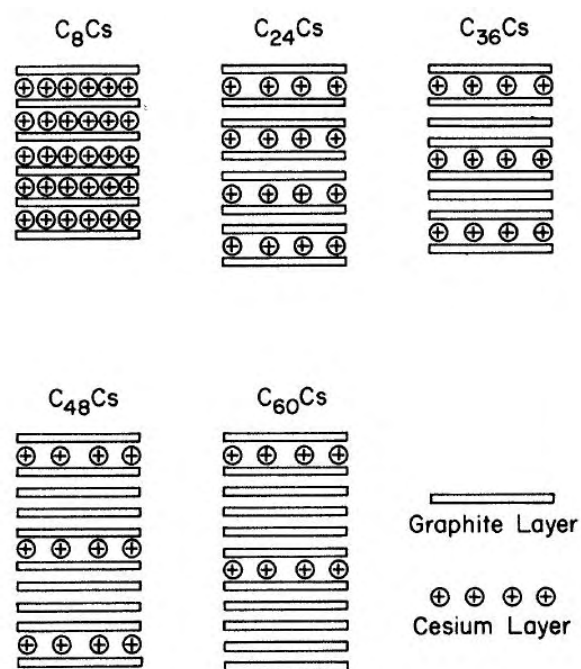


Figure 1.7: Schematic staging arrangement of Cs ions intercalated in graphite. For CsC_8 , stage I configuration is obtained. CsC_{24} corresponds to stage II, CsC_{36} to stage III. This pattern is extended up to stage V (CsC_{60}) [96].

Chapter 2

Fundamentals of NMR

Nuclear magnetic resonance (NMR) has proven to be a suitable tool for the elucidation of structural properties as well as characteristics of electronic structures in many carbonaceous materials [4, 16, 17, 19]. Various monographs introduce NMR as a spectroscopic tool [20–24]. Therefore, in this chapter only some fundamental parameters of NMR are mentioned and properties which are important for this work are discussed in more detail. First, the mechanisms leading to NMR frequency shifts are presented, considering chemical shift, Knight shift and quadrupolar splittings. Subsequently, relaxation processes due to electron-nuclear couplings as well as dynamically induced relaxation effects are discussed. Finally, typical NMR responses of SWNT like ^{13}C spectra and relaxation effects are presented.

2.1 Spin Interactions and Spectra

In general, the effective nuclear-spin Zeeman Hamiltonian \mathcal{H} is given by [23]

$$\mathcal{H} = -\gamma_n \hbar \mathbf{H}_0 \cdot (\mathbf{1} + \mathbf{K} - \boldsymbol{\sigma}) \cdot \mathbf{I} + \mathcal{H}_Q, \quad (2.1)$$

where \mathbf{H}_0 is the vector of the applied magnetic field, γ_n is the nuclear gyromagnetic ratio, \mathbf{I} is the nuclear-spin vector, and \mathcal{H}_Q is the Hamiltonian describing the interaction of the nuclear electric quadrupole moment with the local electric-field gradient. $\boldsymbol{\sigma}$ and \mathbf{K} are called the chemical- and Knight-shift tensors.

By measuring the shift $\boldsymbol{\delta}$ of the Larmor frequency of a nuclear spin, NMR provides information about the chemical environment and the electronic, metal-like properties of a compound. The NMR shift $\boldsymbol{\delta}$, which represents the perturbation of the applied magnetic field due to electrons, consists of a sum of two tensorial contributions, the chemical-shift $\boldsymbol{\sigma}$ and the Knight-shift \mathbf{K} with

$$\boldsymbol{\delta} = \boldsymbol{\sigma} + \mathbf{K}. \quad (2.2)$$

Both represent the fractional shifts of positions of the magnetic resonance frequencies, relative to the frequency in a reference compound containing the same nucleus.

As the shift tensors are in general anisotropic, their appropriate line positions depend on their principal axis orientation to the magnetic field. For powdery samples this results in a distribution of many lines and therefore broad powder spectra.

2.1.1 Magic Angle Spinning

In solids, line broadening due to second rank tensor interactions like the chemical shift anisotropy (CSA), dipole-dipole couplings or first order quadrupolar splittings usually govern the anisotropic shape of a NMR spectrum. By rotating a sample about an axis which is tilted by an angle ϑ with respect to the external magnetic field B_0 , the second rank shift tensor becomes time dependent and the average frequency $\omega(t)$ of the respective spectral line is given by [23]

$$\langle \omega \rangle = \omega_0 \left[\sigma_{iso} + \frac{1}{2} (3 \cos^2 \vartheta - 1) (\sigma_{zz} - \sigma_{iso}) \right]. \quad (2.3)$$

Under the magic angle condition $(3 \cos^2 \vartheta_{\text{magic}} - 1) = 0$, $\vartheta_{\text{magic}} = 54^\circ 44'$, all second rank shift tensor interactions are averaged out which leaves only δ_{iso} . Spinning a sample with a rotation frequency ω_r at the magic angle is called *magic angle spinning*, (MAS).

This process of sample spinning additionally causes sidebands with multiples of the rotation frequency ω_r relative to the isotropic line position in the spectrum. Thereby, the intensities are determined by the anisotropy [22,24]. By analyzing the distribution of the sidebands, Herzfeld and Berger [25] have shown that shift tensor elements σ_{11} , σ_{22} and σ_{33} can be determined from powder sample MAS spectra.

2.1.2 Magic Angle Turning

MAS has several limitations. One limitation is of technological character: Increasing static magnetic fields B_0 have the advantage of increasing the scaling of CSA which simplifies the separation of narrow spaced NMR lines. However, obtaining freestanding isotropic lines with MAS under these conditions requires higher and higher spinning rates. Since in this thesis, special glass sample tubes had to be used, the upper limit for the MAS-frequency was 5 kHz.

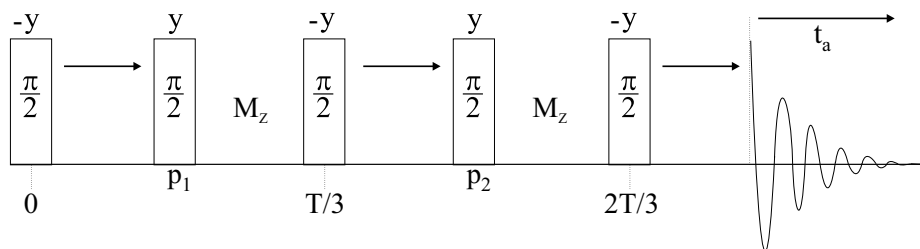


Figure 2.1: Pulse sequence for one of the four steps in the MAT-experiment. The time T is an integral number of rotor periods, excluding a multiple of three. The magnetization process along the longitudinal axis z is labeled M_z .

Another limitation considers NMR of samples, where spectral overlap of several broad isotropic lines prevents the use of MAS. Even though, the separation of these isotropic lines might be possible using MAS at large magnetic fields and high spinning rates, any potentially useful information embodied in the CSA pattern, i.e. the anisotropic shift tensor elements σ_{11} , σ_{22} and σ_{33} , will not be accessible.

All these problems can be overcome using *Magic Angle Turning* (MAT), a two-dimensional Fourier transform technique which presents the isotropic chemical shift projection in one frequency dimension (F_1) and the static anisotropic powder pattern along the other frequency axis (F_2) [26]. In the following, the discussion will be related to chemical-shift anisotropy (CSA), but it can be extended to any other kind of second-rank tensorial interaction.

The MAT experiment is carried out by mounting a sample at the magic angle ϑ_{magic} relative to the static external magnetic field B_0 and turning it with a constant rotor frequency accounting up to several tenth of Hz (typically 30-150 Hz). The MAT NMR pulse sequence is shown in Fig. 2.1.

In general, the experiment starts with a $\pi/2$ pulse which stores the z -magnetization M_z in the $x-y$ plane, where precession through an angle Φ_1 around the z -axis occurs. After a time $\tau/3$, this transverse magnetization is stored back along z by a $\pi/2$ pulse. The phase of the latter projection pulse selects either $\cos(\Phi)$ or $\sin(\Phi)$ transverse components.

In case of Fig. 2.1, starting with a $\pi/2_{-y}$ pulse and using a second $\pi/2_y$ pulse 'p1', $M_0 \cos(\Phi_1)$ is stored back along the longitudinal axis z . At a time $T/3$, where T

is an integral number of rotor periods (excluding a multiple of three), a $\pi/2$ pulse reestablishes transverse magnetization which precesses for another time $\tau/3$ by an angle Φ_2 , before being projected back into z -direction by a $\pi/2$ pulse 'p₂'. Again, the phase of this pulse selects either $\cos(\Phi)$ or $\sin(\Phi)$ transverse components.

In case of Fig. 2.1, the magnetization after this $\pi/2_y$ pulse is given by $M_0 \cos(\Phi_1) \cos(\Phi_2)$. At the time $2T/3$, this process is repeated a third time starting with a $\pi/2$ pulse projecting z -magnetization in the $x - y$ plane, where precession with an angle Φ_3 occurs for a time $\tau/3$. After this last period of time, data acquisition in the t_a domain is started under the consecutive evolution of the transverse magnetization.

In the case of the illustrated MAT-sequence in Fig. 2.1, the FID of the final transversal magnetization after $t_a = 0$ can be written as

$$M(t) = M_0 \cos(\Phi_1) \cos(\Phi_2) \cos(\Phi_3) F_a(t_a) \quad (2.4)$$

with $F_a(t_a)$ describing the evolution of the transverse magnetization during data acquisition. $F_a(t_a)$ additionally considers longitudinal and transversal relaxation effects which occur during the complete pulse sequence.

The precession angles Φ_i can be written as time integrals of the resonance angular frequency $\omega(\gamma(t))$ which itself is a function of the rotor position $\gamma(t)$. Since the magnetization precession with Φ_i starts at well defined rotor positions given by the angles $\gamma(t)$, $\gamma(t + T/3)$ and $\gamma(t + 2T/3)$ (e.g. rotor positions equally spaced at 120° around the circle of rotation), it can be shown that [27]

$$\Phi_1 + \Phi_2 + \Phi_3 = \omega_{iso} \tau. \quad (2.5)$$

ω_{iso} is the resonance angular frequency of the isotropic shift. Finally, in MAT a repetitive four-step phase cycling and therewith a combination of FID signals has to be performed. This is done by choosing an appropriate variation of the phases of the projection pulses p₁ and p₂ as well as additionally varying the detector phase [27, 28]. In this case, Fourier transform of the phase cycled FID as a function of t_a yields a frequency domain (F_2) from which the anisotropic powder pattern can be extracted. Fourier transform as a function of τ will result in a frequency domain (F_1) containing a sideband-free isotropic-shift spectrum. Thus, usage of the MAT 2D spectroscopy technique enables measuring of isotropic shifts and anisotropic powder patterns simultaneously.

In order to obtain simplified phase tables in the four-step phase cycling, a slightly modified MAT-pulse sequence can be used by starting the data acquisition directly after the last pulse. However, omission of the phase angle Φ_3 results in a sheared 2D-spectrum with inclined bands relative to the acquisition axis at an angle $\arctan(\zeta_2/3\zeta_1)$ ($\zeta_{1/2}$ are the evolution and acquisition spectral widths, respectively) [27].

2.1.3 Chemical Shift

The chemical shift tensor $\boldsymbol{\sigma}$ consist of two components, the London ring-current contribution and the Pople correction. The first contribution is an effect due to delocalized electronic interatomic currents well known in aromatic materials, whereas the second term describes a local contribution due to hybridization effects.

The axial symmetric, diagonalized shift tensor $\boldsymbol{\sigma}$ can be separated into two parts, the isotropic part which is equal to the average of the three principal components of the tensor, and the remaining traceless anisotropic part:

$$\boldsymbol{\sigma} = \begin{pmatrix} \sigma_{xx} & 0 & 0 \\ 0 & \sigma_{yy} & 0 \\ 0 & 0 & \sigma_{zz} \end{pmatrix} \equiv \sigma_{iso} \cdot \mathbf{1} + \begin{pmatrix} \sigma_{11} & 0 & 0 \\ 0 & \sigma_{22} & 0 \\ 0 & 0 & \sigma_{33} \end{pmatrix} \quad (2.6)$$

σ_{iso} is the isotropic chemical shift given by

$$\sigma_{iso} = \frac{1}{3} (\sigma_{xx} + \sigma_{yy} + \sigma_{zz}). \quad (2.7)$$

and the elements of the anisotropic chemical shift tensor are given by $\sigma_{11} = \sigma_{xx} - \sigma_{iso}$, $\sigma_{22} = \sigma_{yy} - \sigma_{iso}$ and $\sigma_{33} = \sigma_{zz} - \sigma_{iso}$.

2.1.4 Knight Shift

The Knight shift is only observable in metallic compounds and arises from electron-nuclear spin-spin hyperfine interactions. Comparable to the chemical shift, the axial symmetric, diagonalized shift tensor \mathbf{K} can be separated into the isotropic Knight shift K_{iso} given by

$$K_{iso} = \frac{1}{3} (K_{xx} + K_{yy} + K_{zz}) \quad (2.8)$$

and the traceless anisotropic part with $K_{11} = K_{xx} - K_{iso}$, $K_{22} = K_{yy} - K_{iso}$ and $K_{33} = K_{zz} - K_{iso}$.

Isotropic Knight Shift

The following survey is related to ^{13}C nuclei but can be extracted to any other type of nuclei. The isotropic Knight shift is composed of several contributions:

- (i) *Direct Fermi contact coupling* of the nuclear spin with the s spin density at the site of the nucleus.
- (ii) *Core polarization*: coupling of the nuclear spin to the on-site $2p_z$ electron spins. This coupling polarizes the (filled) on-site $1s$ core electrons which produces a net unpaired spin density at the nucleus.
- (iii) *Spin polarization of σ -bonds*: the on-site $2p_z$ electron polarizes the on-site sp^2 orbitals that make up σ -bonds with neighboring nuclei. This causes a net polarized spin-density at the nucleus, which interacts with the nucleus through the Fermi contact mechanism.
- (iv) *Transferred hyperfine coupling*: $2p_z$ electron-spin densities in neighboring nuclei polarize sp^2 orbitals that make up σ -bonds. This causes a transferred oppositely net polarized spin-density of the according on-site (σ -bond) sp^2 orbitals, which interacts with the nucleus through the Fermi contact mechanism (Fig. 2.2).

Direct Fermi contact coupling (i) and spin polarization of σ -bonds (iii) give rise to positive Knight shifts, whereas core polarization (ii) and the transferred hyperfine coupling (iv) cause negative Knight shifts [3, 4].

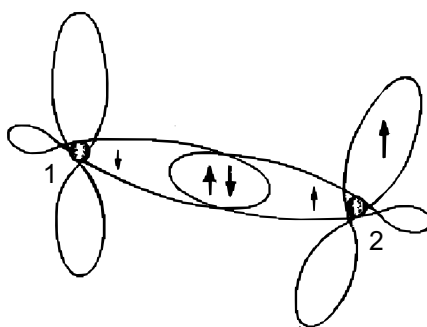


Figure 2.2: Schematics of transferred hyperfine coupling for two ^{13}C nuclei. The two carbon atoms (1) and (2) are connected by a σ bond. The unpaired up-electron spin in the $2p_z$ orbital of atom 2 generates an up-polarization of the spin density in the sp^2 orbital of atom (2). This causes a transferred net down-spin density on atom (1) and therewith a negative hyperfine coupling with the ^{13}C nucleus (1) [4].

In general, electron-nuclear Fermi contact hyperfine interactions can be described by the isotropic Knight shift

$$K_{iso} = \frac{8\pi}{3} \langle |\psi(0)|^2 \rangle \chi_s. \quad (2.9)$$

$\langle |\psi(0)|^2 \rangle$ is the average probability density at the nucleus for all electronic states on the Fermi surface [22]. The reduced Pauli spin-susceptibility χ_s can be described by [29]

$$\chi_s = \frac{1}{2} g^2 \mu_B^2 n(\varepsilon_F), \quad (2.10)$$

with $\mu_B = \gamma_e \hbar / g$ being the Bohr magneton, $g \sim 2$ the Lande factor and $n(\varepsilon_F)$ the density of states at the Fermi level.¹

Another possibility to express the Knight shift is to introduce a hyperfine coupling constant which modifies the Knight shift to [30]

$$K_{iso} = \frac{a_{iso}}{\gamma_n \gamma_e \hbar} \chi_s, \quad K_{ii} = \frac{d_{ii}}{\gamma_n \gamma_e \hbar} \chi_s \quad (i = 1, 2, 3, x, y, z). \quad (2.11)$$

a_{iso} is the isotropic hyperfine coupling constant and d_{ii} represents the (ii) -component of the dipolar hyperfine coupling tensor. γ_e and γ_n are the gyromagnetic ratios of the electron and the observed nuclear spin, respectively.

Isotropic Knight Shifts in Curved Carbon Materials

Generally, p -electrons will not contribute to isotropic Knight shifts, since their probability density at the nucleus vanishes. Thus in carbon materials for the case of perfect sp^2 hybridization K_{iso} should be zero, since sp^2 orbitals and the residual p_z orbitals have a zero probability density at the carbon nuclei.

However, sp^2 hybridization appears to yield a slightly paramagnetic Knight shift in C_{60} . The simple explanation is, that pure sp^2 hybridization exists only in the absence of curvature, which is not the case for carbons on a buckyball sphere, neither on a carbon nanotube tubulus. On curved carbon surfaces, the sp^2 orbitals which ordinarily lie within the xy plane (defined by the p_z orbital) must tilt somewhat to match neighboring carbons. This is achieved by a small admixture of the $2s$ wave function into the $2p_z$ orbital ($2p_z$ in order to retain its orthogonality), reaching a rehybridized state which lies in between the planar sp^2 and the tetrahedral sp^3 character. This

¹In order to practically use susceptibilities often represented in CGS-units [emu/mol], a conversion to SI-units [J/T²] has to be performed by using the relation $\chi_s = \chi_{SI} = \frac{N_A}{10} \chi_{CGS}$.

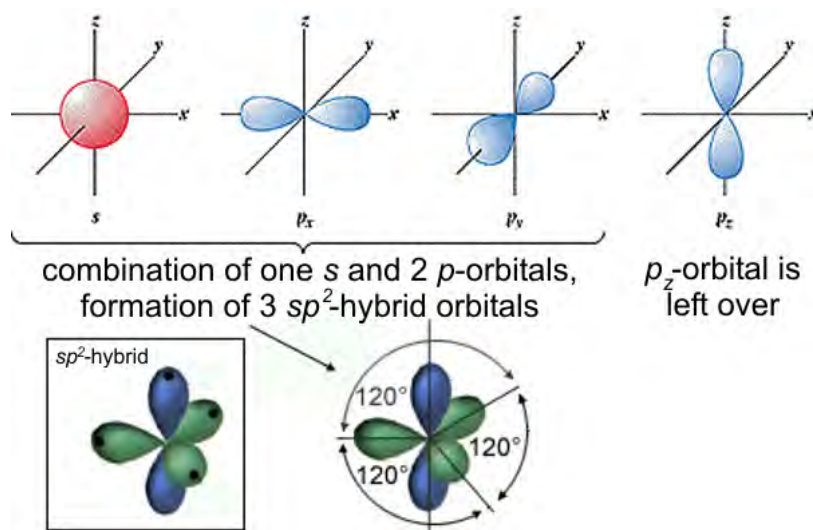


Figure 2.3: Schematics for sp^2 -hybridization. One s , p_x and p_y orbital form three sp^2 -hybrid orbitals lying in the $x-y$ plane. The leftover p_z orbitals are perpendicular to the sp^2 orbitals.

process can also be described as a small $\sigma - \pi$ hybridization if the overlap of orbitals with neighboring carbon atoms is considered.

By the rehybridization process, a small $2s$ -character of the carbon is retained, resulting in a non zero direct Fermi contact interaction and therefore in a small isotropic Knight shift. Even in alkali-GIC, the existence of such an isotropic Knight shift was proven [31]. In alkali intercalated C_{60} , K_{iso} is known to depend on the intercalation level as well as the type of intercalated alkali nuclei and can vary up to a few tenth of ppm relative to pure C_{60} [32].

Anisotropic Knight Shift

Due to the discussed predominant p_z and sp^2 orbital character of the electrons in graphene, C_{60} and carbon nanotubes, the main electron-nuclear interaction arises from couplings of non- s electrons to the nuclei through dipole-dipole interactions, which causes the anisotropic Knight shift K_{aniso} . Assuming an anisotropic dipolar hyperfine coupling tensor which is traceless with $d_{11} = -d_{33}/2$, the dipolar hyperfine coupling for interaction with the electrons in the p_z -orbital is given by [4, 33]

$$d_{11} \equiv A_{dip} = \frac{2}{5} \frac{\mu_0}{4\pi} \gamma_n \gamma_e \hbar \left\langle \frac{1}{r^3} \right\rangle. \quad (2.12)$$

μ_0 is the vacuum permeability constant and $\langle 1/r^3 \rangle$ describes the distance between the electronic spins in the p_z orbital and the interacting nuclear spin, averaged over the

conduction electron wave function.

The Knight shift anisotropy K_{aniso} is defined by

$$K_{aniso} = K_{zz} - \frac{1}{2}(K_{xx} + K_{yy}) \stackrel{K_{11}=K_{22}}{=} K_{33} - K_{11}. \quad (2.13)$$

Since in later discussions, a comparison of ^{13}C NMR anisotropic Knight shifts with corresponding Knight shifts in alkali-GIC is needed, the experimental behavior of K_{aniso} upon alkali metal intercalation in graphite will be briefly mentioned here:

In alkali-GIC, the ^{13}C NMR isotropic Knight shift upon intercalation is relatively small compared to variations in K_{aniso} . For higher stages of intercalation (≥ 2), the anisotropy upon charge transfer to a carbon atom is reduced to about [34]

$$K_{aniso} = K_{33} - K_{11,22} \sim -1800\text{ppm/electron}. \quad (2.14)$$

2.1.5 Quadrupolar Interactions

Nuclei with spin quantum number $I > 1/2$ possess an electrical quadrupole moment Q which may interact with an electric field gradient (EFG) present at the site of the nucleus. $\{V_{ik}\}$ are the tensor elements of the electric field gradient tensor \mathbf{V} with

$$V_{ik} = \frac{\partial^2 V}{\partial i \partial k}. \quad (2.15)$$

In the principal axis frame (X, Y, Z) of the traceless electric field gradient tensor, the quadrupole Hamiltonian can be written as

$$\mathcal{H}_Q = \frac{\hbar\omega_Q}{2} \left[\hat{I}_Z^2 - \frac{1}{3}I(I+1) + \frac{1}{3}\eta(\hat{I}_X^2 + \hat{I}_Y^2) \right] \quad (2.16)$$

with the quadrupole frequency

$$\omega_Q = \frac{3eQ}{2I(2I-1)\hbar} V_{ZZ} \quad (2.17)$$

and the asymmetry parameter

$$\eta = \frac{V_{XX} - V_{YY}}{V_{ZZ}} \quad (|V_{ZZ}| \geq |V_{XX}| \geq |V_{YY}|) \quad (2.18)$$

with $0 \leq \eta \leq 1$. \hat{I}_X , \hat{I}_Y and \hat{I}_Z are operators of the nuclear spin I and e is the elementary charge. If the surroundings of a nucleus have cubic symmetry, the quadrupole coupling vanishes since $V_{XX}=V_{YY}=V_{ZZ}$.

The complete interaction Hamiltonian is given by the sum of the Zeeman Hamiltonian \mathcal{H}_M (*magnetic interaction*) and the quadrupolar Hamiltonian \mathcal{H}_Q (*quadrupolar interaction*) with

$$\mathcal{H} = \mathcal{H}_M + \mathcal{H}_Q, \quad (2.19)$$

$$\mathcal{H}_M = \hbar\omega_0 \hat{I}_Z. \quad (2.20)$$

$\omega_0 = -\gamma_n B_0$ is the Larmor frequency and γ_n the gyromagnetic ratio of the observed nucleus.

With the assumption, that the quadrupole interaction is small compared to the Zeeman interaction, perturbation theory can be applied to calculate the energy levels of the spin system. Because of the quadrupolar perturbation, the energy levels are not any more equidistant like for pure Zeeman interaction. Instead of a single resonance frequency, several transition frequencies (*satellites*) with $\Delta m = 1$ are present. $|m\rangle$ describes the eigenstates of the Zeeman Hamiltonian with $m = -I, I+1 \dots I-1, I$.

The first order satellite transition frequencies are given by [20, 23, 139]

$$\omega_{m,m+1} = \omega_0 + \frac{\omega_Q}{2} [3 \cos^2 \beta - 1 - \eta \sin^2 \beta \cos 2\alpha] \left(m + \frac{1}{2} \right) \quad (2.21)$$

with α and β being the Euler angles of the magnetic field \mathbf{B}_0 in the principal axis system of the quadrupole tensor. This results in quadrupolar spectra of first order with pairs of lines being symmetrical with respect to ω_0 . Additionally, a central transition line in the centre (at ω_0) is observable for half integer spins. The intensities of the various lines are proportional to $|\langle m | I_X | m-1 \rangle|^2$ and given in Table 2.1 for some spin quantum numbers I .

Spin I	Central and satellite transition intensities	β_{opt} [35]
3/2	3:4:3	64°
5/2	5:8:9:8:5	40°
7/2	7:12:15:16:15:12:7	30°

Table 2.1: Line intensities of the central and satellite transitions for various quadrupolar spin I . β_{opt} represents the optimum rotation angle to obtain the highest quadrupolar spin echo amplitude in a $\pi/2 - \beta$ experiment.

Quadrupolar Excitations

A one pulse FID (free induction decay) experiment for spin $I = 1/2$ nuclei is mainly determined by the Rabi frequency ω_{rf} and duration τ_{rf} of the pulse and a maximum FID signal intensity is obtained for $(\omega\tau)_{\text{rf}} = \pi/2$. Due to the additional presence of satellite transitions in quadrupolar spectra, this simple rule does not hold any more. Excitations of quadrupolar spectra can be divided into *selective* and *non selective* excitations. The case of a nonselective excitation of a quadrupolar spectrum is characterized by [36]

- a pulse which has to be strong compared with the internal interactions

$$|\mathcal{H}_{\text{rf}}| \gg |\mathcal{H}_Q|, |\mathcal{H}_{\text{dipolar}}|, |\mathcal{H}_{\text{CSA}}| \quad (2.22)$$

- a sufficiently large bandwidth of excitation $\delta\nu_{\text{rf}}$ and the probe $\delta\nu_{\text{probe}}$:

$$\delta\nu_{\text{rf}}, \delta\nu_{\text{probe}} \gg |\mathcal{H}_Q|/\hbar, |\mathcal{H}_{\text{dipolar}}|/\hbar, |\mathcal{H}_{\text{CSA}}|/\hbar. \quad (2.23)$$

For non selective excitations, the dependence of the FID intensity $G_{m,m+1}$ is sinusoidal on ω_{rf} and τ_{rf} for all transitions with

$$G_{m,m+1} \sim \sin((\omega\tau)_{\text{rf}}) \quad (2.24)$$

and the maximum FID intensity is obtained for $(\omega\tau)_{\text{rf}} = \pi/2$, similarly to excitations in a spin 1/2 system.

In the case of sufficiently large quadrupole splittings with $|\mathcal{H}_Q| \gtrsim |\mathcal{H}_{\text{rf}}|$, a selective excitation of transitions can be obtained by applying a *soft* pulse. In this case, the intensity of the FID is modified to

$$\tilde{G}_{m,m+1} \sim \sin(W(\omega\tau)_{\text{rf}}) = \sin((\tilde{\omega}\tau)_{\text{rf}}) \quad \text{with} \quad (2.25)$$

$$W = \sqrt{(I(I+1) - m(m+1))}. \quad (2.26)$$

Comparison with Eq. (2.24) shows that for a selective excitation of the central transition ($m = -1/2$), the nutation frequency is enhanced by

$$\tilde{\omega}_{\text{rf}} = (I + 1/2)\omega_{\text{rf}}. \quad (2.27)$$

This nutation frequency enhancement can be used as a criterium for the selectivity of pulses by comparing appropriate to pulse length in aqueous solutions of the same quadrupolar nuclei. In solutions, the quadrupolar satellites are usually hidden within the central transition and a non selective excitation of the complete spectrum is achieved even with soft pulses.

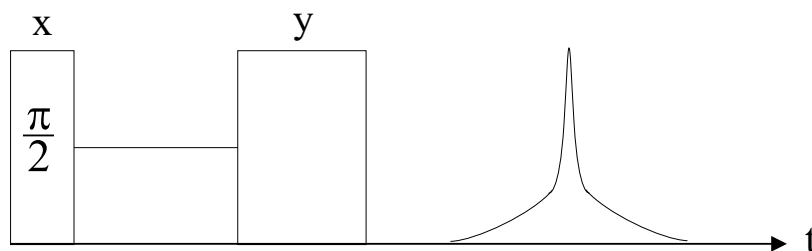


Figure 2.4: Pulse sequence to create the quadrupolar echo. The $(\pi/2)_x$ -pulse is followed by a delay τ , after which a second $(\beta)_y$ -pulse is applied. The spin echo intensity at $t = 2\tau$ depends strongly on the pulse angle β .

Magnetic and Quadrupolar Echoes

Due to quadrupolar broadenings and wide distributions of resonances, it is often difficult to completely record NMR spectra of quadrupolar nuclei within a simple FID experiment (spectrometer dead time problem). This can be bypassed using spin echo techniques. The treatment of spin echo phenomena in quadrupolar nuclei can be carried out using the operator formalism introduced in detail in [23].

The typical spin echo sequence is shown in Fig. 2.4. The pulse sequence consists of a set of two rf pulses near or at the Larmor frequency of the spin system delayed by the time τ with respect to each other. For half-integer spins, the primary echo at $t = 2\tau$ separates into a central transition contribution (broad pedestal) and a satellite contribution (narrow signal). Besides this primary echo, under specific conditions additional multiple echoes are expected.

Considering the primary echo it can be shown, that in the delta pulse approximation the response function $G(t)$ describing the time dependent behavior of the magnetization after the last pulse, can be separated into two parts:

$$G(t) \sim C_M(I, \beta) + C_Q(I, m, \beta). \quad (2.28)$$

The echo amplitude factor $C_M(I, \beta)$ describes the central (magnetic) transition and $C_Q(I, m, \beta)$ describes the quadrupolar satellite transitions. Remarkable is the strong dependence of the magnetic and quadrupolar echo amplitudes on the pulse angle β of the second pulse.

As shown in Fig. 2.5, by choosing an appropriate pulse angle, echo signals from central and satellite transition contributions can be separated. The maximum (primary) spin echo amplitude is obtained at the optimum rotation angle β_{opt} , which is listed for various spin-quantum numbers I in Table 2.1.

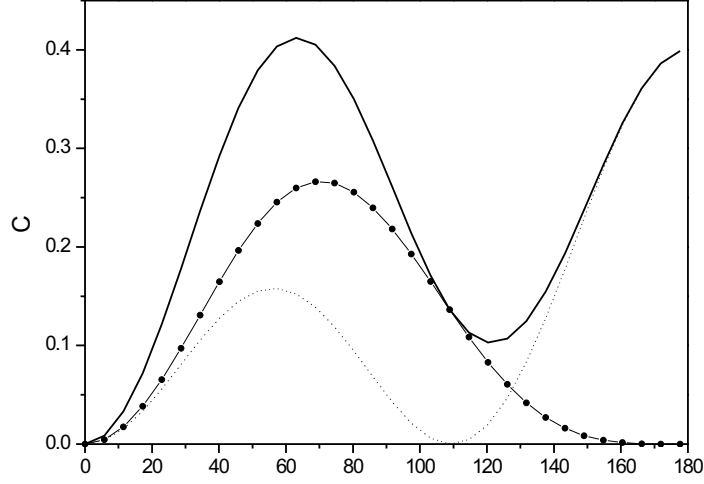


Figure 2.5: Echo amplitudes C for a spin $3/2$. β is the rotation angle of the second rf pulse. The solid line represents the sum of the magnetic contributions (dotted line) and quadrupolar contributions (point-dash line).

Multiple Echoes

As already mentioned, besides the primary echo at $t = 2\tau$, additional multiple echoes can show up in multi-level systems like quadrupolar nuclei. The full response function for the quadrupolar echo is given by [23]

$$G(t > \tau) \sim \sum_{m_1, \dots, m_4} A_{m_1, \dots, m_4} G_{m_1, \dots, m_4}(t, \tau) \quad \text{with} \quad (2.29)$$

$$G_{m_1, \dots, m_4}(t, \tau) = \exp\left(i\frac{\omega_Q}{2} [(t - \tau)(m_1^2 - m_2^2) + \tau(m_4^2 - m_3^2)]\right) \times \exp(i\delta\omega [(t - \tau)(m_1 - m_2) + \tau(m_4 - m_3)]) . \quad (2.30)$$

A_{m_1, \dots, m_4} are prefactors and m_i is given by $-I \leq m_1, \dots, m_4 \leq +I$. Multiple echoes appear only in case of a fairly homogeneous local field distribution $p(\delta\omega)$ and spin $I > 3/2$. By neglecting the distribution of local fields and offsets of type $\delta\omega$, the condition for echo formation at time t can be extracted from Eq. (2.30) to

$$\frac{t - \tau}{\tau} = \frac{m_4^2 - m_3^2}{m_2^2 - m_1^2} = k > 0 \quad (m_2^2 \neq m_1^2). \quad (2.31)$$

Spin echoes are only observable, if matrix elements of corresponding transitions do not vanish. This limits Eq. (2.31) to $m_2 = m_1 - 1$ and the echo condition can be rewritten to a more restricted form

$$\frac{t - \tau}{\tau} = \frac{m_4^2 - m_3^2}{2m_1 - 1} = k > 0. \quad (2.32)$$

Spin I	Quadrupolar echo positions, multiples of τ
3/2	2
5/2	3/2, 2, 5/2*, 3, 4*
7/2	4/3, 3/2, 5/3, 2, 5/2, 8/3*, 3, 7/2*, 4, 6*, 7*

Table 2.2: Echo positions for multiple quadrupolar echoes occurring at multiples of τ for different nuclear spin I . The (*) marked echo positions correspond to forbidden echoes.

In the limit $\omega_{\text{rf}} \gg \omega_Q$, Eq. (2.32) becomes additionally restricted to $m_4 = m_3 \pm 1$, transitions with $m_4 \neq m_3 \pm 1$ are termed *forbidden*.

This restriction can be eased for $\omega_{\text{rf}} \approx \omega_Q$. In the case of spin $I = 3/2$ this leads to the formation of only one echo, the usual Hahn echo at $t = 2\tau$. In case of spin $I = 5/2$, in principle 5 echoes are expected with 2 of them being forbidden. For spin $I = 7/2$, 7 allowed and 4 forbidden echoes can be calculated. The corresponding echo positions are summarized in Table 2.1.5.

2.1.6 Spectra Under Molecular Motion

Definition of the n -th Moment

The n th moment M_n of a shape function $f(\omega)$ with a maximum at a frequency ω_0 is given by

$$M_n = \frac{\int_{-\infty}^{\infty} (\omega - \omega_0)^n f(\omega) d\omega}{\int_{-\infty}^{\infty} f(\omega) d\omega}. \quad (2.33)$$

Two commonly used line shapes are the (1) Gaussian and the (2) Lorentzian line shape.

- (1) A Gaussian line shape can be described by

$$f(\omega) = \frac{1}{\Delta\sqrt{2\pi}} \exp\left(-\frac{(\omega - \omega_0)^2}{2\Delta^2}\right). \quad (2.34)$$

It has a second moment given by $M_2 = \Delta^2$ and the corresponding half width at half height equals $\delta = \Delta\sqrt{2\ln 2} \simeq 1.18\Delta$.

- (2) Very often in FID experiments the magnetization follows a single exponential decay vs. time described by

$$G(t) = \exp(-t/T_2'). \quad (2.35)$$

In general, the spin-spin relaxation rate $1/T_2'$ has the form

$$\frac{1}{T_2'} = \frac{1}{T_2} + \frac{1}{2T_1} \quad (2.36)$$

with $1/T_1$ being the spin-lattice relaxation rate. Spin-lattice relaxation is negligible since usually, $1/T_2 \gg 1/T_1$ and for Eq. (2.35), the corresponding Fourier transformed spectrum is a Lorentzian lineshape described by

$$f(\omega) = \frac{1}{\pi} \frac{\delta}{\omega^2 + \delta^2}, \quad (2.37)$$

where δ is the half width at half intensity corresponding to the spin-spin relaxation rate $\delta = 1/T_2'$.

No second or higher moment can be defined for a Lorentzian shape, since the corresponding integrals diverge. However, by cutting off the line very far in the wings, finite values of M_2 (describing the width of the line) can be obtained [24].

Motional narrowing

At low temperatures in the absence of molecular motions, the rigid lattice linewidth $\delta\omega_0$ is determined by various static interactions like dipolar couplings, quadrupolar couplings, or couplings to conduction electrons or paramagnetic impurities. The length and orientations of the vectors \mathbf{r}_{jk} describing the relative positions of the spins do not change in time. In a powder average, the second moment M_2 of a rigid molecule exhibiting pure dipolar couplings can be expressed by [20]

$$M_2 = \frac{6}{5} I(I+1) \left(\frac{\mu_0}{4\pi} \right)^2 \gamma_n^4 \hbar^2 \sum_{j < k} \frac{1}{r_{jk}^6}. \quad (2.38)$$

The sum runs over all spin-spin distances r_{jk} in the molecule.

However, in the case of molecular motion, the vectors \mathbf{r}_{jk} are not static any more. The spins are in rapid relative motion and only an average value of the fluctuating local field will be observed, leading to a motional narrowing of the line. The rate of these fluctuations can be described by a correlation rate τ_c^{-1} and the criterion for motional narrowing is given by

$$\langle \delta\omega_0^2 \rangle \tau_c^2 \ll 1. \quad (2.39)$$

It can be shown, that the narrowed linewidth $\delta\omega$ is correlated with the second moment $M_2 = \delta\omega_0^2$ of the rigid lattice by the implicit formula [20]

$$\delta\omega^2 = \delta\omega_0'^2 + \delta\omega_0^2 \frac{2}{\pi} \arctan[\alpha\delta\omega\tau_c]. \quad (2.40)$$

α is a phenomenological numerical factor of order unity and $\delta\omega_0'^2$ takes into consideration, that upon motional narrowing not all interactions become completely averaged over the motion.

Typically, τ_c can be assumed to follow an Arrhenius like activated behavior with

$$\tau_c = \tau_0 \exp\left(\frac{\Delta E}{k_B T}\right), \quad (2.41)$$

where τ_0 is the value of τ_c at infinite temperature and ΔE the activation energy.

2.2 Relaxation Effects in NMR

Spin systems excited into a quantum state are subject to couplings to the environment. Fluctuating magnetic interactions introduce irreversible processes, called relaxation or decoherence of the spin system. Possible interactions or couplings are of scalar, dipolar or quadrupolar order. In the following, various kinds of relaxation are introduced, starting with relaxation due to electron-nuclear coupling, followed by relaxation due to fluctuating homonuclear dipole-dipole interactions. Since in this thesis, quadrupolar relaxation effects were not dominantly observed, they will not be addressed here.

2.2.1 Hyperfine Relaxation

In a metal, spin-lattice relaxation is usually dominated by the hyperfine interaction between conduction electrons and nuclear spins. This relaxation process can be treated as a nuclear transition involving a simultaneously elastic electron scattering process.

As shown for the case of the Knight shift, both the isotropic and the anisotropic hyperfine coupling play an important role for electron-nuclear interactions. For appreciable s character of the conduction electron wave function, the isotropic Fermi contact interaction is dominating, whereas for electrons with non- s character the distant dipolar hyperfine coupling is more important.

A relation between the spin-lattice relaxation rate $1/T_1$ and the Knight shift can be given by the Korringa relation [37]

$$T_1 T K_{iso}^2 \left(1 + \frac{1}{2}\varepsilon\right) C_0 S_K = 1 \quad \text{with} \quad (2.42)$$

$$C_0 = 4\pi \frac{k_B}{\hbar} \left(\frac{\gamma_n}{\gamma_e}\right)^2.$$

The Korringa relation is valid in both cases of isotropic and dipolar hyperfine interactions. The dimensionless Korringa enhancement factor S_K equals ~ 1 in conventional metals. Its deviation from unity is a sign of the importance of electron-electron interactions (electronic correlation). Using the definition $d \equiv d_{zz} - a_{iso} = d_{33}$ which describes the dipolar hyperfine coupling, ε is given by

$$\varepsilon = \frac{d_{33}}{a_{iso}^2} = \frac{d^2}{a_{iso}^2} \stackrel{\text{Eq. (2.11)}}{=} \frac{(K_{zz} - K_{iso})^2}{K_{iso}^2}. \quad (2.43)$$

By relating the Knight shift in Eq. (2.11) with the spin susceptibility of a Fermi liquid (2.10), a modified expression for the Korringa relation (2.42) is obtained:

$$\frac{1}{T_1 T} = \pi k_B \hbar S_K a_{iso}^2 \left(1 + \frac{1}{2}\varepsilon\right) n(\varepsilon_F)_{iso}^2 \quad (2.44)$$

$$= \pi k_B \hbar S_K (a_{iso}^2 + 2d_{11}^2) n(\varepsilon_F)_{iso}^2. \quad (2.45)$$

Assuming a pure dipolar hyperfine coupling with electrons in the p_z -orbital described by Eq. (2.12) and setting $S_K = 1$ since in ordinary metals, the spin-lattice relaxation expression for dipolar hyperfine interaction ($d_{11} = A_{dip}$) can be calculated to [4,30,33]

$$\frac{1}{T_1 T} = \frac{2\pi k_B}{\hbar} A_{dip}^2 n(\varepsilon_F)^2 \quad \text{with} \quad (2.46)$$

$$A_{dip} = \frac{2}{5} \frac{\mu_0}{4\pi} \gamma_n \gamma_e \hbar^2 \left\langle \frac{1}{r^3} \right\rangle. \quad (2.47)$$

All the above expressions for spin-lattice relaxation were derived for a powder average since both, isotropic and dipolar hyperfine interaction depend on the orientation angle of the magnetic field. This powder average leads to a non mono-exponential magnetization recovery in a spin-lattice relaxation measurement. Upon excitation of the spin system with hard pulses covering the total spectral width, the magnetization recovery is given by a sum of exponentials with different T_1 values [37].

2.2.2 Scalar Spin-Spin Coupling

In the last section the nuclear hyperfine coupling of a nuclear spin with conduction electron spins was treated as a scattering process with an ensemble of conduction electrons. Now the case of an interaction between a single nuclear spin I and a single electron spin S will be addressed. Only for an electron wave function having a non-vanishing value at the position of the nucleus, a scalar spin-spin coupling can exist.

Scalar couplings between different spins cause relaxation due to the time dependence of the spin-spin coupling A_{IS} (called scalar relaxation of the first kind). In the following it is assumed, that the spin state of the spin S fluctuates fast in time compared with the strength of the spin-spin coupling A_{IS} . The source of such a spin state fluctuation could be a rapid spin-lattice relaxation of the spin S with the consequence, that only the average value of the spin-spin coupling is observed. If the spin-spin interaction is not too strong, the coupling can be treated as a small perturbation on the Zeeman energy of the spin I . Resonant transitions between nuclear Zeeman levels can be induced and detected.

Spin-Spin Relaxation

By applying standard relaxation theory, Abragam [20] calculated the corresponding spin-spin relaxation rate to

$$\frac{1}{T_2} = \frac{A^2}{3} S(S+1) \left[\frac{\tau_{1e}}{1 + (\omega_I - \omega_S)^2 \tau_{1e}^2} + \tau_{1e} \right] \quad (2.48)$$

with τ_{1e} describing the spin-lattice relaxation rate of the spin S , $\omega_{I/S}$ being the Larmor frequencies of the corresponding spins I and S and A describing the spin-spin coupling strength.

If S is an electron spin with the spin quantum number $S = 1/2$, the first term in Eq. (2.48) can be neglected for higher magnetic fields, since $\omega_S \gg \omega_I$. Therefore, the transversal relaxation rate of a nuclear spin due to scalar coupling to a fluctuating electron spin can be written as

$$\frac{1}{T_2} = \frac{A^2}{4} \tau_{1e}. \quad (2.49)$$

It is usually considered that the temperature dependence of the electron spin-lattice relaxation time τ_{1e} due to spin-phonon interactions is to follow the law $\tau_{1e} \sim T^{-1}$ for a direct process, while stronger dependence of τ_{1e} on temperature is typical for a Raman process [38].

Spin-Lattice Relaxation

The spin-lattice relaxation rate for relaxation due to scalar electron-nuclear coupling is composed of several functions of type [23]

$$J_i(\omega_i) \sim \frac{\tau_e}{1 + \omega_i^2 \tau_e^2}. \quad (2.50)$$

However, electron-nuclear coupling terms comprising $\omega_i = \omega_S - \omega_I$ can be neglected due to the high electron spin Larmor frequency ω_S . The final spin-lattice relaxation rate for relaxation due to scalar electron-nuclear coupling can be written as

$$\frac{1}{T_1} = \frac{2A^2}{3} S(S+1) \left[\frac{\tau_{1e}}{1 + \omega_I^2 \tau_{1e}^2} \right] \quad (2.51)$$

It is important to note, that both, Eq. (2.48) and Eq. (2.51) only consider dipolar and isotropic exchange interactions, whereas antisymmetric tensor components are neglected.

2.2.3 Dynamic Relaxation - Weak Collision

As already mentioned, local magnetic or electric field fluctuations at the site of a nucleus can induce transitions among Zeeman levels and thus will effect the spin-lattice relaxation rate $1/T_1$. The changes in the local field can be caused by molecular or lattice dynamics and the mean time between different sterically states of the molecule is described by the correlation time τ .

In the case the correlation rate $1/\tau$ of a molecular motion exceeds strongly the spin interaction coupling, that is $1 \gg \delta\omega\tau$ ($\tau \ll T_2$), many atomic jumps are required to relax the spin system. Relaxation in this limit is described by a *weak collision theory*, originally developed by Bloembergen, Purcell and Pound (BPP), who treated the fluctuating interaction Hamiltonian as a perturbation on the Zeeman levels [39]. The stochastic nature of the fluctuating spin interactions can be generally described by introducing the memory function $K_a(t)$, a rapidly decaying function of time given by [23]

$$K_a(t) = \frac{\left(\left[\hat{I}_a, \Delta \hat{\mathcal{H}}_{\text{int}}(0) \right]_- \left[\hat{I}_a, \Delta \hat{\mathcal{H}}_{\text{int}}(t) \right]_- \right)}{\hbar^2 \left(\hat{I}_a | \hat{I}_a \right)} \quad (2.52)$$

(The rectangular brackets $[...]_-$ are commutator relations). The memory function contains the interaction Hamiltonians $\Delta \hat{\mathcal{H}}_{\text{int}}(t)$ which describe the (averaged) time

dependence of the perturbation on the spin system. The appropriate spin relaxation rate is then given by

$$\frac{1}{T_a} = \text{Re} \int_0^\infty K_a(t) dt \sim J(\omega), \quad (2.53)$$

$$J(\omega) = \text{Re} \int_0^\infty G(t) \exp(-i\omega t) dt. \quad (2.54)$$

The spectral density $J(\omega)$, which is the Fourier transform of the corresponding autocorrelation function $G(t)$, describes the spectral distribution of the fluctuating spin interactions.

Depending on the type of spin interaction and model of molecular motion, $K_a(t)$ has to be adapted individually. A detailed approach is given in [23]. For the case of Debye fluctuations typically occurring for many types of isotropic molecular motion processes, the spectral density $J(\omega)$ is provided by the Lorentzian distribution

$$J(\omega_0) = \frac{\tau_c}{1 + \omega_0^2 \tau_c^2}, \quad (2.55)$$

and the temperature dependence of the correlation time τ_c can be described by an Arrhenius activated process

$$\tau_c(T) = \tau_0 \exp\left(\frac{\Delta E}{k_B T}\right). \quad (2.56)$$

Evidently, the maximum in the spectral density and thus in the relaxation rate occurs for $\omega_0 \tau_c = 1$ (*BPP maximum*). This can be understood illustratively by considering that, since the nuclei precess at the Larmor frequency ω_0 , the fluctuating fields will appear static to the precessing nuclei, when $1/\tau = \omega_0$. Such static fields will be highly effective in spin-lattice relaxation and thus give rise to a T_1 minimum (BPP maximum).

For the sake of completeness, the spin-lattice relaxation relations for dipolar and quadrupolar relaxation (case of isotropic molecular reorientations) are given here:

$$\frac{1}{T_1} = 2a_{d/Q} [J(\omega_0) + 4J(2\omega_0)]. \quad (2.57)$$

For dipolar couplings, the prefactor a_d is given by

$$a_d = \frac{1}{5} I(I+1) d^2 \quad (2.58)$$

with the dipolar coupling constant d defined by

$$d = \frac{\mu_0 \gamma_I^2 \hbar}{4\pi r^3} \quad (2.59)$$

r is the distance a pair of like spins with gyromagnetic ratio γ_I is separated. For pure dipolar relaxation, Eq. 2.60 can be modified to

$$\frac{1}{T_1} = \frac{2}{3}M_2 [J(\omega_0) + 4J(2\omega_0)] \quad (2.60)$$

with M_2 describing the second moment of a dipolar broadened line [24].

For quadrupolar relaxation, a_Q is given by

$$a_Q = \frac{1}{300}\omega_Q^2(2I + 3)(2I - 1) \quad (2.61)$$

with the quadrupolar coupling constant ω_Q given by Eq. (2.17) [23].

2.2.4 Dynamic Relaxation - Strong Collision

The range of validity of the weak collision BPP theory sketched above is for $1 \gg \delta\omega\tau$, which in particular includes relaxation processes due to fast motions or fluctuations. Even though, slow motions in conventional magnetic fields of the order of several Tesla leave spin-lattice relaxation almost unaffected (as the accompanying couplings become quiet ineffective), relaxation can still be described by the standard weak collision theory.

However, in case of slow motions in weak applied magnetic fields, the correlation rate of the molecular motion decreases to the order of the spin-spin coupling strength. With $1 \leq \delta\omega\tau$, $\tau \geq T_2$, the BPP theory does not hold any more. Note that the term *weak applied fields* applies to both, weak external magnetic fields as well as considerations in the rotating frame.

The first reason for the failure of the BPP theory is, that the fluctuating interaction Hamiltonian is not any more a perturbation on the Zeeman levels. The correct eigenstates are now determined by the spin-spin couplings. The second reason for the failure of BPP originates from the fact, that $1/\tau \leq \delta\omega$. This results in a very high efficiency of interactions with fluctuations: every atomic jump (or fluctuation) relaxes the spin system (*strong collision theory*). This is different from the weak collision case, where only an average due to many fluctuations caused the relaxation.

Ailion [40–42] treated the case of a diffusion-induced modulation of dipolar couplings in the rotating frame using the assumption of sudden approximation. This assumption includes, that the actual time a nucleus spends in a jump is so short compared to a nuclear precession period that it can be assumed, all spins have the same orientation just after a jump as they do just before a jump. The spin-lattice relaxation rate in the rotating frame $1/T_{1\rho}$ was obtained to

$$\frac{1}{T_{1\rho}} = \frac{1}{T_1'} + \frac{2(1-p)}{\tau_{sc}} \frac{H_D^2}{H_1^2 + H_D^2}. \quad (2.62)$$

$1/T_1'$ is the spin-lattice relaxation rate due to all mechanisms other than molecular jumping, H_D is the dipolar contribution to the local field and H_1 the external rf field. The parameter p represents the fact that the local field is not completely randomly after a jump. It depends on the local lattice geometry and was calculated e.g. for a powder averaged BCC-lattice to $p = 0.26$ [43].

$1/\tau_{sc}$ ('sc'=strong collision) is given by

$$\frac{1}{\tau_{sc}} = \frac{N_v}{N\tau_v}. \quad (2.63)$$

Here, N is the number of nuclei per unit volume, N_v the number of available vacancies and τ_v the mean time a nucleus spends between jumps.

In order to adapt Eq. (2.62) for spin-spin relaxation T_2 , which occurs in 'zero' magnetic field, H_1 has to be set to zero. In the strong collision case $1/T_2$ can be described by

$$\frac{1}{T_2} = \frac{1}{T_2'} + \frac{2(1-p)}{\tau_{sc}}. \quad (2.64)$$

This approach is possible since the derivation of Eq. (2.62) is only based upon the assumption that H_1 is sufficiently small to allow cross relaxation between the Zeeman H_1 systems and dipolar H_D systems prior to each jump (theory of spin temperature).

2.2.5 Stimulated Echo

The decay of solid echo intensity upon variation of τ in a $\pi/2 - \tau - \pi/2 - \tau -$ echo pulse sequence can be used to measure the spectral density of slow spin fluctuations. Thereby, solid echo probes the transversal spin-relaxation in the $x - y$ plane. Longitudinal relaxation due to slow spin fluctuations can be investigated using a three-pulse stimulated echo sequence $\pi/2 - t_1 - \pi/2 - t_2 - \pi/2 - t_1 -$ echo, where the time delay t_1 is fixed and t_2 is varied [44–46].

The first $\pi/2$ pulse creates a transverse magnetization in the rotating frame. The second $\pi/2$ pulse stores the phase-encoded transversal magnetization along the z -axis (*population grating*), where during the t_2 period it is subject to T_1 relaxation only. The spin polarization and spin alignment are transferred by the third $\pi/2$ pulse into coherent transverse states, which then evolve in a reverse manner to that occurring during the first evolutionary period t_1 . After a delay time t_1 , the spin states are refocussed and an echo is formed.

However, if spin fluctuations during the t_2 period cause perturbation of the phase-encoded magnetization pattern, an incomplete refocusing of the spin packets at the moment of the stimulated echo detection occurs. In such a case increasing of t_2 leads to an exponential decay of the stimulated echo with a rate $1/T_1^{stim}$ due to increasing modification of the population grating [46–48].

The response function $G(t > t_1 + t_2)$ consists of six different contributions causing several unwanted echoes besides the genuine stimulated echo at $t = t_2 + 2t_1$ [23]. Cancellation of all unwanted signals can be achieved by the phase cycling sequence shown in Tab. 2.3.

φ_1	φ_2	φ_3	φ_4
0	0	$3\pi/2$	0
$\pi/2$	π	π	0
π	0	$\pi/2$	0
$3\pi/2$	π	0	0

Table 2.3: Phase cycling scheme for the stimulated echo $\pi/2(\varphi_1) - t_1 - \pi/2(\varphi_2) - t_2 - \pi/2(\varphi_3) - \text{acquisition}(\varphi_4)$.

2.3 ^{13}C NMR Shifts in Carbon Nanotubes

NMR of SWNT can be found only in a limited number of papers. Thereby the major topics can be subdivided in ^{13}C NMR of pristine SWNT [34, 190, 193–199, 242], NMR of alkali intercalated SWNT [129, 137, 138, 140, 164, 173] and NMR of hydrogen storage in SWNT [201–208]. In the following, the key features of pristine SWNT will be summarized.

2.3.1 Spectra and Sample Purity

Fig. 2.6 shows typical static and MAS ^{13}C NMR spectra of pristine SWNT. The static spectrum shows a powder lineshape with principal tensor values $\delta_{xx} = 240$ ppm, $\delta_{yy} = 171$ ppm and $\delta_{zz} = -36$ ppm and the main peak around 183 ppm. Such values are typical for sp^2 carbons belonging to aromatic materials like frozen benzene, C_{60} and graphene and confirm the aromatic character of the SWNT.

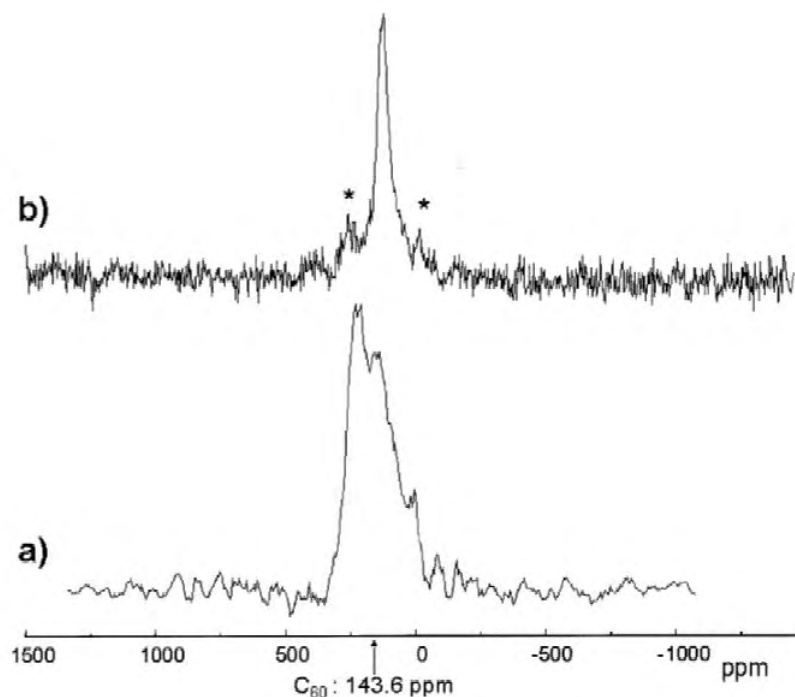


Figure 2.6: ^{13}C MAS high resolution room temperature spectrum (a) and static spectrum at 170 K (b) of purified SWNT, recorded at a Larmor frequency of $\omega_0 = 100.6$ MHz. The symbols * indicate the sidebands. The SWNT are 10% ^{13}C enriched and produced using the electric arc method with 1 at% Y and 4 at% Ni as catalyst [34].

For comparison, for C_{60} the principal tensor values were reported to $\delta_{xx} = 213$ ppm, $\delta_{yy} = 183$ ppm and $\delta_{zz} = 33$ ppm with an isotropic shift of 143 ppm [37].

The MAS spectrum in Fig. 2.6 consists of one broad isotropic line (FWHM ~ 50 ppm), centered around 126 ppm. The measured isotropic line position corresponds very well with the isotropic value calculated using the principal tensor values $\delta_{iso} = 1/3(\delta_{xx} + \delta_{yy} + \delta_{zz}) = 125$ ppm.

The line broadening is usually interpreted as a distribution of several isotropic lines related to the different chiralities and diameters of SWNT present in a sample. The static spectrum shows about 300 ppm of CSA (chemical shift anisotropy) which is again typical for sp^2 carbons belonging to curved graphene sheets.

Of particular importance is the purity of the investigated SWNT sample. Nanoparticles like amorphous carbons, free para- or ferromagnetic catalyst clusters, as well as metallic catalysts encapsulated in graphitic shells disturb the NMR experiments since they drastically affect the homogeneity of the external magnetic field. Without purification, the MAS spectrum in Fig. 2.6 would show a very broad line with about 1500 ppm of anisotropy.

Thus, the prerequisite for obtaining well defined NMR spectra of SWNT is either purification of pristine samples in order to remove metallic catalyst particles or even the production of SWNT containing non-ferromagnetic catalysts. The disadvantage of SWNT purification is the modification of the electronic properties of SWNT due to nanotube-sidewall functionalization, the formation of defects in the SWNT and even the possibility of nanotube-opening by oxidative end-cap removal.

As an example, Fig. 2.7 shows a high-resolution ^{13}C NMR spectrum of purified SWNT recorded with proton-decoupling in order to remove ^{13}C NMR line broadenings due to dipolar coupling with ^1H nuclear spins. Upon SWNT purification with 65% nitric acid treatment and subsequent chromatographic separation of SWNT and nanoparticles, the NMR line structure becomes drastically changed.

Besides a modification of the sp^2 line, the appearance of an additional -COOH line as well as a sp^3 line is observable. This is a clear signature of SWNT functionalization and existence of a large variety of defects. Even though, reversibility of the functionalization by high temperature treatment was proven, a regeneration of removed SWNT end-caps is rather improbable [194].

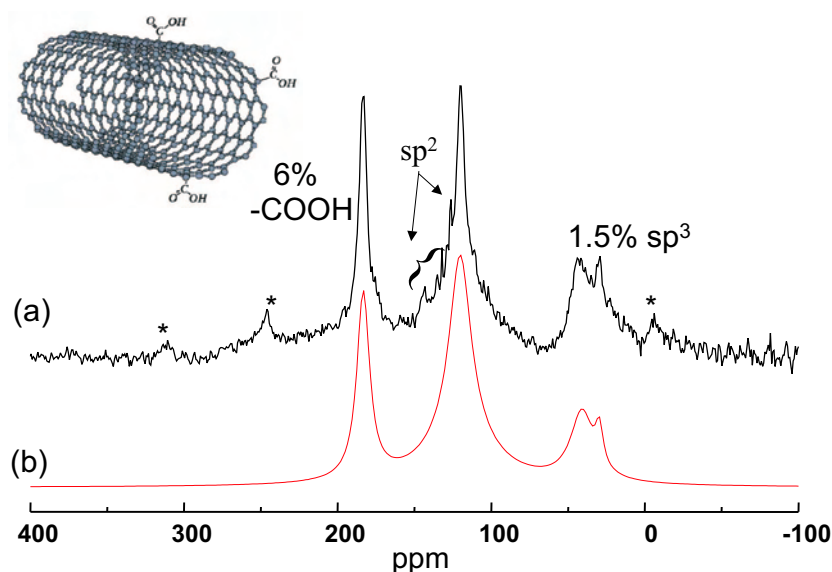


Figure 2.7: ^{13}C proton decoupled MAS NMR spectrum of purified SWNT (a) and its deconvolution with five Lorentzian lines (b) [194].

In order to overcome these problems, the usage of SWNT produced with only small amounts of catalysts is preferable to a purification process. Already molar proportions of 89.92% C, 0.54% Ni and 0.54% Y catalysts have shown to provide reasonable SWNT material suitable for NMR investigations. Best results can be obtained by using non-ferromagnetic Pt/Rh catalysts. With molar proportions of 96.1% C, 1.1% Pt and 2.8% Rh, corresponding ^{13}C NMR spectra show no significant difference compared to high quality Ni/Y SWNT.

By performing a *Raman selection* of pristine Pt/Rh SWNT (eg. by only selecting grains of SWNT that show an intense Raman RBM-signal using the Raman microscope), high quality SWNT can be obtained that are particularly suitable for NMR investigations.

2.3.2 Shift Interactions in SWNT

Theoretical calculations have shown that the total degree of carbon $\text{sp}^2 - \text{sp}^3$ -rehybridization required to form the curvature of a nanotube surface is rather small, constant and independent of nanotube chiralities. Therefore, the Pople part contribution to chemical shifts in SWNT should be more or less negligible. This is different from the chemical shift behavior in fullerenes, where the hybridization Pople part is dominant in chemical shifts [4, 194].

Furthermore, the Knight shift contribution in pristine SWNT is rather small and negligible. It depends on the density of states at the Fermi level which, as will be shown later, accounts only for about $n(\varepsilon_F) \sim 0.015$ states/eV \cdot spin \cdot atom in metallic SWNT [210]. Therefore, the difference between the isotropic line position of isolated metallic and semiconducting SWNT is solely determined by the London ring-current shift contribution. This leads to a calculated isotropic line splitting of 12 ppm (Fig. 2.8) [194, 196, 209].

However, this splitting of metallic and semiconducting SWNT ^{13}C NMR lines should be rather difficult to observe, since paramagnetic impurities and defects in SWNT will broaden NMR spectra.

Fig. 2.9 shows the calculated CSA tensor for a powdered mixture of (1/3) metallic and (2/3) semiconducting SWNT since this mixing ratio represents the theoretical composition of a carbon nanotube sample. The metallic nanotubes are of type (10,10) and the semiconducting of type (12,8) SWNT. Depending on the nanotube surface orientation with respect to the external magnetic field, axial, orthoradial and radial London ring-current components contribute differently to the CSA tensor lineshape.

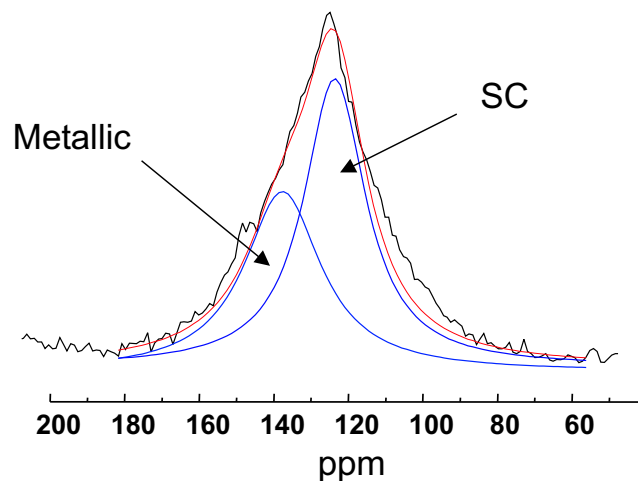


Figure 2.8: Isotropic ^{13}C NMR line at 126 ppm and its deconvolution with two Lorentzian lines attributed to metallic and semiconducting SWNT [34].

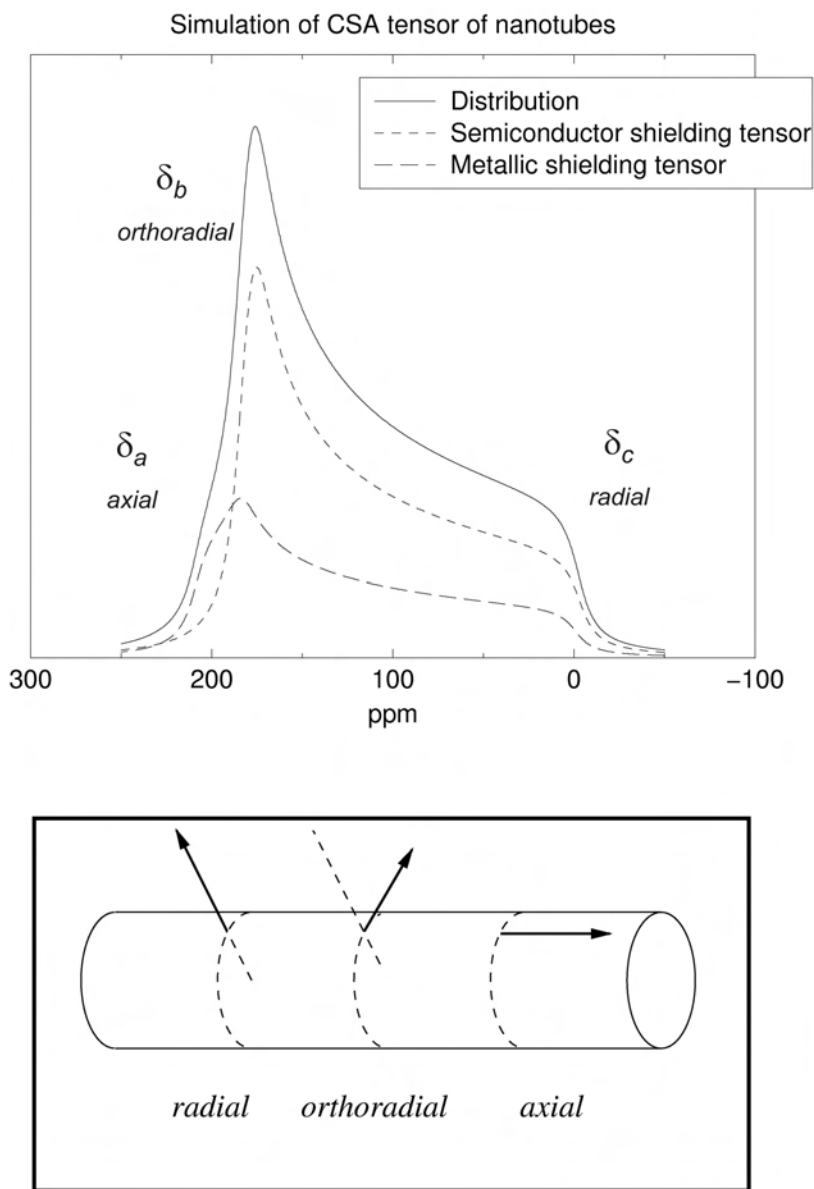


Figure 2.9: Simulation of the CSA tensor of a powdered sample of SWNT (top). Illustration for the three different sources of interatomic currents contributing to the chemical shift tensor (bottom) [209].

Chapter 3

Lithium Intercalated SWNT

This chapter deals with NMR of chemically Li-intercalated SWNT with different stoichiometries. After a brief presentation of the intercalation technique, ^{13}C NMR spectra are discussed and relaxation measurements are used to determine the density of states at the Fermi level. It is shown how the alkali content controls the electronic properties of the metallic SWNT ground state. By using ^7Li and ^1H NMR, the status of Li and the solvent THF concerning their structural and dynamical properties is clarified.

3.1 Sample Preparation and Experimental Conditions

SWNT samples were synthesized by the electric arc method under the conditions described in the references [72,195]. In order to improve the ^{13}C NMR signal to noise ratio, 10% ^{13}C isotope enriched graphitic rods have been vaporized in the presence of a catalyst mixture in the molar proportions 96.8% C, 2.1% Rh and 1.1% Pt. The SWNT bundles were collected directly from the collerette and used as produced without any purification. In order to obtain high quality samples, nanotube grains were selected according their RBM-mode intensity using Raman spectroscopy. A content over 80% in carbon nanotubes was estimated showing an average diameter of 1.4 nm and bundle length of several microns.

Lithium was chemically intercalated in SWNT bundles by using solutions of aromatic hydrocarbons, pure tetrahydrofuran (THF, $\text{C}_4\text{H}_8\text{O}$) and SWNT.

From a chemical point of view, in a first step electrons are transferred from Li to the aromatic hydrocarbons due to their high electron affinity. The Li^+ cations become coordinated by THF molecules and paired with aromatic hydrocarbon anion radicals. In a second step, the solvated Li metal ions are intercalated into the SWNT host by

gradual charge transfer from the aromatic hydrocarbons to the SWNT. Thereby the amount of charge transfer depends on the aromatic hydrocarbons redox potential, which allows to control the stoichiometry of the intercalated Li [92].

Using this mechanism of redox reactions between the radical-anions of fluorenone, benzophenone and naphthalene with Li^+ as counter ion, intercalated SWNT were synthesized with stoichiometries of LiC_{10} , LiC_7 and LiC_6 respectively [125, 161]. All the samples were sealed under high vacuum. The experimental sample preparation conditions, as well as a detailed Raman characterization are described in Ref. [161, 211, 212].

Since raw and chemically untreated SWNT are used as intercalation starting material, the nanotubes are expected to have closed end caps. Therefore, possible Li adsorption sites are only provided by the interstitial channels as well as the surface of a carbon nanotube bundle. The interior space of the present SWNT is supposed to be predominantly inaccessible for penetration by Li atoms.

It was shown that an electronic charge transfer occurs from the aromatic hydrocarbons to the SWNT bundles as expected. Similarly to the intercalation process in other carbon materials, in order to establish charge neutrality, alkali are expected to be cointercalated together with THF molecules, forming a binary or ternary compound $\text{Li}_x(\text{THF})_y\text{C}$ [92, 93, 213–215].

NMR experiments were carried out on a *Bruker ASX200* spectrometer at a magnetic field of 4.7 T and ^{13}C NMR Larmor frequency of 50.3 MHz. High resolution MAS ^{13}C NMR was performed at room temperature with spinning frequencies from 4 kHz up to 9 kHz. ^{13}C NMR static spectra were obtained in the temperature range of 50 – 300 K. ^7Li and ^1H NMR measurements were performed on a home built pulsed NMR spectrometer equipped with a sweep magnet working at 4.2 T and 6.0 T. The following Larmor frequencies have been used: 70.2 MHz for ^7Li and 180.5 MHz for ^1H .

^{13}C and ^1H NMR line shifts were referred to TMS, ^7Li NMR line shifts to 1M LiCl as an external standard. All spectra were recorded using a Hahn echo pulse sequence and Fourier transformation. Spin-lattice relaxation rates T_1^{-1} were obtained using a saturation recovery pulse technique and a Hahn echo as a detection pulse.

3.2 ^{13}C NMR

3.2.1 Spectra

Static and high-resolution MAS ^{13}C NMR spectra of the pristine and Li intercalated SWNT are presented in Fig. 3.1. The static spectra at the top show the evolution of the sp^2 powder pattern lineshape of SWNT under Li intercalation. For pristine SWNT, the spectrum has a CSA of about 600 ppm. A clear reducing of the anisotropy is observed with increasing amount of intercalated Li. The sideband distributions at

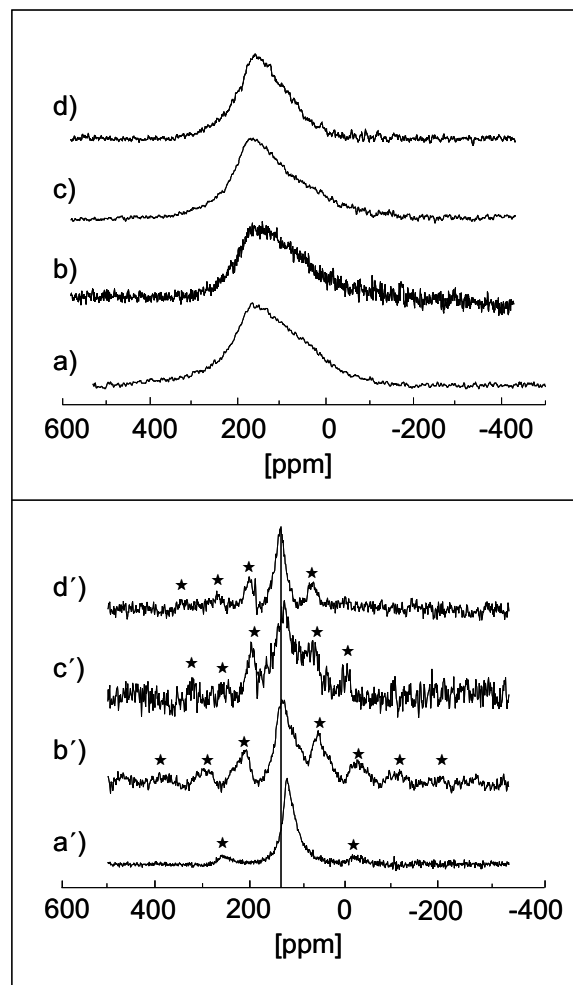


Figure 3.1: ^{13}C NMR spectra recorded at a Larmor frequency of 50.3 MHz at room temperature of pristine SWNT (a) and LiC_x intercalated compounds with $x = 10, 7, 6$, (b), (c) and (d), respectively. Top: static ^{13}C NMR spectra. Bottom: high resolution ^{13}C MAS NMR spectra. The symbols (\star) are for the spinning sidebands. For more details refer to the text.

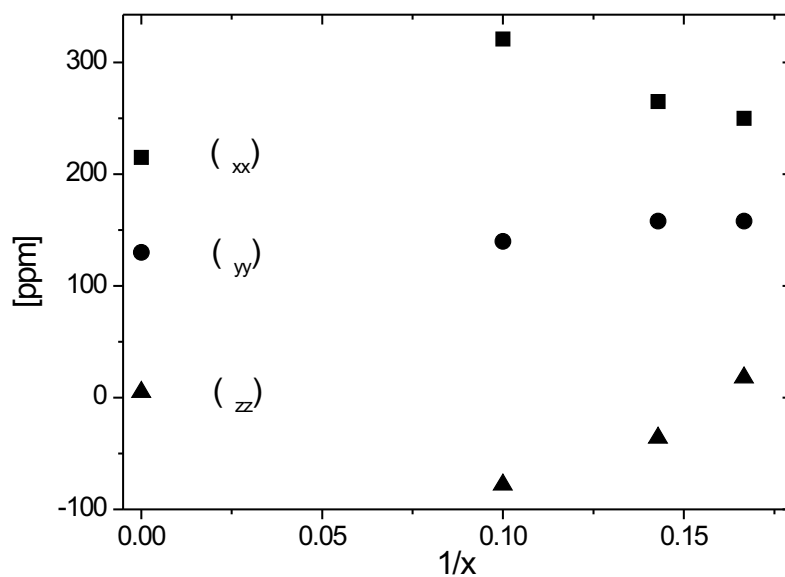


Figure 3.2: ^{13}C NMR CSA tensor components δ_{ii} for the room temperature spectra of pristine SWNT ($1/x = 0$) and LiC_x intercalated compounds with $x = 10, 7, 6$ ($1/x = 0.1, 0.14, 0.17$), respectively.

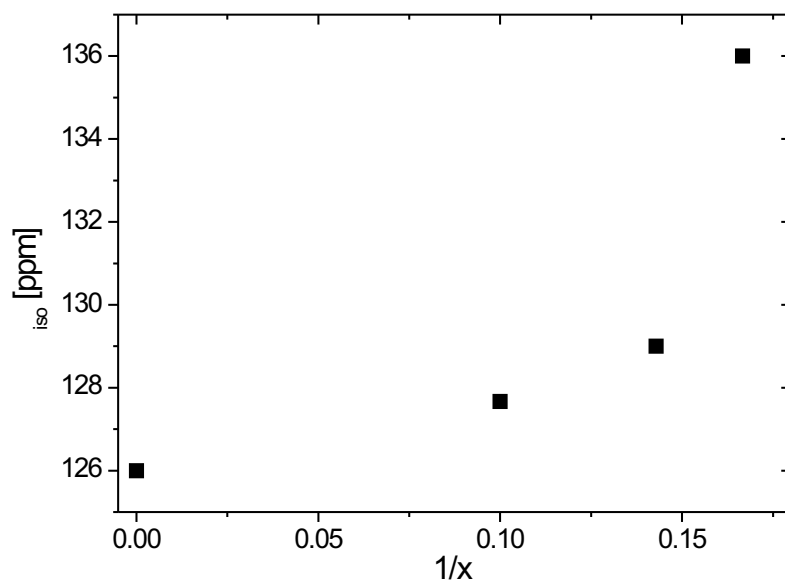


Figure 3.3: ^{13}C NMR isotropic shift positions at room temperature for pristine SWNT ($1/x = 0$) and LiC_x intercalated compounds with $x = 10, 7, 6$ ($1/x = 0.1, 0.14, 0.17$), respectively. The isotropic shifts are the sum of the chemical σ and the Knight shift K .

the corresponding MAS spectra at the bottom of Fig. 3.1 confirm these facts. By performing a Herzfeld-Berger analysis [25], a continuous reduction of the anisotropy of about 200 ppm from LiC_{10} to LiC_6 is observed (Fig. 3.2).

As described by Eq. (2.14), for higher stages of intercalated graphite, the anisotropy is reduced to about 1800 ppm/electron upon charge transfer to the carbon host.

Even though GIC and SWNT systems are not necessarily identical, they should present similarities. Following the spectral line shapes from LiC_{10} to LiC_6 and transferring the scenario of anisotropy reduction in GIC to Li intercalated SWNT, a reduction of the anisotropy up to ~ 450 ppm is expected. A simple comparison with the lower observed value of 200 ppm in Li-SWNT suggests an incomplete electron charge transfer at higher intercalation levels.

With increasing intercalation level, the isotropic line positions δ_{iso} are monotonically paramagnetically shifted from 126 ppm for pristine SWNT [34, 195] up to 136 ppm for LiC_6 (Fig. 3.3).

These observations indicate important modifications of the electronic properties and suggest that all samples exhibit a metallic ground state which can be monitored simply by the amount of intercalated Li [216]. The observed shift δ can be separated into two additive parts, the chemical shift σ and the Knight shift \mathbf{K} with

$$\delta = \sigma + \mathbf{K}. \quad (3.1)$$

As shown in Chap. (2.1), σ and \mathbf{K} are second rank tensors consisting of an isotropic and an anisotropic part. In the following, the evolution of the isotropic part under Li intercalation is discussed.

According to Eq. (2.9) and (2.10), the isotropic part of the Knight shift is paramagnetic and proportional to the conduction electron probability at the nucleus $\langle |\psi(0)|^2 \rangle$ and the density of states (DOS) at the Fermi level $n(\varepsilon_F)$:

$$K_{iso} = \frac{16\pi}{3} \langle |\psi(0)|^2 \rangle \mu_B^2 n(\varepsilon_F). \quad (3.2)$$

Since the isotropic Knight shift is proportional to $n(\varepsilon_F)$, the measurements in Fig. 3.1 suggest an increasing of the DOS with increasing Li concentration. However, it is not trivial to estimate $n(\varepsilon_F)$ directly from the isotropic line position because of the isotropic chemical shift contribution which is completely unknown in charged SWNT. The isotropic shift values given in Tab. 3.1 represent the sum of chemical shift and Knight shift $\delta = \sigma + K$.

	LiC ₆	LiC ₇	LiC ₁₀
δ_{iso} [ppm]	136	129	127.7
δ_{zz} [ppm]	18	-36	-78

Table 3.1: Experimental values for δ_{iso} and δ_{zz} for LiC₆, LiC₇ and LiC₁₀. The shifts are always the sum of chemical shift and Knight shift $\delta = \sigma + K$.

Assuming a weak dependence of the chemical shift on the Li intercalation, the monotonic increase of δ_{iso} suggests a strong modification and increase of the density of states at the Fermi level $n(\varepsilon_F)$ with increasing Li intercalation level. However, in order to confirm this assumption and obtaining an estimate of $n(\varepsilon_F)$, temperature dependent ¹³C NMR spin-lattice relaxation measurements were performed.

3.2.2 $1/T_1$ Relaxation Rate

Fig. 3.4 compares the room temperature magnetization recovery for pristine and Li intercalated SWNT (LiC₆). For all Li intercalated samples, 96% of the ¹³C NMR signal exhibits one T_1 component which can be fitted by an exponential magnetization recovery curve after saturation. The corresponding T_1^{-1} relaxation rates are plotted in Fig. 3.5.

In pristine SWNT, the magnetization recovery typically consists of two components with a ratio of 60:40 and room temperature relaxation times of 90 s and 5 s, respectively. In general, these two relaxation components are attributed to relaxation of semiconducting (60%) and metallic (40%) carbon nanotubes [34, 193, 194]. Since in the intercalated SWNT only the fast relaxing component is observable it can be assumed, that due to intercalation the band structure of the semiconducting SWNT is modified and these nanotubes behave like metallic ones with increased DOS.

Above a temperature of 50 K a linear regime of the spin-lattice relaxation rate versus temperature is seen in Fig. 3.4. The slope depends on the Li intercalation level. Below 50 K, the relaxation rate seems to increase with decreasing temperature.

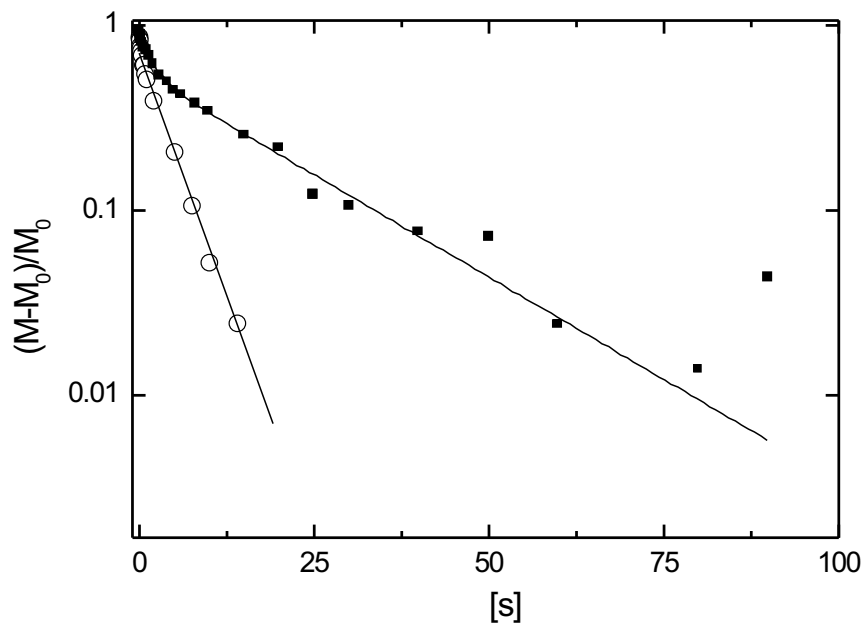


Figure 3.4: ^{13}C NMR magnetization recovery at room temperature for LiC_6 : \circ and pristine SWNT: \blacksquare [34].

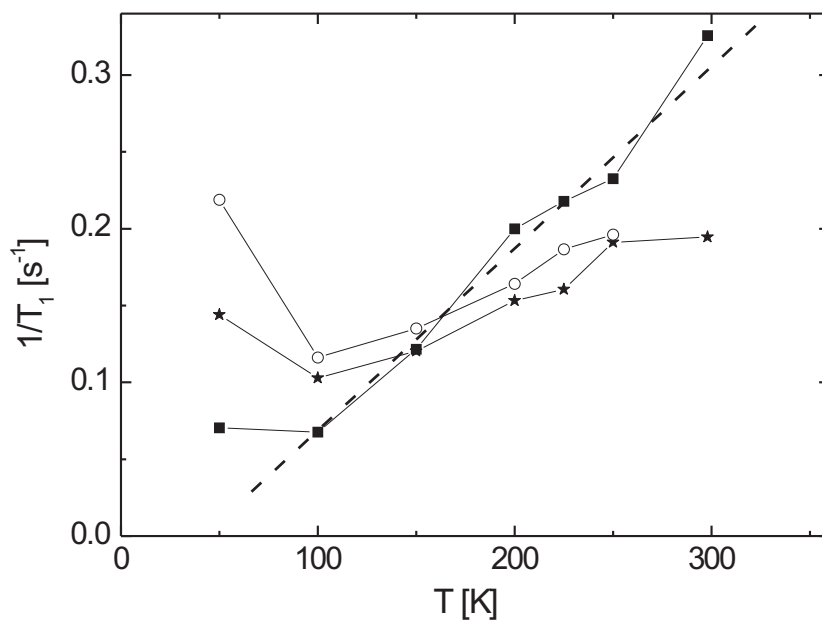


Figure 3.5: Temperature dependent ^{13}C NMR spin lattice relaxation rates for LiC_{10} : \star , LiC_7 : \circ and LiC_7 : \blacksquare . The dashed line is a guideline for the eyes.

Low Temperature Increase of $1/T_1$

In the following, several explanations for the increase of $1/T_1$ with decreasing temperature below 50 K are discussed.

- One possible origin for the low temperature increase of $1/T_1$ could arise from couplings between ^{13}C nuclear spins and unpaired electron spins which are fixed in space. Such a kind of coupling is different from the scalar spin-spin coupling discussed in Chap. (2.2.2), where rapid relative motions of nuclear and electron spins were considered.

Fixed electron spins could originate from either fixed ferro- or paramagnetic impurities or unpaired electrons due to local defects in the SWNT. Generally, SWNT are known to possess defects like Stone-Wales defects, single vacancies, point defects and dangling bonds around vacancies, which are all known to influence the physical and chemical properties of SWNT to some extent [217–219]. The present samples were prepared using the non-ferromagnetic catalyst Pt and Rh. Platinum is a paramagnetic metal, whereas bulk Rhodium shows diamagnetic properties. However, below 93 K small clusters of Rh (up to ~ 80 atoms, size of several nm) show superparamagnetism. In general, below a certain temperature in strong external magnetic fields, superparamagnetic clusters possess a giant magnetic moment. Above that temperature, thermal fluctuations prevent the magnetic moment from fully aligning with the external field and the clusters show paramagnetic behavior [220–222].

Paramagnetic spin-lattice relaxation is highly effective even for small concentrations of unpaired electrons, since the relaxation among neighboring nuclear spins is dispensed through spin diffusion to other nuclei (mutual spin flips between neighboring spins). The corresponding nuclear spin-lattice relaxation rate is given by [20]

$$\begin{aligned} \frac{1}{T_1} &= \frac{C}{r^6} \quad \text{with} \\ C &= \frac{2}{5} (\gamma_S \gamma_I \hbar)^2 S(S+1) \frac{\tau_S}{1 + \omega_0^2 \tau_S^2}, \end{aligned} \tag{3.3}$$

where r is the distance of the observed nucleus to the unpaired electron and γ_S and γ_I are the gyromagnetic ratios of the electron and nucleus, respectively. S is the electron spin quantum number and τ_S the electron spin-lattice relaxation time.

This kind of ^{13}C NMR T_1 relaxation behavior in SWNT was observed by Goze et al. in pristine SWNT [195]. The authors reported an increase of $1/T_1$ below 50 K, corresponding to the high temperature part of Eq. (3.3). However in their investigations, the dominant source of relaxation most likely originated from ferromagnetic Ni/Y impurities, present as catalytic particles in the sample.

- Another proposed origin for a low temperature increase of ^{13}C NMR $1/T_1$ with decreasing temperature is the opening of a band gap in the SWNT electronic band structure at low temperatures [223].

Generally, in the presence of a small band gap, the highest occupied band just below the gap and the lowest occupied band just above the gap are equally occupied at higher temperatures. With decreasing temperature, the upper band is depleted, which leaves unpaired electrons in this band. These unpaired electrons effectively relax the spin-system causing an increase of $1/T_1$. At very low temperatures, the relaxation rate decreases again, since the upper band becomes completely unoccupied and the number of available unpaired electrons in the upper band is exhausted.

The reason for the opening of a gap in metallic SWNT is manifold. Theoretical calculations have shown, that deformations of carbon nanotubes, close packing of nanotubes in a bundle and even the adsorption of transition metal atoms on a metallic SWNT can give rise for the opening of a band gap [183, 224, 225]. Since the catalyst impurities in the present intercalated samples are the transition metals Rhodium and Platinum, the presence of a band gap is very likely [225]. Also due to the close packed triangular lattice of the nanotube system, the presence of a pseudo gap of 0.1 eV width at the Fermi level is imaginable as shown by ab-initio calculations [224]. However, it is unknown how effectively ^{13}C NMR spin-lattice relaxation will be affected by a band gap in the investigated temperature range.

- A third possibility for an increase of ^{13}C NMR $1/T_1$ with decreasing temperature could originate from the formation of a Tomonaga-Luttinger liquid (TLL) at low temperatures. TLL-states describe one-dimensional correlated electron states which are expected in metallic SWNT at low temperatures (see Chap. 1.2).

It is theoretically predicted, that electron-electron Coulomb interactions cause a deviation of the linear $1/T_1$ behavior from the classical Korringa relaxation law. In three dimensional metals, a Korringa type $1/(T_1T)$ is known to be independent of temperature. However, in nearly one dimensional systems like

SWNT, the TLL state is expected to cause an increase of $1/(T_1T)$ (e.g. of $1/T_1$) by a power law with decreasing temperature [190].

However, this should be only the case for very low alkali intercalation levels. For potassium intercalation in SWNT bundles, Pichler et. al [226] has shown, that already above an intercalation level of KC_{150} , a transition from TLL states to a Fermi liquid state occurs. Since in the present Li intercalated samples, the Li content is at least more than a factor 10 above this stoichiometry, the existence of a TLL state seems to be unlikely.

Correspondingly it can be stated, that the source for the increase of ^{13}C NMR $1/T_1$ with decreasing temperature has to be either attributed to couplings between ^{13}C nuclear spins and unpaired electron spins (paramagnetic relaxation) or the opening of a band gap at low temperatures. A clear statement is not possible using the present data and further detailed low temperature ^{13}C NMR experiments with according data-fits have to be performed.

Linear Increase of T_1^{-1} Above 50 K

The linear increase of the relaxation rate above 50 K is typical for a metallic Fermi liquid system. In metals the major relaxation mechanism is caused by hyperfine coupling of conduction electron spins with the observed nuclei. Additionally, this coupling causes a Knight shift. Both the isotropic and the anisotropic hyperfine coupling play an important role for the electron-nuclear interaction. As discussed in Chap. (2.1.4), the isotropic Fermi contact interaction is dominating, if the electron wave function has appreciable s character and therefore a non vanishing probability density at the carbon nucleus. For electrons with non- s character (e.g. p_z or sp^2 orbital character), the distant dipole-dipole hyperfine coupling is more important.

From graphene and particularly C_{60} , a predominant p_z and sp^2 orbital character of the ^{13}C electrons is known, causing an anisotropic Knight shift K_{aniso} [4, 33]. Therefore it is obvious to fit the increase of $1/T_1$ in Fig. 3.5 by using the Korringa relation (see Chap. 2.2.1), which describes a linear temperature dependence of the spin-lattice relaxation rate. Considering an isotropic dipolar hyperfine coupling, the corresponding spin-lattice relaxation rate is given by Eq. (2.46)

$$\frac{1}{T_1T} = \frac{2\pi k_B}{\hbar} S_K A_{dip}^2 n(\varepsilon_F)^2 \quad \text{with}$$

$$A_{dip} = \frac{2}{5} \frac{\mu_0}{4\pi} \gamma_n \gamma_e \hbar^2 \left\langle \frac{1}{r^3} \right\rangle.$$

This formula includes the Korringa enhancement factor S_K defined in Eq. (2.42). However, up to the present no experimental or theoretical data are available which would enable to calculate the required dipolar hyperfine coupling constant A_{dip} of intercalated SWNT. Thus, due to the similarity of the curved carbon structure of intercalated C_{60} and SWNT, it is reasonable to use a dipolar hyperfine coupling constant of A_3C_{60} in order to obtain a rough estimate of the density of states at the Fermi level in SWNT [193]. By using ab initio calculations, Antropov et al. [33] showed, that in the case of potassium intercalated graphite K_3C_{60} , $\langle (a_0/r)^3 \rangle = 3.71$ with a_0 being the Bohr radius. This yields a dipolar hyperfine coupling of $A_{dip} = 8.2 \cdot 10^{-7}$ eV.

In pristine SWNT, the applicability of applying the dipolar hyperfine coupling of K_3C_{60} was demonstrated. ^{13}C NMR spin-lattice relaxation measurements proved that the resulting $n(\varepsilon_F) = 0.022$ states/(eV·spin·atom) is remarkably close to the theoretical value of $n(\varepsilon_F) = 0.015$ states/(eV·spin·atom) calculated for a (10,10) armchair SWNT with a diameter of 14 Å [193, 210].

The Korringa enhancement factor S_K for the three Li intercalated samples can be extracted from Eq. (2.42)

$$T_1 T K_{iso}^2 (1 + \frac{1}{2}\varepsilon) C_0 S_K = 1 \quad \text{with} \quad (3.4)$$

$$\varepsilon = \frac{(K_{zz} - K_{iso})^2}{K_{iso}^2}.$$

However, this requires the knowledge of K_{iso} and K_{zz} , which cannot be directly extracted from Fig. 3.1. As already mentioned, the shift values in Tab. 3.1 contain an unknown contribution from the chemical shift due to orbital currents.

In the following, a rough estimate for the chemical shifts, the Knight shifts and the Korringa enhancement factor S_K is developed. It is assumed, that the main principal axis of the chemical and Knight shift tensors are identical, which is not necessarily the case. Finally, by fitting the linear part of the ^{13}C NMR spin lattice relaxation rate in Fig. 3.5, the evolution of $n(\varepsilon_F)$ with the Li concentration is calculated.

To simplify matters, first, shift tensors of pristine SWNT are examined followed by tensors of intercalated SWNT.

- In **pristine SWNT**, K_{iso} was estimated to be less than 10 ppm. [34, 196]. Since δ_{iso} in pristine SWNT typically amounts to 126 ppm, the corresponding isotropic chemical shift should be expected to follow $116 \text{ ppm} \leq \sigma_{iso} \leq 126 \text{ ppm}$.

$\sigma_{zz} = \delta_{zz} - K_{zz}$ can be calculated using Eq. (3.4) to $\sigma_{zz} = -35$ ppm for pristine SWNT. This corresponds to a Korringa enhancement factor $S_K \sim 2.2$ and the theoretically expected DOS of $n(\varepsilon_F) = 0.015$ states/(eV·spin·atom). The Korringa enhancement factor is comparable to $S_K \sim 2.5$ as observed in A_3C_{60} [37].

Finally, by using Eq. (2.44), the isotropic hyperfine coupling constant can be calculated to $a_{iso} = 2\pi \cdot 2.8 \times 10^7$ s⁻¹.

- For the **intercalated SWNT**, this analysis is much more difficult, since there exist no isotropic chemical shift calculations for this kind of material. However, by comparison with the isotropic chemical shift behavior observed in C_{60} upon potassium intercalation (experimental data on K_3C_{60}), the isotropic chemical shift σ_{iso} can be estimated to be around $\sim 120 - 130$ ppm [37].

With increasing intercalation level, $n(\varepsilon_F)$ is expected to increase due to the rising availability of electrons transferred from the Li nuclei. Thereby, in order to keep S_K in a reasonable range ($1 \leq S_K \leq 4$), δ_{zz} has to decrease with increasing intercalation level. The corresponding results are summarized in Tab. 3.2.

	LiC ₆	LiC ₇	LiC ₁₀	Pristine
σ_{iso} [ppm]	120-130	116-129	116-128	116-126
σ_{zz} [ppm]	-85	-85	-40	-30
K_{iso} [ppm]	0 – 16	0 – 13	0 – 12	0 – 10
K_{zz} [ppm]	103	49	-38	35
S_K []	1.2	2.2	2.6	2.2
a_{iso} [$2\pi \cdot$ s ⁻¹]	5.4×10^7	4.8×10^7	3.8×10^7	2.8×10^7
$n(\varepsilon_F)$ [states/(eV·spin·atom)]	0.042	0.021	0.020	0.015

Table 3.2: Analysis of the CSA tensors for Li intercalated SWNT LiC_x and pristine SWNT: Calculations of chemical shift σ and Knight shift \mathbf{K} tensor values, Korringa enhancement factors S_K , isotropic hyperfine coupling constants a_{iso} and density of states at the Fermi level $n(\varepsilon_F)$. The main principal axis of the chemical and Knight shift tensors are assumed to be identical.

In agreement with the lineshape modification, the highest $n(\varepsilon_F)$ corresponds to the highest Li intercalation. However, assuming a complete electron charge transfer, the increase in $n(\varepsilon_F)$ from LiC_{10} to LiC_7 is expected to be stronger than is observed. An explanation for the similarity of the DOS in LiC_{10} and LiC_7 could arise from a severe limitation in charge transfer in LiC_7 .

Using first principle calculations, Jo et. al [131] determined the dependence of $n(\varepsilon_F)$ on potassium intercalation stoichiometry. Comparable to the present results, the authors found a rapidly increasing DOS at low intercalation levels, saturating at a stoichiometry of KC_{20} . This behavior was explained by a partial (not complete) charge transfer occurring in between the potassium and the SWNT.

Nevertheless, the density of states at the Fermi level increases monotonically with increasing charge concentration and no evidence for features originating from van Hove singularities (spikes) in the DOS is observable. In general, SWNT bundles are made of tubes of different diameters and chiralities. Correspondingly the van Hove singularities in the DOS are expected to be broadened due to a distribution of diameter and chirality [191,227]. Additionally, upon intercalation the SWNT band structure is modified and various van Hove singularities tend to coalesce with increasing intercalation density [142]. The van Hove singularities are smoothed out and not resolvable any more. This is in agreement with in-situ conduction measurements during intercalation on the present Li intercalated samples [161].

3.3 ^7Li NMR

3.3.1 Spectra

Fig. 3.6 shows the static ^7Li NMR spectrum of LiC_{10} at a temperature of 50 K. No Li^0 metal line was observed which is expected to be paramagnetically shifted up to $\delta_{\text{metal}} = 262$ ppm.

The lineshape in Fig. 3.6 can be fitted using two quadrupolar inhomogeneously broadened lines suggesting two inequivalent sites for the Li with different environments and hybridized electronic states. The motivation for using a fit combination of two quadrupolar lines arises from the spin-lattice (T_1) relaxation behavior of the spectrum, which will be discussed in detail in the next section.

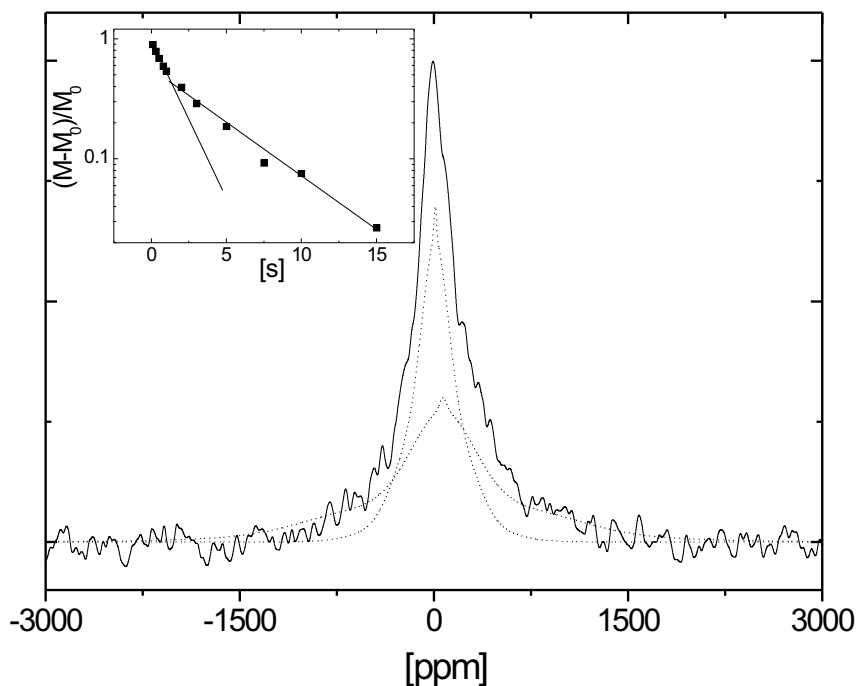


Figure 3.6: Static ^7Li NMR spectrum of LiC_{10} at a temperature of 50 K and a magnetic field of 4.2 T (Larmor frequency 70.2 MHz). The dotted lines are fits using two quadrupolar broadened lines. Inset: magnetization recovery after saturation for LiC_{10} at a temperature of 50 K showing two α and β magnetization recovery components.

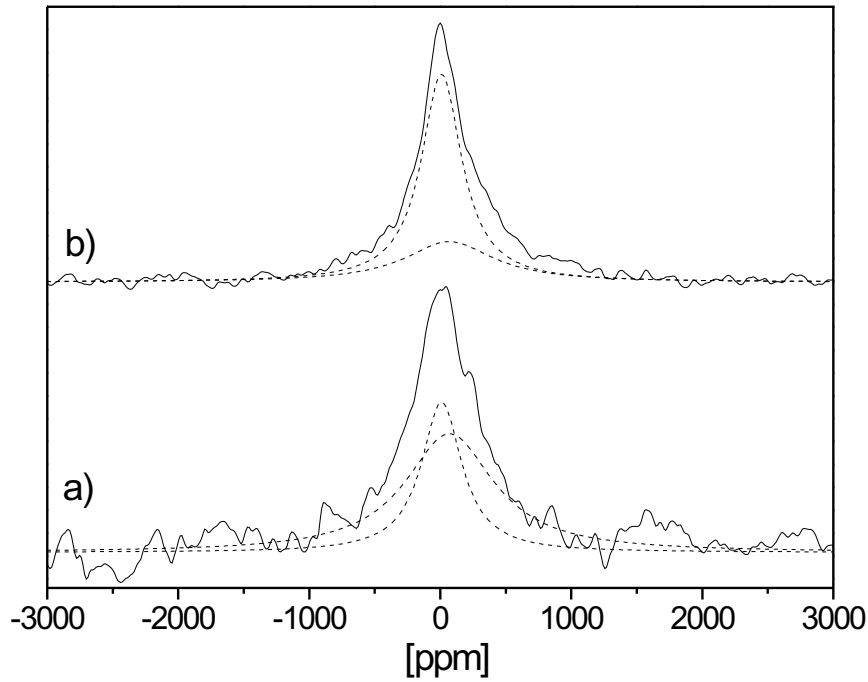


Figure 3.7: ${}^7\text{Li}$ NMR spectra in LiC_{10} at a Larmor frequency of 70.2 MHz and a temperature of 50 K extracted from magnetization recovery experiments: a) partially recovered spectrum at a short delay of $\tau = 0.8$ s and b) fully relaxed spectrum at a long delay of $\tau = 22$ s. The ratios in a) [α : 37% β : 63%] and in b) [α : 70% β : 30%] are obtained from a deconvolution (dashed lines) with one sharp- α and one broad- β Lorentzian line as described in the text.

In all samples at all temperatures, the recovery of the magnetization follows a biexponential curve (Fig. 3.6, inset). This corresponds to two sources of spin-lattice relaxation rates suggesting two inequivalent Li sites. In the following, these two sites are labeled α and β with $T_1^\alpha > T_1^\beta$.

In order to estimate the corresponding ${}^7\text{Li}$ NMR resonances, the line shift and linewidth during relaxation measurements were investigated. Fig. 3.7 shows the spectra for LiC_{10} at 50 K during the magnetization recovery experiment at two different delays (a: $\tau = 0.8$ s, b: $\tau = 22$ s).

For the sake of simplicity, Lorentzian lines instead of quadrupolar broadened lines are used in order to fit the partially recovered spectrum (Fig. 3.7a) and fully relaxed one (Fig. 3.7b). The best fits are performed assuming a sharp- α (FWHM ~ 29 kHz) and a broad- β (FWHM ~ 64 kHz) Lorentzian line shifted to $\delta_\alpha \sim 10$ ppm and $\delta_\beta \sim 70$ ppm, respectively. The intensities were determined according to their relaxation behaviors at 50 K with spin-lattice relaxation times $T_1^\alpha \sim 3.8$ s and $T_1^\beta \sim 0.54$ s and their ratios extracted from the magnetization recovery curve.

The two Lorentzian lineshapes reflect well the quadrupolar broadened lines in Fig. 3.6 – the corresponding quadrupolar lineshape parameters are $\Delta\omega_Q^{(\alpha)} \sim 2\pi \cdot 45$ kHz and $\Delta\omega_Q^{(\beta)} \sim 2\pi \cdot 140$ kHz with Gaussian broadenings of the central transitions with $\delta\omega^{(\alpha)} \sim 2\pi \cdot 8$ kHz and $\delta\omega^{(\beta)} \sim 2\pi \cdot 19$ kHz. The line broadenings indicate an inhomogeneous linewidth due to a large distribution of quadrupole frequencies. The significant difference in quadrupolar interaction of the α and β line suggests profound difference in their environment.

These results confirm the presence of two different Li^+ cations, one $\text{Li}^{(\alpha)+}$ with an ionicity close to +1 and a $\text{Li}^{(\beta)+}$ cation with an ionicity < 1 , *i.e.* $\beta < \alpha \approx 1$.

The paramagnetic shift of the β -line has to be attributed to either a Knight or a chemical shift. However, the β -line shift is already about 30% of the pure metal Knight shift. The maximum range of Li chemical shifts is known to be in the order of only (+5,-10 ppm) which suggests that the chemical shift is small [90].

Thus, the large remaining shift is dominantly a Knight shift, which is typically for a limited charged transfer of the 2s electron of Li stored in a dense form in nanoporosities [228].

The quadrupolar broadened ^7Li NMR β -line as observed in Fig. 3.6 suggests the presence of strong interactions between C and $\text{Li}^{(\beta)+}$ nuclei comparable to observations in graphite intercalation compounds [90, 229].

The origin for the two inequivalent Li-sites is unknown, but it is certainly related to the complex structure of bundles of carbon nanotubes which presents different adsorption sites giving inequivalent environments and hybridized electronic states for the Li [131, 142, 143]. According to recent calculations, the outside-Li adsorption is energetically more favorable than the Li inside the SWNT [143]. In particular, the curvature of the graphene layer in SWNT and the presence of highly reactive dangling bonds localized on defects tend to enhance the adsorption capabilities [15, 216].

Solid state electrochemistry revealed that electrochemical Li intercalation in SWNT is only partially reversible. The authors claim that upon de-intercalation some Li remains trapped in the SWNT host [162]. This would confirm the strong interactions between Li and C in the present samples. It should be emphasized that this effect, which limits the charge transfer for higher levels of intercalation could explain the similarities in ^{13}C NMR relaxation between LiC_{10} and LiC_7 despite the different stoichiometries.

Remarkable is the similarity of the present ${}^7\text{Li}$ spectra with spectra obtained from Li graphite intercalation compounds (Li-GIC) [90]. Depending on the stoichiometry, two coexisting lines located around +17 ppm and +45 ppm are observed for stage II and stage III Li-GIC. At higher stoichiometries of LiC_6 (stage I), only one single quadrupolar shaped line at 45 ppm is observable. The line positions and line shapes suggest that the electronic states of the $\text{Li}^{(\alpha)+}$ and $\text{Li}^{(\beta)+}$ nuclei are comparable to the ones in Li-GIC.

3.3.2 $1/T_1$ Relaxation Rate

${}^7\text{Li}$ NMR spin-lattice relaxation measurements were performed by saturation-recovery experiments in the temperature range from 50 K to 450 K. Due to the limited stability of the intercalated samples, it was not possible to measure above this temperature. The work on the relaxation experiments was mainly focused on the sample LiC_{10} , since T_1 in the other samples showed very long relaxation times and bad signal to noise ratios. Therefore, in case of LiC_6 and LiC_7 , spin-lattice relaxation measurements were limited to only a few temperatures.

For all samples at all investigated temperatures, the magnetization recovery followed a biexponential curve confirming the two $\text{Li}^{(\alpha)+}$ and $\text{Li}^{(\beta)+}$ inequivalent sites. From fits of the magnetization recovery, the ratios between α and β sites can be estimated. The results are summarized in Tab. 3.3. Obviously, at low intercalation levels the first intercalated Li are of type $\text{Li}^{(\alpha)+}$. While increasing the Li concentration, a second type $\text{Li}^{(\beta)+}$ is adsorbed by the SWNT host.

The temperature dependence of the α - and β - $1/T_1$ relaxation rate is presented in Fig. 3.8. For later discussions it is important to note, that relaxation measurements on LiC_7 yield a similar relaxation behavior in temperature.

	α -site	β -site
LiC_{10}	70%	30%
LiC_7	55%	45%
LiC_6	50%	50%

Table 3.3: Ratios of α and β sites in LiC_x ($x=6, 7, 10$) at room temperature. The ratios are extracted from magnetization recovery experiments.

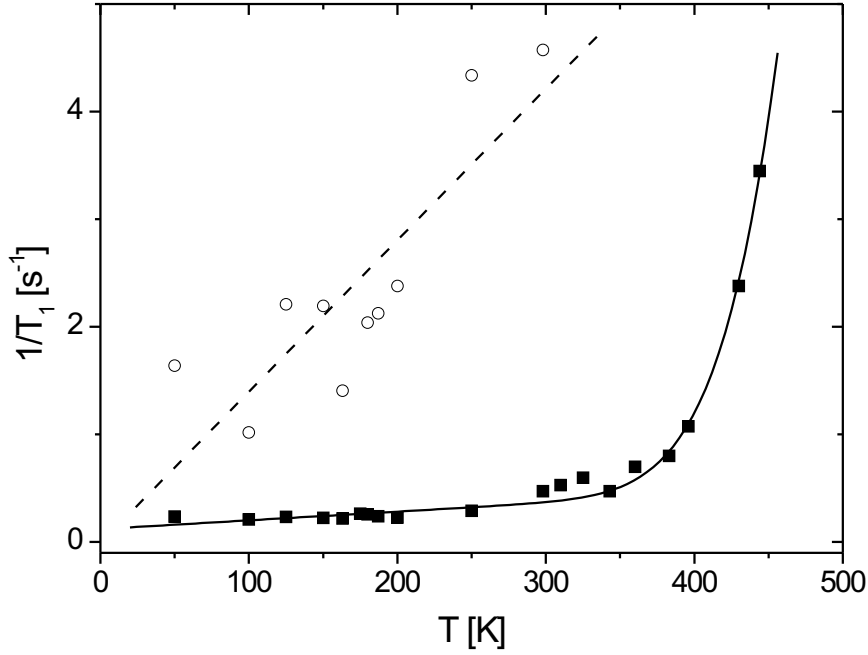


Figure 3.8: Temperature dependence of the ${}^7\text{Li}$ NMR spin-lattice relaxation rate $1/T_1$ of LiC_{10} for the α -line (■) and the β -line (○). The solid line is a fit assuming a combination of a linear Korringa relaxation process and a BPP-type quadrupolar relaxation mechanism. The dashed line is a fit assuming a Korringa relaxation process.

α -Line T_1 -Relaxation

The α -line spin-lattice relaxation rate follows a linear increase with increasing temperature below ~ 400 K and a rapid exponential increase above. According to the Korringa relation Eq. 2.44, the source of the linear relaxation regime can be interpreted as a hyperfine coupling of the Li nuclei to conduction electrons of the carbon nanotube host at low temperatures.

By applying a linear fit to the low temperature run of $1/T_1$ in Fig. 3.8, a slope of $1/T_1^{(\alpha)}T \sim 0.00081 \text{ s}^{-1}\text{K}^{-1}$ is obtained. This value is below the result of $1/T_1T = 0.0016 \text{ s}^{-1}\text{K}^{-1}$ for a first stage Li-graphite intercalation compound LiC_6 [91].

The exponential increase and deviation from Korringa's law of $1/T_1$ above a temperature of 400 K is typical for a thermally activated BPP-type diffusion or motion modulated quadrupolar interaction. A thermally activated diffusion path of $\text{Li}^{(\alpha)+}$ is expected along the channels of the carbon nanotube bundles.

A quadrupolar relaxation of the ${}^7\text{Li}$ nuclei promoted by fluctuations of local electric field gradients can be readily expressed according to Chap. (2.2.3) as

$$\frac{1}{T_1} = \frac{2}{25} \Delta\omega_Q^2 \cdot [J^{(1)}(\omega_0) + J^{(2)}(\omega_0)]. \quad (3.5)$$

where the spectral densities $J^{(i)}(\omega_0)$ include a thermally activated process with

$$J^{(1)}(\omega_0) = \frac{\tau_c}{1 + \omega_0^2 \tau_c^2}, \quad J^{(2)}(\omega_0) = \frac{4\tau_c}{1 + 4\omega_0^2 \tau_c^2}. \quad (3.6)$$

Since the high-temperature tail of the BPP-peak in Fig. 3.8 is missing, the infinite temperature correlation time τ_0 remains indefinite. Nevertheless, in order to fit the data a typical value of $\tau_0 \sim 10^{-12}$ s is assumed. With an Arrhenius type thermally activated correlation time given by Eq. (2.56)

$$\tau_c(T) = \tau_0 \exp\left(\frac{\Delta E}{k_B T}\right), \quad (3.7)$$

the activation energy for the Li relaxation process can be determined to $\Delta E \sim 0.4$ eV. Additionally, a constant background relaxation rate $1/T_{10}^\alpha \sim 0.12$ s $^{-1}$ has to be assumed. The quadrupolar coupling constant can be estimated to $\Delta\omega_Q^{(\alpha)} \sim 2\pi \cdot 40$ kHz. It confirms the quadrupolar α -line fit parameter $\Delta\omega_Q^{(\alpha)} \sim 2\pi \cdot 45$ kHz in Fig. 3.6.

β -Line T_1 -Relaxation

In the investigated temperature range, the β -line spin-lattice relaxation rate in in Fig. 3.8 follows a linear Korringa relaxation process. By applying a linear fit, a slope of $1/T_1^{(\beta)} T \sim 0.0135$ s $^{-1}\text{K}^{-1}$ is obtained. This value is in between $1/T_1 T = 0.0016$ s $^{-1}\text{K}^{-1}$ for a first stage Li-graphite intercalation compound LiC_6 [91] and $1/T_1 T = 0.023$ s $^{-1}\text{K}^{-1}$ for pure Li^0 metal [230].

These results confirm the interpretation of the substantial paramagnetic β -line Knight shift in Fig. 3.6: a strong hyperfine coupling between $\text{Li}^{(\beta)}$ nuclei and the nearly free electron π system of the SWNT, which participates in the density of states $n(\varepsilon_F)$ of the conduction electronic states. The strong Li-C hyperfine coupling suggests a $\text{Li}(2s)$ - $\text{C}(2p)$ hybridization which explains well the charge transfer limitations observed with ${}^{13}\text{C}$ NMR measurements in Chap. (3.2.2).

3.4 ^1H NMR

3.4.1 Spectra

In order to understand the role of the cointercalated solvent molecules THF, temperature dependent ^1H NMR measurements were performed. The ^1H NMR spectra for LiC_7 are shown in Fig. 3.9. At temperatures below 300 K, the spectrum consists of one broad line with a FWHM of about 72 ppm ($\delta\nu_B \sim 13$ kHz). Above 300 K, a second narrow line is visible (FWHM < 17 ppm $\delta\nu_N < 3$ kHz) and the spectra can be fitted using 2 Lorentzian lines, a broad and a narrow one. This suggests the presence of two types of inequivalent THF solvent molecules with different chemical environments and dynamical behavior.

Assuming a Gaussian lineshape, the FWHM for a THF molecule in a rigid lattice can be calculated by using Eq. 2.38 to $\delta\nu \sim 46$ kHz. This value is comparable with the linewidth obtained in Li-GIC ($\text{LiC}_n(\text{THF})_m$) at low temperatures (FWHM ~ 60 kHz). At elevated temperatures, a linewidth narrowing to ~ 14.9 kHz is observable in Li-GIC

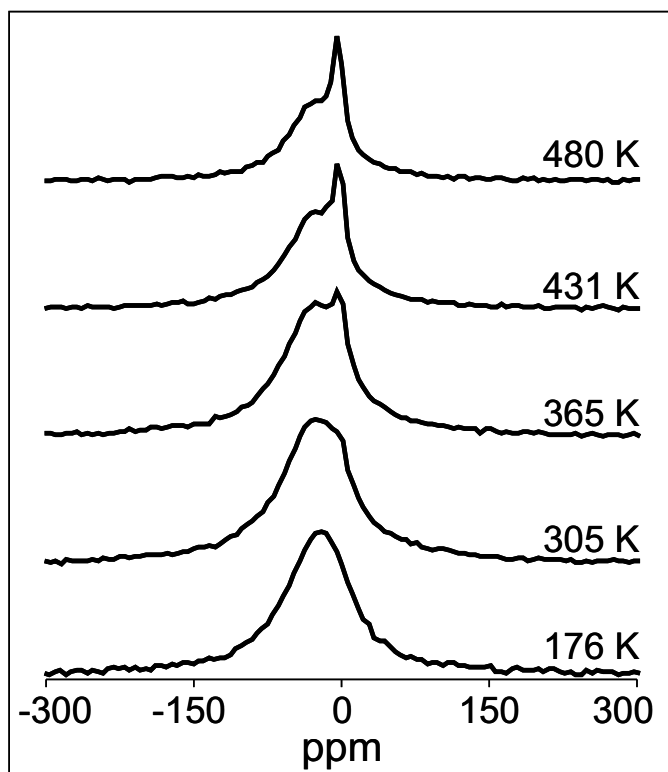


Figure 3.9: Static ^1H NMR spectra of LiC_7 at different temperatures between 176 K and 480 K and a magnetic field of 4.2 T (180.5 MHz). The spectra show one broad line and the evolution of one thermally activated narrow line.

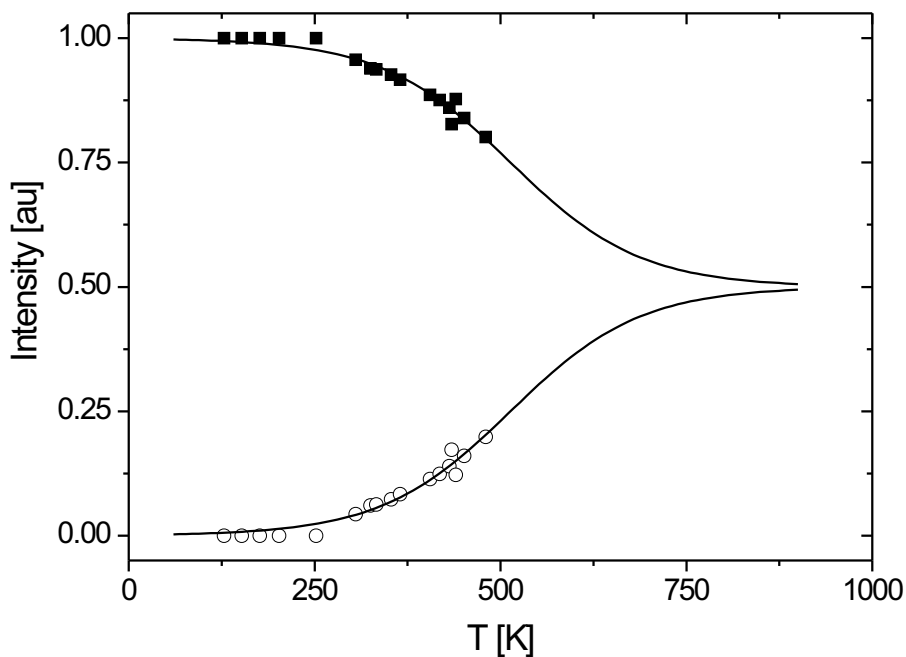


Figure 3.10: Relative intensities of the broad (■) and the narrow ^1H NMR line (○) extracted from fits with two Lorentzian lines. The solid lines represent fits using sigmoidal curves. For more details refer to the text.

which is characteristic of an anisotropic hindered motion of THF molecules (rotation around the dipolar axis) [18]. This is comparable with the observed $\delta\nu_B \sim 13$ kHz reported here and suggests a rotation of the THF molecules around their dipolar axis as the origin of the broad proton line.

On the other hand, isotropic rotation of the THF molecules is understood as the source of the linewidth of the narrow line ($\delta\nu_N \sim 3$ kHz).

At room temperature, the broad line is located around $\delta = -30$ ppm whereas the second narrow line is shifted to around $\delta = -3$ ppm. The observed negative shifts are unusual and remarkably high. ^1H NMR chemical shifts usually range from 0 to +12 ppm. The phenomenon of negative shifts can be either explained by a negative paramagnetic Knight shift or an extremely large diamagnetic shielding of the carbon nanotubes and will be addressed later.

Following the line positions in the temperature range from 300 K to 480 K, the broad line is slightly paramagnetically and the narrow line slightly diamagnetically shifted. This is a signature of an exchange process [20].

Another signature is the growing intensity of the narrow line with increasing temperature at the expense of the broad line as Fig. 3.10 shows. For the case of an exchange process, the temperature dependence of the intensities can be described by a sigmoidal curve

$$I(T) = \frac{I_0 - I_\infty}{1 + \exp\left(\frac{T - T_{\frac{1}{2}}}{\Gamma}\right)} + I_\infty. \quad (3.8)$$

I_0 and I_∞ are the intensities at 0 K and infinite temperature, respectively and Γ is a measure for the bending of the curve. At $T = T_{\frac{1}{2}}$ the intensity of the curve is given by $I_{\frac{1}{2}} = (I_0 + I_\infty)/2$.

The solid lines in Fig. 3.10 represent fits using sigmoidal curves with $I_0 = 0$ (narrow ^1H NMR line, \circ), $I_0 = 1$ (broad ^1H NMR line, \blacksquare) and $I_\infty = 0.5$ for both lines. The temperature $T_{\frac{1}{2}}$ is found to $T_{\frac{1}{2}} = 514$ K.

For an exchange process, the correlation time $\tau_{\frac{1}{2}}$ at the temperature $T = T_{\frac{1}{2}}$ is described by

$$\tau_{\frac{1}{2}} \delta\omega_0 = 1 \quad (3.9)$$

with $\delta\omega_0$ being the rigid lattice linewidth. By assuming an Arrhenius behavior of the correlation time

$$\tau_{\frac{1}{2}} = \tau_0 \exp\left(\frac{E_A}{k_B T_{\frac{1}{2}}}\right), \quad (3.10)$$

setting $\tau_0 = 1 \cdot 10^{-12}$ s and $\delta\omega_0 = 2\pi\delta\nu_B$ the activation energy for the exchange process can be roughly estimated to $E_A \sim 0.72$ eV.

Since the linewidth behavior of the narrow line gives strong evidence for molecular motion, temperature dependent ^1H spin-lattice relaxation experiments were performed.

3.4.2 $1/T_1$ Relaxation Rate

Fig. 3.11 presents the temperature dependent ^1H NMR spin-lattice relaxation rate $1/T_{1b}$ of the broad and $1/T_{1n}$ of the narrow line. With increasing temperature, $1/T_{1b}$ (broad line) follows an exponential increase, whereas $1/T_{1n}$ (narrow line) remains nearly constant. In the following, the spin-lattice relaxation behavior of broad and narrow line are discussed separately.

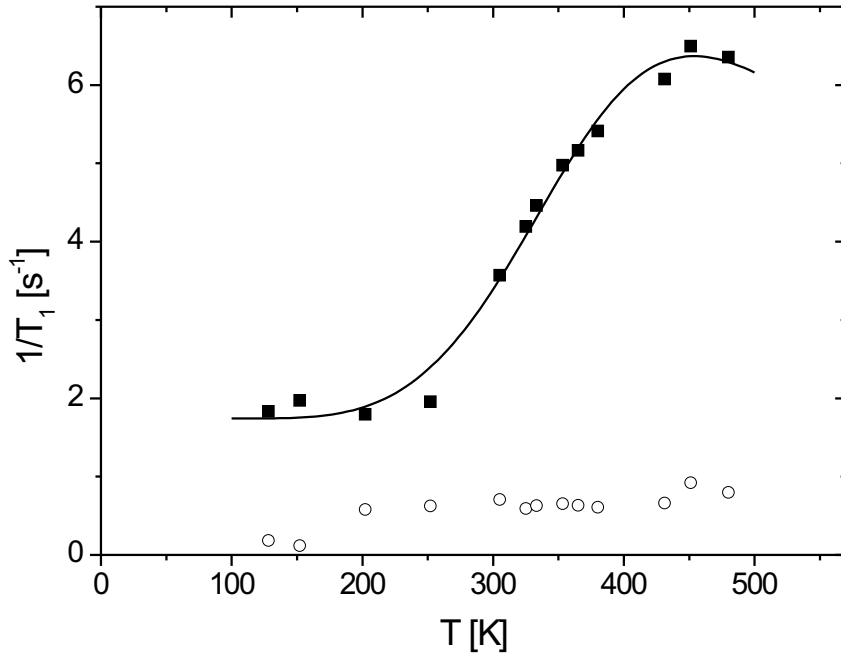


Figure 3.11: ^1H NMR spin-lattice relaxation rate $1/T_1$ for LiC_7 as function of temperature (narrow line: \circ and broad line: \blacksquare). The solid line is a fit assuming isotropic molecular reorientations with dipolar interactions. More details are given in the text.

Broad-Line Spin-Lattice Relaxation

The spin-lattice relaxation rate of the broad line, caused by the anisotropic rotation of the THF molecules, exhibits a maximum around a temperature of $T \sim 450$ K. The exponential increase of $1/T_{1b}$ with subsequent decrease is typically for a thermally activated BPP peak behavior due to proton dipole-dipole couplings. Using the relations for dynamically dipolar relaxation given in Chap. (2.2.3),

$$\frac{1}{T_{1b}} = \frac{3}{10} d^2 [J(\omega_0) + 4J(2\omega_0)], \quad (3.11)$$

$1/T_{1b}$ can be fitted with an activation energy $\Delta E \sim 0.13$ eV, an infinite temperature correlation time $\tau_0 \sim 1.7 \cdot 10^{-11}$ s and a dipolar coupling constant of $d \sim 2\pi \cdot 12 \cdot 10^3$ s⁻¹. By comparing Eq. 3.11 with relation Eq. 2.60 which describes dipolar spin-lattice relaxation using the second moment M_2 of a lineshape, M_2 can be calculated to $(M_2)_{relax} = 9/20 d^2 \sim 2.6 \cdot 10^9$ s⁻².

For the case of a Gaussian lineshape, the observed high temperature linewidth $\delta\nu_B \sim 2$ kHz corresponds to a second moment $(M_2)_{spectrum} \sim 1.2 \cdot 10^9 \text{ s}^{-2}$. This value is comparable to $(M_2)_{relax}$ and confirms the dipolar character of line broadening and spin-lattice relaxation.

Narrow-Line Spin-Lattice Relaxation

The spin-lattice relaxation rate $1/T_{1n}$ of the narrow line shown in Fig. 3.11 is rather low and slightly increasing with increasing temperature. This is compatible with a slow motion as expected for the high activation energy for isotropic rotation as discussed in the previous section.

3.4.3 Structural THF Arrangement

Concerning the structural THF and therefore the proton arrangement in the system, several scenarios are conceivable. In the following, comparisons with systems of THF co-intercalation in potassium intercalated graphite (K-GIC) as well as systems built up from polymer electrolyte matrix formations are drawn.

THF in GIC

From the point of chemistry, THF and potassium should form a stable coordinated complex. The main driving force for the geometrical THF arrangement are ionic interactions in between the strongly electronegative oxygen atoms and the positively charged Li^+ cations. Similarly due to electron affinity reasons, the THF-hydrogen atoms tend to point towards a graphene layer.

Facchini et. al [93] performed ^1H NMR of the graphite intercalation compound $\text{KC}_{24}(\text{THF})_2$. The authors claimed a free rotation of the THF molecules around their oxygen atom (dipolar axis) perpendicular in between adjacent graphene layers at room temperature (Fig. 3.12). The K^+ cations located halfway between the graphene planes pin the oxygen atoms to their immediate neighborhood.

Only for this perpendicular THF-arrangement, high stoichiometries of Li intercalation can be reached. Since the dimension of the THF molecules along their dipolar axis extends to 5.4 \AA , perpendicular standing THF molecules require a drastically enlargement of the graphene layer spacing d_s .

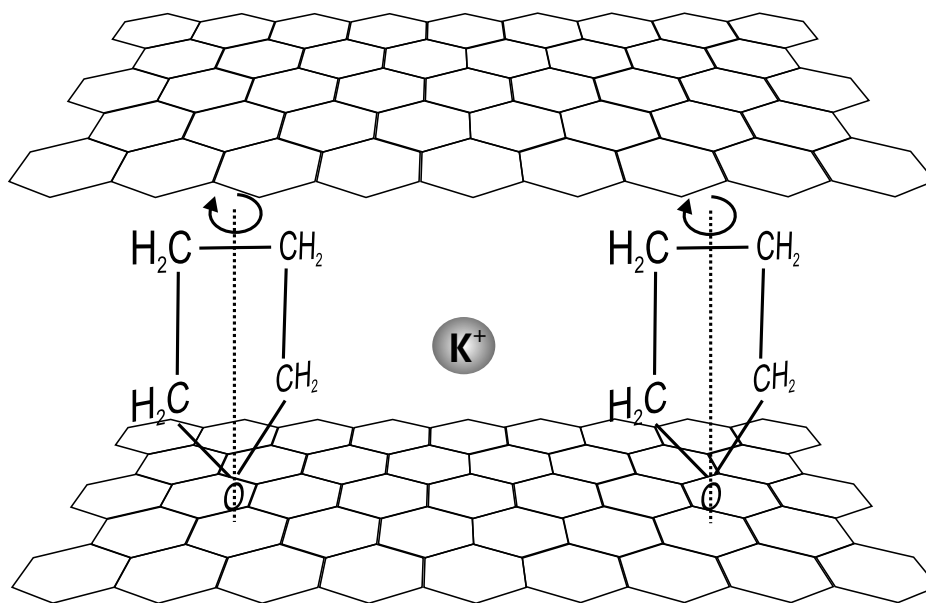


Figure 3.12: Schematic of potassium intercalation in graphite. At room temperature the cointercalated THF molecules show a rotation about their oxygen atoms in between two adjacent graphene layers.

Indeed XRD measurements proved an increase from $d_s = 3.35 \text{ \AA}$ in pure graphite to $d_s = 8.8 \text{ \AA}$ in stage I K-GIC binary compounds. Upon intercalation of the larger Li-THF ternary complexes, even an increase of the graphene layer spacing up to $d_s = 12.4 \text{ \AA}$ was reported [92].

Similarly to the situation in graphite, in SWNT an expansion of the triangular SWNT-bundle lattice has to be expected upon Li-THF intercalation. However, also imaginable would be a distortion of the triangular SWNT-bundle lattice. For the case of a simple lattice expansion, the lattice spacings can be easily calculated by geometrical considerations.

THF in SWNT

Following the sketched scenario of $\text{KC}_{24}(\text{THF})_{(2)}$ with THF molecules standing perpendicularly to the hexagonal carbon surface and alkali ions located halfway between the graphene planes, a conceivable Li-THF-SWNT configuration is illustrated in Fig. 3.13. The Li^+ cations are located halfway between two adjacent SWNT and pin the oxygen-(THF) atoms to their immediate neighborhood. The number of

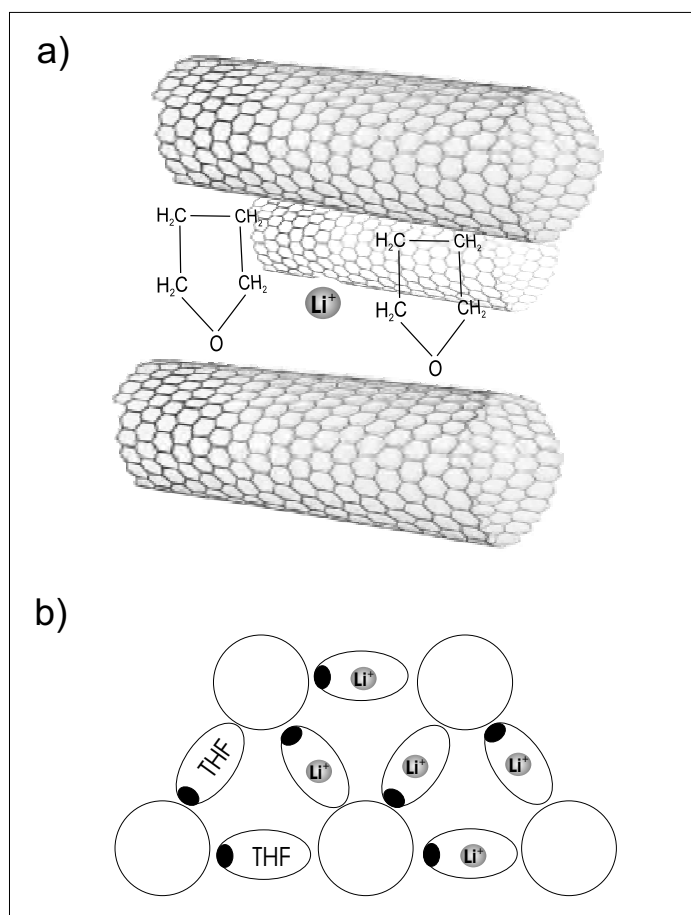


Figure 3.13: Schematic of sites for intercalation of THF-Li complexes in a SWNT bundle with triangularly arranged individual nanotubes. a) side view. b) top view. The black dots symbolize oxygen atoms. The Li⁺ ions are located above and below the THF molecules.

next neighbor THF molecules is determined by the Li-THF coordination number. Applying the values of lattice expansions in $\text{KC}_{24}(\text{THF})_{(2)}$, an expansion of the SWNT bundle lattice of 30% has to be expected.

Since in the investigated Li intercalated SWNT samples, XRD measurements never yielded any diffraction patterns of carbon nanotubes, protons or Li ions, a strong disorder in the SWNT-Li-THF system has to be assumed [110, 132, 162, 173]. This distortion might originate from the existence of various Li-THF coordination numbers as well as a wide distribution of SWNT diameters in the samples.

The discussed geometrical THF-arrangements strongly remind to atomic configurations in polymer electrolytes matrices like poly(ethylene oxide) (PEO). Its monomer ethylene oxide ($\text{C}_2\text{H}_4\text{O}$) is very similar to THF and the polymerized form tends to form crystalline complexes enwrapping metal ions like Li^+ . Thereby the ions are able to move along crystalline channels formed by the PEO matrix, while only a restricted sequential motion of the polymer chains (for example by bond rotations) is possible [232, 233].

Transferring this picture to Li-intercalated SWNT, the presence of the ^7Li NMR $\text{Li}^{(\alpha)+}$ line and related spin-lattice relaxation could arise from a Li^+ diffusion in channels formed by a THF-matrix in the interstitial channels of the SWNT bundle. The THF matrix could explain the observed broad proton line in the spectra of Fig. 3.9 since THF molecules in between adjacent SWNT exhibit a restricted rotation around their dipolar axis with an activation energy of $\Delta E \sim 0.13$ eV. At higher temperatures, formation of detached THF molecules is possible. These detached molecules are able to diffuse along the interstitial channels of the SWNT bundle, which in the expanded lattice provide enough space for an additional isotropic THF molecule rotation. This explains the appearance of a narrow ^1H NMR line at higher temperatures.

3.4.4 Negative Line Shifts

Yet unclear is the origin of the huge negative shifts of the broad and the narrow ^1H NMR line. Conceivable are both, a negative paramagnetic Knight shift or a large diamagnetic shielding of the carbon nanotubes. In the following both effects will be discussed in consideration of the above discussed structural THF arrangement.

- The origin of **negative paramagnetic Knight shifts** is a negative transferred hyperfine coupling at the site of the protons (see Chap. 2.1.4). The Knight shift comprising the hyperfine coupling is given by Eq. 2.10 and Eq. 2.11 with

$$K_{iso} = \frac{1}{2} \frac{\gamma_e}{\gamma_n} a_{iso} \hbar n(\varepsilon_F). \quad (3.12)$$

By applying the DOS at the Fermi level $n(\varepsilon_F)$ calculated in Chap. (3.2.2) from ^{13}C NMR measurements, as well as the ^1H NMR line shift of the broad proton line in Fig. 3.9, a lower limit of the isotropic hyperfine coupling constant can be estimated to $a_{iso} \sim -2\pi \cdot 10^9 \text{ s}^{-1}$.

However, DFT calculations considering the above discussed structural THF arrangement resulted an average hyperfine coupling constant of only $a_{iso} \sim -2\pi \cdot 5.6 \times 10^6 \text{ s}^{-1}$. Applying again the $n(\varepsilon_F)$ extracted from ^{13}C NMR measurements to this value yields an upper limit of the Knight shift of $K_{iso} \sim -1.6 \text{ ppm}$. This value is much smaller than the measured Knight shift.

The observed Knight shift of 30 ppm would result only if the THF orbitals would contribute 100% to the SWNT conduction band and the DOS would be a factor of twenty larger. This is very unlikely. The conclusion is that the observed shift is of different origin, probably a diamagnetic shift.

- The reason for a large **diamagnetic shift** could be a diamagnetic shielding of the carbon nanotube bundles. Such a diamagnetic shielding is expected to originate from an anisotropic diamagnetic susceptibility caused by SWNT π -electron orbital magnetism of the sp^2 carbon bonds.

However, in case of a diamagnetic shielding, an similar negative shift would be expected for all types of THF molecules in the sample. Since the THF molecules corresponding to the narrow ^1H NMR line exhibit only a weak diamagnetic shift, an averaging of the anisotropic susceptibility upon diffusion has to be assumed.

On the contrary, THF molecules corresponding to the broad and strongly negatively shifted ^1H NMR line are subject to the full diamagnetic SWNT shielding since motion is restricted to a rotation around the dipolar THF axis.

3.5 Comparison of ^1H and ^7Li NMR $1/T_1$ Relaxation Rates

Both, H and Li nuclei show a thermally activated motion behavior. In the following a possible correlation of these two types of motions is discussed. For a direct comparison of the ^1H and ^7Li NMR spin-lattice relaxation results, the following aspects have to be considered:

- ^1H and ^7Li NMR spin-lattice relaxation measurements were performed on different samples (^1H : LiC_7 , ^7Li : LiC_{10}). Nevertheless, since ^7Li NMR on LiC_7 and on LiC_{10} show a similar relaxation behavior in temperature, the ^7Li NMR $1/T_1$ results can be treated universally valid for LiC_7 and LiC_{10} . The spin-lattice relaxation measurements on LiC_7 (^1H) and LiC_{10} (^7Li) can be directly compared.

- The ^1H and ^7Li NMR $1/T_1$ measurements were performed at different Larmor frequencies. Nevertheless, correlation rates and therewith activation energies can be directly compared, since according to the BPP-maximum condition $\omega_0\tau_c = 1$ only the BPP-maximum position will be shifted for different Larmor frequencies.

The activation energies $\Delta E_{\text{Li}} \sim 0.4$ eV and $\Delta E_{\text{H}} \sim 0.1$ eV differ by a factor of four which implicates that dynamical Li-H interaction is not very effective. Rotational proton (THF) and diffusive lithium motion are predominantly not dynamically correlated.

3.6 Summary

Lithium was chemically intercalated in SWNT bundles by using solutions of aromatic hydrocarbons, tetrahydrofuran (THF) and SWNT.

^{13}C NMR spectral analysis shows a reduction of the spectral anisotropy upon Li intercalation. However, this reduction is weaker than expected by comparison with results from Li-GIC, which can be explained by an **incomplete charge transfer at higher intercalation levels**. This assumption is emphasized by ^{13}C NMR spin-lattice relaxation measurements, where the behavior of $n(\varepsilon_F)$ does not uniformly follow the Li intercalation level. Nevertheless, upon intercalation the system reveals a pure metallic behavior and no signature for semiconducting SWNT can be found. At low temperatures, ^{13}C NMR shows an increase of $1/T_1$ with decreasing temperature. This relaxation behavior is a possible indication for the presence of either unpaired electron spins due to defects or paramagnetic impurities or the opening of a band-gap at low temperatures.

By performing **^7Li NMR experiments**, the presence of **two types of Li-nuclei** with different environments was shown: at low intercalation levels the first intercalated Li are of type **completely ionized α -type Li ions**. While increasing the Li concentration, a second type of **partially ionized β -type Li** is adsorbed by the SWNT host.

For both types of Li ions, considerable line broadenings suggest a large distribution of quadrupole frequencies. This quadrupole frequency distribution could arise from the existence of various Li-THF coordination numbers as well as a wide distribution of SWNT diameters.

- **β -type Li**: the origin of the above sketched limited Li-C charge transfer is explainable by the presence of $\text{Li}^{(\beta)+}$ ions in the system. ^7Li NMR demonstrates a remarkable Knight shift for these nuclei as well as a strong hyperfine coupling to SWNT conduction electrons. Both facts suggest a **Li(2s)-C(2p) hybridization**.

A charge transfer limitation due to the presence of THF molecules in the system is rather unlikely. The electron charge transfer occurs independently of the presence of THF molecules during the first step of intercalation by transferring electrons from the aromatic hydrocarbon anion radicals directly to the SWNT host.

- **α -type Li:** ^7Li NMR on the α -type nuclei proves a high-temperature dynamical process with an activation energy of $\Delta E \sim 0.4$ eV which can be interpreted as a **$\text{Li}^{(\alpha)+}$ cation diffusion** along the interstitial channels of the SWNT bundles.

However, the measured activation energy is 2 times higher than reported for a similar Li motion process in the first stage Li-GIC compound LiC_6 with $\Delta E = 0.22$ eV [231]. Actually the activation energy in the present intercalated SWNT is expected to be higher since strong interactions between Li and C must be overcome (β -Li). Additionally, a hindered nearly one dimensional motion of Li in the channels of the carbon nanotube bundle is expected rather than a two dimensional diffusion as in graphite.

Temperature dependent ^1H NMR experiments have proved the existence of **two types of inequivalent THF solvent molecules** with different chemical environments and dynamical behavior.

- **At low temperatures** only one broad line is observable. THF molecules perpendicularly arranged in between adjacent SWNT presumably exhibit a **restricted rotation around their dipolar axis** with an activation energy of $\Delta E \sim 0.13$ eV. The Li^+ cations are located halfway between two adjacent SWNT and pin the oxygen-(THF) atoms to their immediate neighborhood.
- **At higher temperatures** a narrow dipolar broadened line develops due to detaching and formation of THF molecules **isotropically rotating and diffusing** along the interstitial channels of the SWNT bundles.

The two types of THF molecules are most likely coupled by a thermally activated exchange process with an activation energy of $E_A \sim 0.72$ eV.

The remarkable diamagnetic shift of the ^1H NMR lines suggest an extremely large **diamagnetic shielding of the carbon nanotubes** due to high anisotropic diamagnetic susceptibilities. This shielding is expected to likewise affect the ^7Li NMR spectra which suggests an underestimation of the observed ^7Li NMR line positions.

^1H and ^7Li NMR dynamics are predominantly not dynamically correlated. Nevertheless, Li and THF are deeply structural coupled, since they coexist confined in a nearly one dimensional system.

Chapter 4

Cesium Intercalated SWNT

In this chapter, vapor phase Cs intercalation in connection with a new preparation method for obtaining well defined Cs intercalation stoichiometries is treated. Using high resolution ^{13}C and static ^{133}Cs NMR techniques, the dynamical and structural properties of the intercalated system are investigated. The observed Cs-C hybridization and Cs^+ cation diffusion are discussed and the charge transfer characteristics of the system is compared with Cs intercalated graphite.

4.1 Sample Preparation and Experimental Conditions

Similarly to the sample production process described in Chap. (3.1), SWNT samples were synthesized by the electric arc method with 10% ^{13}C isotope enrichment and a catalyst mixture in the molar proportions of 96.8% C, 2.1% Rh and 1.1% Pt. After Raman-selection the pristine SWNT bundles were vapor phase intercalated with cesium following the two-bulbs method [174]. By using a temperature gradient between the alkali metal and the SWNT ($T_{\text{C}} = 186^\circ\text{C}$, $T_{\text{Cs}} = 200^\circ\text{C}$), a saturation intercalation stoichiometry of CsC_8 is expected [16,96].

In order to obtain samples with lower intercalation densities under controlled conditions, the saturation intercalated sample CsC_8 was mixed with pristine SWNT in different ratios. Upon vacuum annealing at $T = 300^\circ\text{C}$ for 3 days, Cs primarily deintercalates and uniformly disperses on the complete sample. Subsequent cooling in a closed vessel is expected to re-intercalate the sample leading to new intercalation stoichiometries CsC_x ($x > 8$). All the samples were sealed under high vacuum.

^{13}C NMR experiments were carried out on a *Bruker ASX200* spectrometer working at a magnetic field of 4.7 T and a ^{13}C NMR Larmor frequency of 50.3 MHz. Static spectra were obtained in the temperature range of 10 – 300 K. Room temperature

^{13}C MAT NMR was performed on a *Varian/Chemagnetics Infinity 300* spectrometer at a magnetic field of 7 T and a ^{13}C NMR Larmor frequency of 75.7 MHz. ^{133}Cs NMR measurements were carried out on a home built pulsed NMR spectrometer equipped with a sweep magnet working at 9.1 T and a ^{133}Cs NMR Larmor frequency of 50.7 MHz. The ^{13}C NMR line shifts were referred to TMS and the ^{133}Cs NMR line shifts to an aqueous solution of 1M CsNO_3 as an external standard.

4.2 ^{13}C NMR

4.2.1 Static Spectra

In order to estimate the stoichiometries of the Cs intercalated SWNT samples, static ^{13}C NMR was performed on the various mixtures of pristine SWNT and CsC_8 just before vacuum annealing. As the samples without heat treatment are composed of two well defined phases of pristine and saturation intercalated SWNT, the associated

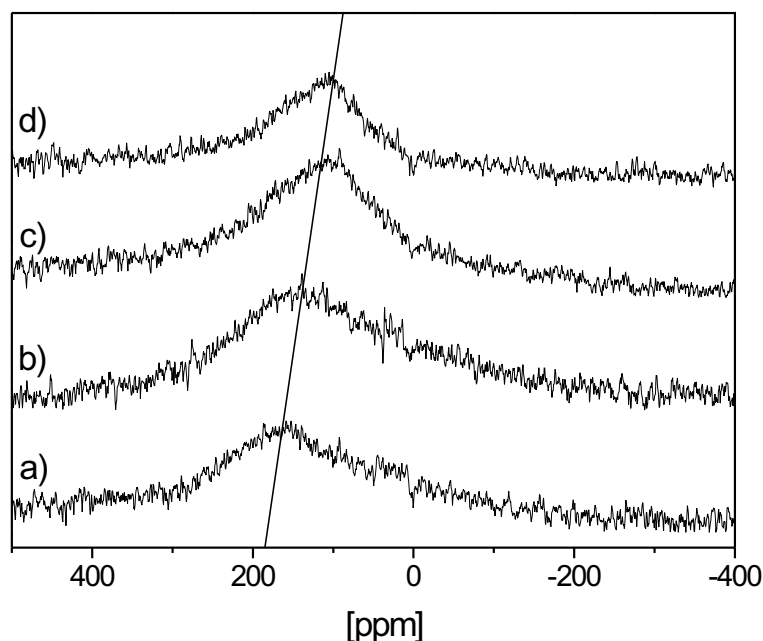


Figure 4.1: Static room temperature ^{13}C NMR spectra of various mixtures of pristine SWNT and CsC_8 just before vacuum annealing. The Larmor frequency was 50.3 MHz. From fits of the spectra, the following stoichiometries were extracted as described in the text: (a) Pristine SWNT, (b) CsC_{34} , (c) CsC_{12} , (d) CsC_8 . The straight line is a guideline illustrating the shift of the maximum intensity upon increasing Cs concentration.

spectra are expected to be composed of the ^{13}C NMR lines of pristine SWNT and CsC_8 with their weights describing the exact stoichiometries of the samples.

All static ^{13}C NMR spectra were recorded using a Hahn echo pulse sequence and Fourier transformation. The spectra of pristine SWNT (a) and CsC_8 (d) strongly differ as can be seen in Fig. 4.1. Therefore, combining the pristine and CsC_8 tensorial lineshapes allows to accurately estimate the stoichiometry of the investigated samples by changing the weights of each tensor. Following this concept, seven different samples were characterized with stoichiometries CsC_x ($x=8, 12, 30, 31, 33, 34, 40$).

In Fig. 4.2 static ^{13}C NMR spectra of pristine (a) and saturation intercalated SWNT CsC_8 (b) are directly compared. The tensorial powder pattern lineshape of pristine SWNT reveals a maximum around 150 ppm and an anisotropy of about 450 ppm, whereas in the Cs intercalated SWNT sample the maximum is diamagnetically shifted to 100 ppm and the anisotropy is reduced from 450 ppm to 200 ppm. Possibly, an inversion of the tensor lineshape in CsC_8 is present.

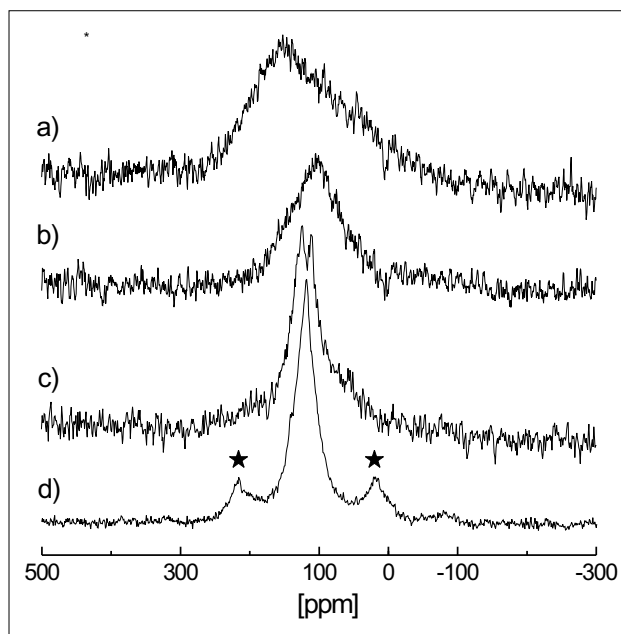


Figure 4.2: Static room temperature ^{13}C NMR spectra of (a) pristine SWNT and (b) Cs intercalated SWNT CsC_8 . (c): MAS spectrum of Cs intercalated SWNT CsC_{31} after vacuum annealing. The isotropic sp^2 line splitting is clearly visible. (d): high resolution MAS spectra of the corresponding pristine SWNT. The symbols (★) are for the spinning sidebands. All spectra were recorded at a Larmor frequency of 50.3 MHz. For more details refer to the text.

The observed reduction of the anisotropy is comparable with the anisotropy reduction behavior in higher stage GIC, where the reduction is known to account for about 1800 ppm/electron (cp. Eq. 2.14). This corresponds to a reduction 225 ppm for a stoichiometry of CsC_8 .

4.2.2 MAS

In order to estimate the isotropic ^{13}C NMR line positions, room temperature MAS was performed at a spinning rate of 5 kHz. Fig. 4.2 (c) shows the ^{13}C MAS NMR spectrum of CsC_{31} . The spectrum consists of two isotropic lines located around 111 ppm and 128 ppm. However, the weights of the two lines cannot be extracted directly since the spectrum was not recorded fully relaxed. Relative to the isotropic line position of 119 ppm in the corresponding pristine SWNT material (Fig. 4.2 (d)), the two lines are paramagnetically and diamagnetically shifted.

The appearance of two isotropic lines is rather surprising. In case of a simple Cs intercalation process, a charge transfer from Cs to the SWNT and consequentially a dominant positive Knight shift is expected. Compared to the line position in pristine SWNT, the isotropic line position in CsC_{31} should only be paramagnetically shifted and a diamagnetic shift is rather unusual.

In order to exclude measurement errors as source for the isotropic double-line structure in the spectrum, as well as resolving the lines in better resolution, MAT experiments were performed. MAT as a two-dimensional Fourier transform technique is able to properly resolve splittings of several isotropic lines even in case of strong spectral line overlaps.

4.2.3 MAT

The ^{13}C MAT NMR experiment was carried out using the 5-pulse sequence illustrated in Fig. 2.1. Data acquisition was performed directly after the last $\pi/2$ pulse. The MAT rotor frequency was 150 Hz and τ varied from 0.1 s to 6 s within 40 steps. The FID acquisition during t_a included 1024 points with a dwell time of 4 μs . The MAT experiments were performed on pristine SWNT as well as Cs intercalated SWNT CsC_{30} . Two dimensional Fourier transformation as a function of τ and t_a results the 2D-MAT spectrum of pristine SWNT in Fig. 4.3.

It is important to note, that projections of the 2D-spectrum onto the two axis of the contour plot in Fig. 4.3 do not directly represent the isotropic and CSA

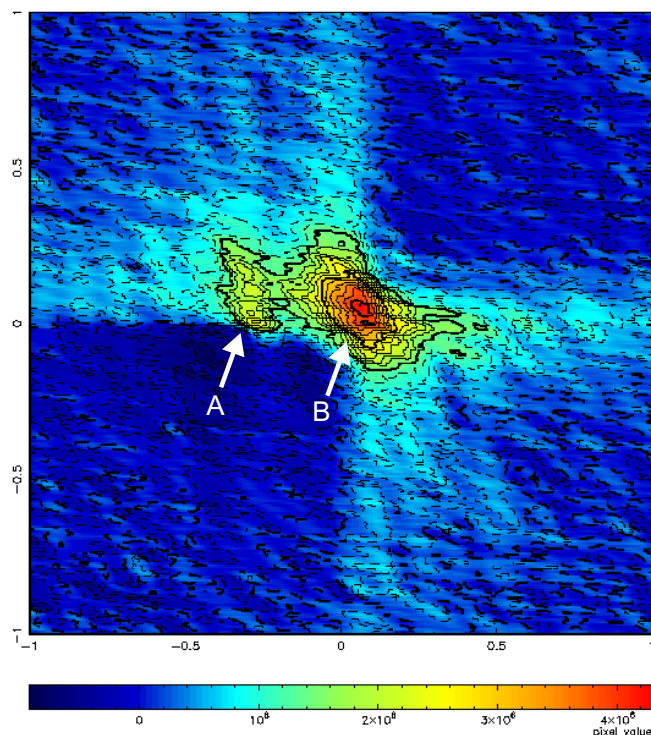


Figure 4.3: Room temperature ^{13}C MAT NMR spectrum of pristine SWNT at a Larmor frequency of 75.7 MHz. (A) indicates an artifact peak, whereas (B) can be assigned to SWNT. The scaling of the axis is displayed in arbitrary units.

patterns, since data acquisition is already started after the last $\pi/2$ -pulse of the MAT pulse sequence (see Chap. 2.1.2). Therefore, the scalings of the axis in Fig. 4.3 are displayed in arbitrary units. Projecting the spectrum onto the acquisition dimension axis at an angle $\arctan(\zeta_2/3\zeta_1)$ will result in the isotropic-shift spectrum, while projection on a perpendicular axis will result in the CSA powder pattern. $\zeta_{1/2}$ are defined by the number of acquisition points and dwell times given by τ and t_a .

In the 2D-spectrum of Fig. 4.3 two main peaks A) and B) are clearly visible. However, the peak A) is an artifact and only peak B) represents the real 2D-spectrum of pristine SWNT.

By performing the described spectral projections onto the acquisition dimension axis, the isotropic ^{13}C NMR spectrum in Fig. 4.4 was extracted from the MAT 2D-data. In order to calibrate frequency displacement and scaling, preliminary ^{13}C MAT NMR experiments with subsequent 2D-Fourier transformations and isotropic spectra calculations were performed using C_{60} ($\delta_{iso} = 143$ ppm) and Adamantane (2 isotropic lines, $\delta_{iso} = 28 - 38$ ppm) as a reference.

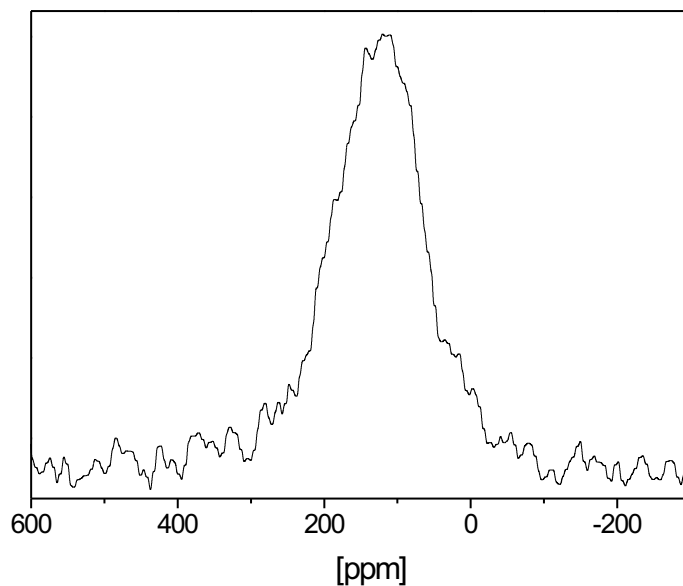


Figure 4.4: Isotropic ^{13}C NMR spectrum of pristine SWNT at room temperature at a Larmor frequency of 75.7 MHz. The spectrum was extracted from the corresponding 2D-MAT experiment.

The ^{13}C NMR spectrum in Fig. 4.4 is typical for sideband-free isotropic lineshape in pristine SWNT. The isotropic line is paramagnetically shifted to about 126 ppm which is comparable to results from MAS experiments on pristine SWNT as described in Chap. (2.3). Additional line broadenings arise from the imperfect projection of the 2D-spectrum on the acquisition axis.

In Fig. 4.5 the ^{13}C NMR 2D-contour plot of CsC_{30} is displayed. Besides the artifact peak A) already known from pristine SWNT, two peaks B) and C) are observable. Projecting the spectrum onto the acquisition dimension axis yields the isotropic ^{13}C NMR spectrum in Fig. 4.6. Contrary to the isotropic spectrum of pristine SWNT which consists of only one main peak around 126 ppm, two sp^2 peaks observable. Due to the broad spectrum, the line positions can only be roughly estimated to around 84 ppm and 124 ppm. Nevertheless, the presence of two peaks confirms the isotropic line splitting observed by MAS in Fig. 4.2 (c).

The sp^2 -line splitting suggests the existence of two inequivalent carbon sites in the Cs intercalated samples. In order to allow further interpretations of the observed shifts and line splittings, ^{13}C NMR spin-lattice relaxation measurements were carried out.

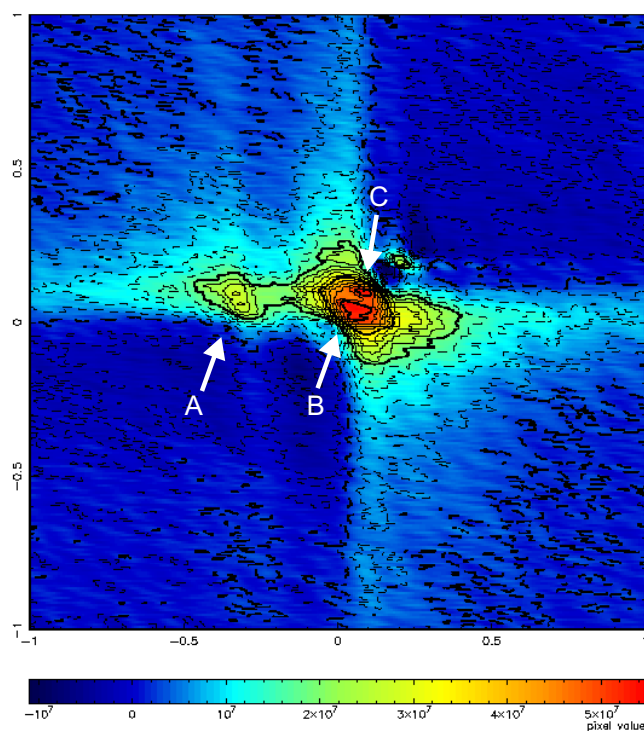


Figure 4.5: Room temperature ^{13}C MAT NMR spectrum of CsC_{30} at a Larmor frequency of 75.7 MHz. (A) indicates an artifact peak, whereas (B) and (C) can be assigned to ^{13}C nuclei of intercalated SWNT. The scaling of the axis is displayed in arbitrary units.

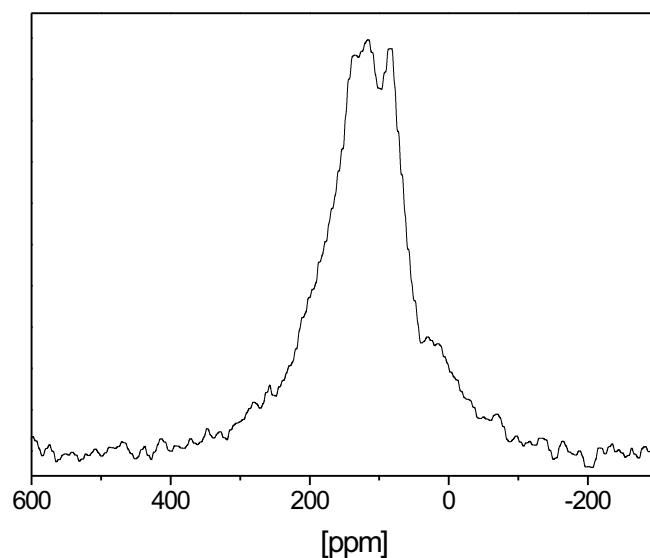


Figure 4.6: Isotropic room temperature ^{13}C NMR spectrum of CsC_{30} at a Larmor frequency of 75.7 MHz. The spectrum was extracted from the corresponding 2D-MAT experiment. A splitting of the isotropic sp^2 line is clearly visible.

4.2.4 $1/T_1$ Relaxation Rate

All ^{13}C NMR spin-lattice relaxation rates $1/T_1$ were obtained at a Larmor frequency of 50.3 MHz using a saturation recovery pulse technique and a Hahn echo as a detection pulse. At all temperatures for all samples, the magnetization recovery follows a biexponential recovery curve, confirming the two inequivalent carbon sites. The magnetization recovery is composed of a fast and a slow relaxation component. As shown in Fig. 4.7, the fraction of the slow relaxation component decreases from 75% in CsC_8 to 50% in CsC_{31} and is constant in temperature for each sample.

In pristine SWNT, the magnetization recovery typically consists of two components with a ratio of 60:40. However, ^{13}C NMR spin-lattice relaxation in this system is different from the present relaxation processes in Cs-SWNT. In pristine SWNT, room temperature relaxation times are in the order of 5 s (40%) and 90 s (60%), respectively, whereas in CsC_8 the corresponding relaxation times are $T_{1a} \sim 0.25$ s and $T_{1b} \sim 2.3$ s. In general, the two relaxation components in pristine SWNT are attributed to relaxation of semiconducting (60%) and metallic (40%) carbon nanotubes [34, 193, 194]. The higher relaxation rate of the spin system in CsC_8 indicates an increased metallic character of the SWNT system.

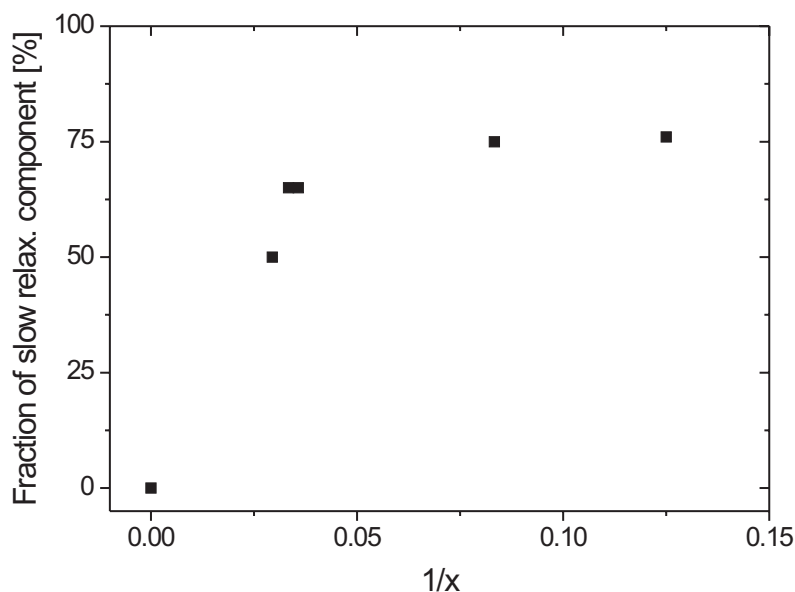


Figure 4.7: Stoichiometry dependence of the fraction of the slow relaxation component in the ^{13}C NMR magnetization recovery for the samples CsC_x with $x = 8, 12, 30$ and 40 , respectively.

As shown in Fig. 4.8 (top), both relaxation components $1/T_{1a}$ (high relaxation rate, 25%) and $1/T_{1b}$ (low relaxation rate, 75%) follow a linear increase with increasing temperature, which points to a Korringa type relaxation process of the ^{13}C nuclei. In order to prove a Korringa relaxation in the complete observed temperature range, the temperature dependence of $T_{1a}T$ and $T_{1b}T$ is plotted in Fig. 4.8 (bottom).

For Korringa relaxation, T_1T is expected to be constant and independent of temperature, which is not the case for both $T_{1a}T$ and $T_{1b}T$. Below a temperature of $T \sim 150$ K, $T_{1b}T$ deviates strongly from the Korringa law. Also $T_{1a}T$ shows a temperature dependent behavior varying from a constant T_1T value, however less pronounced.

A similar deviation from the Korringa law was already observed for ^{13}C NMR spin-lattice relaxation measurements in Li intercalated SWNT which is discussed in detail in Chap. (3.2.2). The origin of the deviation was explained by either localized electron spins or the opening of a band gap. Here, a similar mechanism could be active. However, the high temperature of 150 K where the deviation from the Korringa law in CsC_8 sets in makes the scenario of a band-gap-opening rather unlikely. Furthermore, relaxation due to the development of Rh superparamagnetism at low temperatures is also rather improbable, since Rh clusters show incipient superparamagnetism only below 93 K. This leaves localized paramagnetic relaxation due to impurities and defects like dangling bonds as the main reason for the strong increase of T_1T at low temperatures.

Similarly to the procedure in Chap. (3.2.2), the slope of the linear $1/T_1$ dependence in Fig. 4.8 (top) enables to determine the density of states at the Fermi level $n(\varepsilon_F)$ by using the relation

$$\frac{1}{T_1T} = \frac{2\pi k_B}{\hbar} S_K A_{dip}^2 n(\varepsilon_F)^2 \quad \text{with}$$

$$A_{dip} = \frac{2}{5} \frac{\mu_0}{4\pi} \gamma_n \gamma_e \hbar^2 \left\langle \frac{1}{r^3} \right\rangle.$$

However, an exact treatment generally requires detailed knowledge of the both, the dipolar hyperfine coupling constant A_{dip} , as well as the Korringa enhancement factor S_K . Since these values were not measured in CsC_8 until now, in the following the Korringa enhancement factor will be assumed to $S_K = 1$. By using the dipolar hyperfine coupling constant A_{dip} of potassium intercalated C_{60} (K_3C_{60}), the DOS at the Fermi level $n(\varepsilon_F)$ for various Cs stoichiometries was calculated.

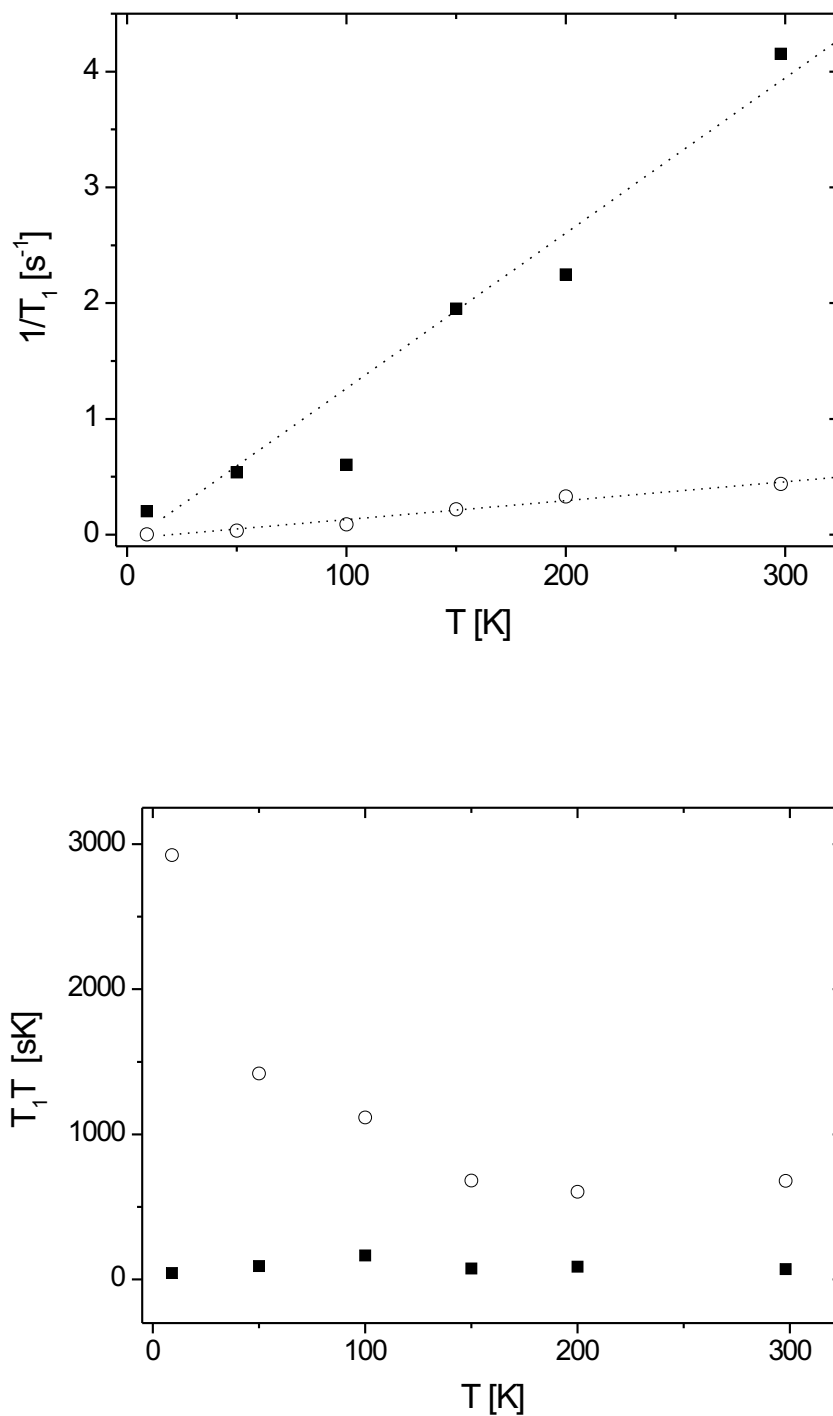


Figure 4.8: ^{13}C NMR temperature dependence of $1/T_1$ (top) and $T_1 T$ (bottom) for CsC_8 . The two spin-lattice relaxation components are T_{1a} (■) and T_{1b} (○).

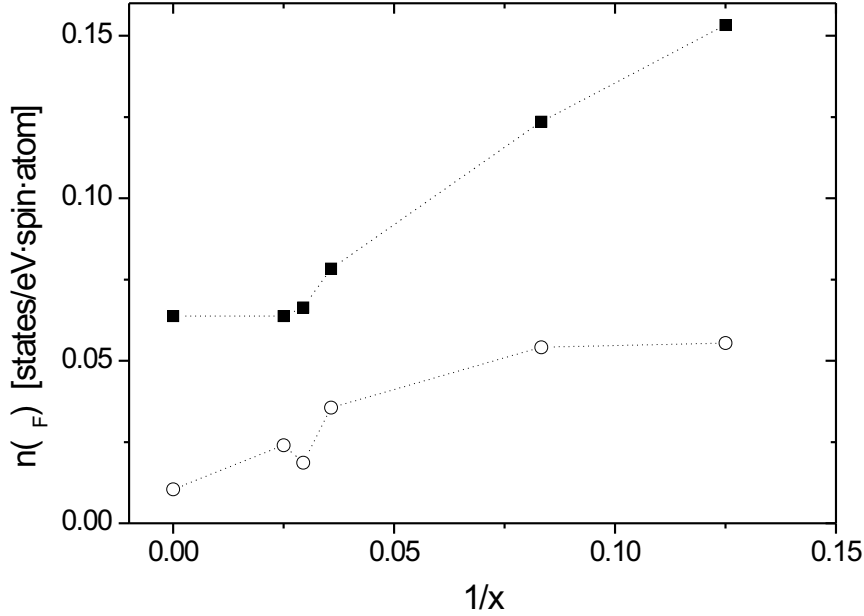


Figure 4.9: Density of states at the Fermi level $n(\varepsilon_F)$ for various stoichiometries CsC_x . The $n(\varepsilon_F)$ were derived from ^{13}C NMR $1/T_1$ relaxation measurements as described in the text.

As shown in Fig. 4.9, for both types of relaxing ^{13}C nuclei, $n(\varepsilon_F)$ follows a monotonic increase with increasing Cs intercalation level. Such a behavior is well understandable, considering that with increasing Cs concentration the amount of electron charge transferred to the SWNT is expected to simultaneously increase.

4.2.5 Discussion of ^{13}C NMR Data

The two $1/T_1$ components as well as the spectral lines suggest the presence of at least two different kinds of carbon sites with different environments. In a first simple consideration, the appearance of two carbon sites could either be explained with inhomogeneous intercalation of Cs, finite size bundle effects or localized Cs-C effects.

- **Inhomogeneous Cs intercalation** corresponds to different, in space well separated domains of intercalated SWNT with various Cs stoichiometries. However, it is rather questionable why exactly two well defined carbon environments should coexist in this scenario, even though this could explain two ^{13}C NMR lines with two associated spin-lattice relaxation components.

The applied two-bulb sample preparation method for Cs intercalation in SWNT is the same method as usually applied for the preparation of A_3C_{60} ($\text{A} = \text{K}, \text{Rb}$,

Cs). From A_3C_{60} it is known, that for higher temperatures (200-300 °C) alkali diffusion with an activation energy around 0.1 eV provides a very homogeneous alkali intercalation throughout the whole sample [102,103]. Since SWNT can be considered as a comparable system with diffusion activation energies in the same order of magnitude it can be assumed, that a homogeneous Cs distribution in the present samples occurs rather than a random inhomogeneous intercalation.

- **Finite size effects** of the bundle could also play an important role, since SWNT bundles are finite crystal structures with sizes of a few nanometers. Due to completely different structural environments, C atoms corresponding to SWNT located on the outer surface of the bundle are expected to be subject to modified interactions compared to C atoms on SWNT in the center of a bundle. Even though, generally samples exhibit a wide random distribution of bundle sizes, a categorical subclassification of the structure into bundle surface- and 'bulk' is always possible. Since 1H NMR on Li intercalated SWNT proved a large diamagnetic susceptibility of the SWNT bundle structure (see Chap. 3.4.4), the effect of diamagnetic shielding for SWNT located on a bundle surface or SWNT located in the 'bulk' of a bundle are expected strongly differ.

Therefore, finite size effects are supposed to substantially influence ^{13}C NMR spectra and spin relaxation. This could also explain the diamagnetic shift of one of the observed ^{13}C NMR isotropic lines relative to the isotropic pristine SWNT line position.

- Another possibility could arise from an **in plane localization** of the density of states which was observed in stage- n alkali-GIC ($n \gg 2$), where only every n -th graphene plane has a neighboring alkali layer [94,95].

This effect limits the electron charge distribution to neighboring graphene planes and results in two well defined densities of states for 1) direct alkali-neighbor graphene planes and 2) graphene planes distant by more than two graphene sheets away from the alkali ion layer.

Accordingly, transferring this scenario to Cs-SWNT, the higher DOS and the stronger paramagnetically shifted line could be attributed to Cs ions located next to the SWNT, whereas the lower DOS and the less paramagnetically shifted line would correspond to SWNT not in direct contact with Cs ions.

In order to understand the structure and dynamics of the intercalated Cs ions, ^{133}Cs NMR experiments were performed on the samples CsC_8 and CsC_{30} .

4.3 ^{133}Cs NMR

4.3.1 Nutation Experiments

Preliminary ^{133}Cs NMR FID experiments on the sample CsC_{31} (not shown here) have given evidence for a broad ^{133}Cs NMR spectrum. In order to determine correct $\pi/2$ pulse length to excite the complete spectrum, nutation experiments were carried out. Fig. 4.10 shows the ^{133}Cs NMR nutation experiment on the sample CsC_{30} and a fit (solid line) using a $\sin(\alpha)$ function. The maximum FID amplitude is obtained at a $\pi/2$ pulse length of $3.2 \mu\text{s}$. For comparison, calibrating the spectrometer with CsNO_3 yielded a $\pi/2$ pulse length of $2.4 \mu\text{s}$. The longer pulse length in the intercalated carbon nanotube sample can be attributed to a screening of the electromagnetic field of the pulse due to the high conductivity of SWNT.

As Cs atoms are quadrupolar nuclei, powder spectra consist of the central transition as well as satellite lines. A selective excitation of the central transition enhances the nutation frequency by a factor 4 for Cs (Chap. 2.1.5). For an aqueous solution of CsNO_3 , in general a complete excitation of the spectrum can be expected. Since the $\pi/2$ pulse length of CsNO_3 and CsC_{30} are comparable, a full excitation of the spin system in CsC_{30} can be concluded.

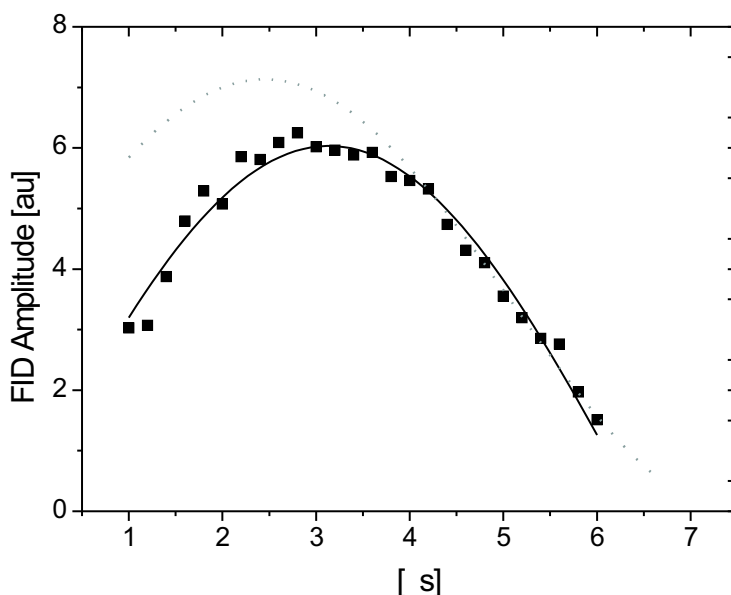


Figure 4.10: ^{133}Cs NMR nutation experiment on CsC_{30} (■) at room temperature. The solid line is a fit using a $\sin(\alpha)$ function, which describes the dependence of the FID amplitude on the pulse angle α . For comparison, the ^{133}Cs NMR nutation of an aqueous solution of CsNO_3 is shown as dotted points.

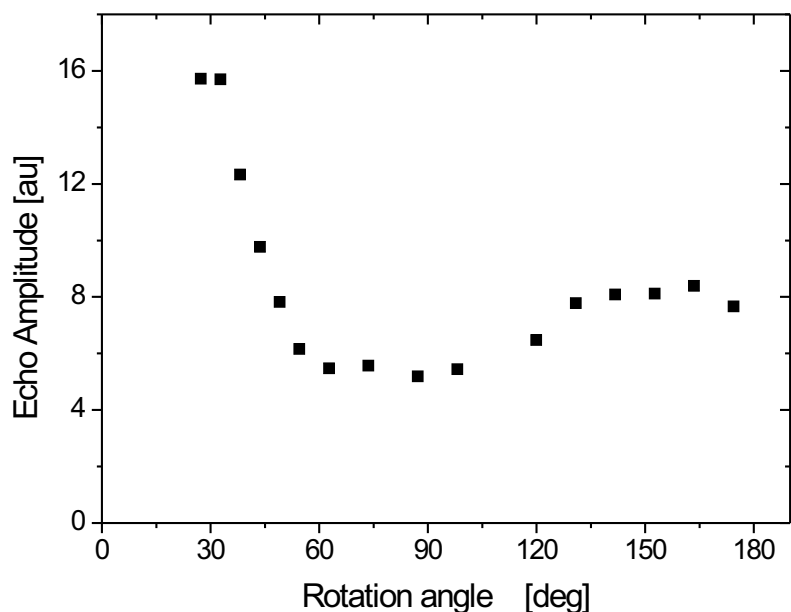


Figure 4.11: Echo amplitude of the ^{133}Cs NMR $\pi/2 - \beta$ experiment on the sample CsC_{30} (■) at room temperature. The amplitudes were recorded as a function of the 2nd pulse angle β .

4.3.2 $\pi/2 - \beta$ Experiments

In general, the spin echo height at time $t = 2\tau$ after a $\pi/2 - \tau - \beta$ pulse sequence varies strongly with the rotation angle β . In Chap. (2.1.5) it was shown that in the case of electric quadrupolar interactions, the optimum pulse angle β depends on the spin quantum number.

The maximum echo amplitude in CsC_{30} is obtained for a β -pulse angle of $\beta_{\text{opt}} \sim 30^\circ$ as can be seen from Fig. 4.11. This value is in good agreement with theoretical calculations of quadrupolar echoes in spin 7/2 systems [35].

4.3.3 General Considerations of the Static Spectra

Using the determined optimum pulse length, static ^{133}Cs NMR spectra of Cs intercalated SWNT were recorded using a Hahn echo pulse sequence and subsequent Fourier transformation. Fig. 4.12 shows the static room temperature ^{133}Cs NMR spectra for Cs intercalated SWNT with different intercalation stoichiometries of CsC_x ($x = 8, 12, 30, 40$). Following the stoichiometry dependence, at low intercalation levels, only one single quadrupolar broadened line located at 0 ppm is present. Above a stoichiometry CsC_{40} , a second line located around 2700 ppm is showing up with increasing intensity depending on the Cs concentration. However, it is

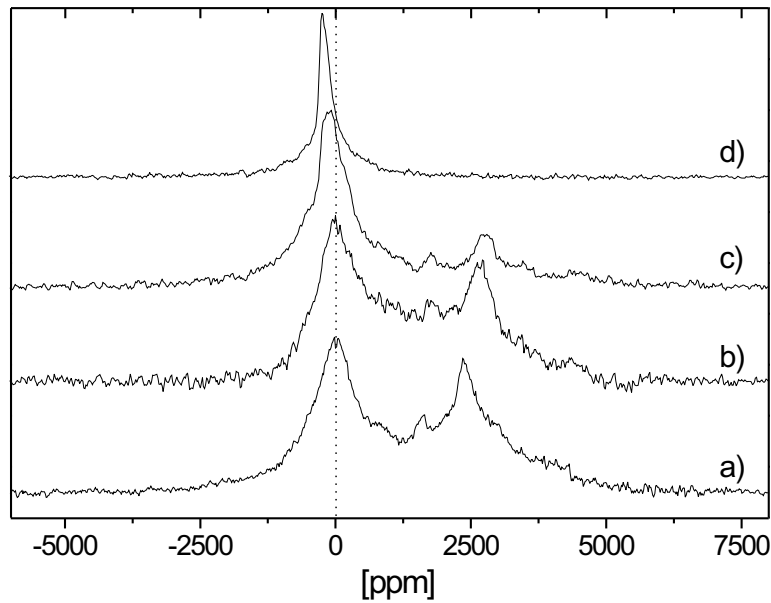


Figure 4.12: Room temperature ^{133}Cs NMR spectra of Cs intercalated SWNT with different intercalation stoichiometries of CsC_x with $x = 8$ (a), 12 (b), 30 (c) and 40 (d). The Larmor frequency was 50.7 MHz

difficult to judge if the 2700 ppm line is growing at the expense of the 0 ppm line since this could only be proven by in situ NMR measurements during Cs intercalation.

To simplify matters, in the following the 0 ppm line is labeled as α - and the 2700 ppm line as β -line. The presence of the two lines at high Cs concentrations suggests the existence of at least two inequivalent Cs α - and β adsorption sites in the SWNT bundle. It is again important to note, that possible Cs adsorption sites are only provided by the interstitial channels as well as on the surface of a carbon nanotube bundle. The interior space of the present SWNT is supposed to be predominantly inaccessible for penetration by Cs atoms since the used nanotubes are expected to have closed end caps.

The position of the α line around 0 ppm indicates the presence of almost fully ionized $\text{Cs}^{(\alpha)+}$ cations, whereas the strongly paramagnetically shifted β -line indicates the presence of $\text{Cs}^{(\beta)+}$ cations with $\beta < \alpha \approx +1$. The paramagnetic shift of the β -line can be interpreted as a Knight shift corresponding to a slightly metallic character of $\text{Cs}^{(\beta)+}$ ions located at β adsorption sites. The presence of pure metallic Cs in the present samples can be excluded, since the associated NMR line would be located around 14900 ppm [234].

4.3.4 α -Line FWHM

Fig. 4.13 shows the FWHM temperature dependence of the α -line at low intercalation levels of CsC_{31} , where a clear separation of the α - and β line is possible. At temperatures around 100 K the α -line exhibits a weak symmetrical quadrupolar powder pattern with the appropriate etches spaced by about 76 kHz (~ 1500 ppm) as is shown in Fig. 4.14. A corresponding quadrupolar coupling strength can be estimated to $\omega_Q^{(\alpha)} \sim 2\pi \cdot 150$ kHz.

Therefore it can be concluded that at low temperatures, the rigid-lattice linewidth is dominated by quadrupolar interactions. Around a temperature of $T \sim 150$ K, the linewidth is reduced with increasing temperature, which is typical for thermally activated motion behavior. However, motional narrowing is incomplete in the investigated temperature range.

In the presence of motional narrowing the linewidth $\delta\omega$ can be fitted using the relation (2.40)

$$\delta\omega^2 = \delta\omega_0'^2 + \delta\omega_0^2 \frac{2}{\pi} \arctan[\alpha\delta\omega\tau_c]. \quad (4.1)$$

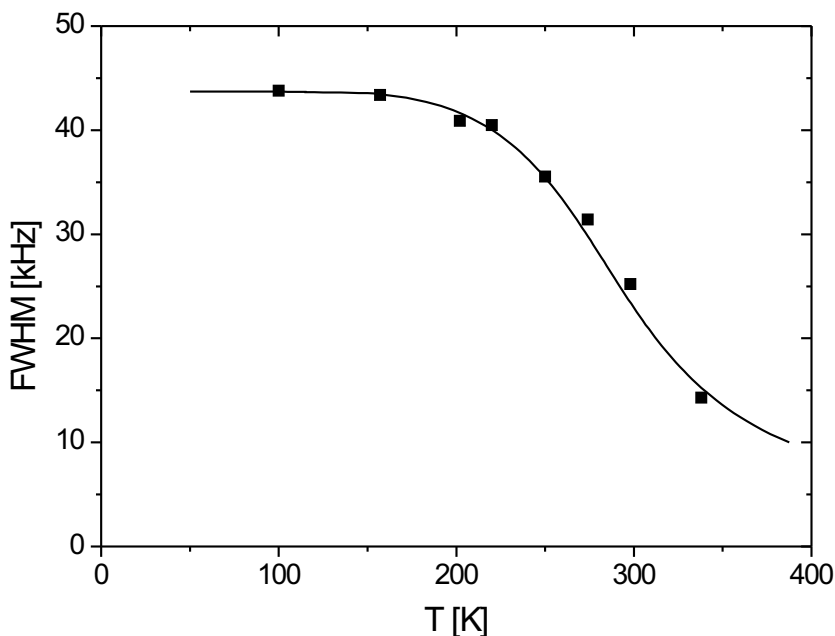


Figure 4.13: FWHM of the α -line as a function of temperature. The data was extracted from ^{133}Cs NMR spectra of CsC_{31} , which allows a clear separation of α - and β line. The solid line is a fit assuming a thermally motional narrowing process.

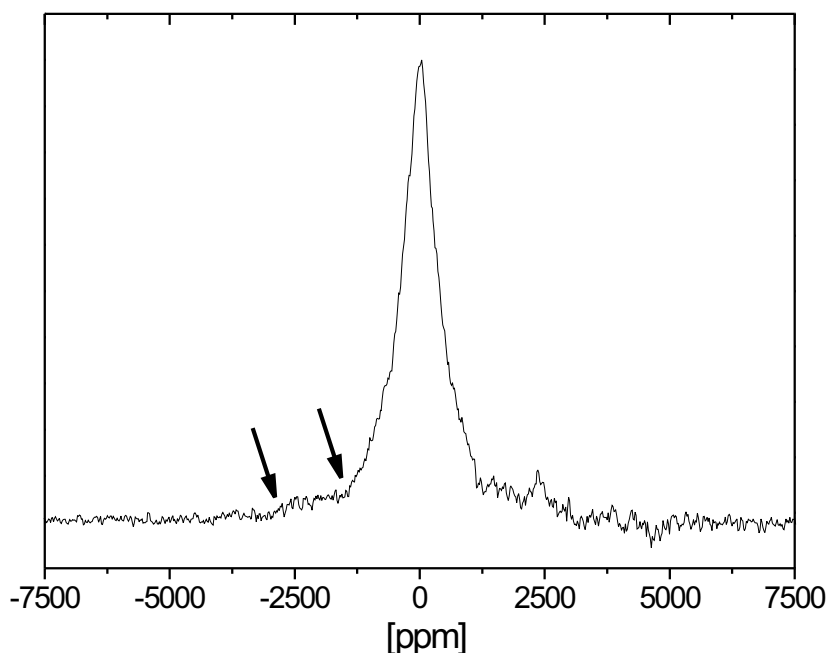


Figure 4.14: ^{133}Cs NMR spectrum of CsC_{31} at a temperature of $T = 100$ K. Clearly visible is the α -line at 0 ppm (\blacklozenge) and the paramagnetically shifted β -line (\bullet). In order to emphasize the quadrupolar line shape of the α -line, edges of the "Pake pattern" are indicated by arrows.

By assuming an Arrhenius behavior of the correlation time $\tau_c = \tau_0 \exp(E_A/k_B T)$ and setting $\alpha = 1$, the activation energy for the accompanying motional process can be roughly estimated to $E_{A1} = 0.1$ eV. The rigid lattice linewidth is about $\delta\omega_0 \sim 2\pi \cdot 44$ kHz and the linewidth at high temperatures can be calculated to be around $\delta\omega'_0 \sim 2\pi \cdot 3$ kHz.

For a rigid-lattice linewidth dominated by quadrupolar interactions, $\delta\omega_0$ is expected to be in the order of $\omega_Q^{(\alpha)} \sim 2\pi \cdot 150$ kHz. However, due to the weak pronounced quadrupolar line structure, analysis of the spectral FWHM was limited to the central transition. This explains the low value of $\delta\omega_0$.

As shown in Chap. (2.1.6), the second moment of a line and the corresponding spin-spin relaxation are sensitive to fluctuations in a comparable frequency range. Therefore, the changes in the α -line FWHM with increasing temperature should strongly effect the spin-spin relaxation behavior $1/T_2^\alpha$.

4.3.5 α -Line, $1/T_2^\alpha$ Relaxation Rate

Fig. 4.15 displays the spin-spin relaxation rate of the α -line $1/T_2^\alpha$ as a function of temperature. The measurements were performed on the sample CsC_{31} . At all temperatures, the relaxation followed an exponential decay composed of two components, which both reveal a very similar temperature dependence. Since Cs nuclei have a quadrupolar moment, their spectra consist of several spectral contributions. A multi-exponential spin-spin relaxation is therefore not surprising.

With rising temperature, $1/T_2^\alpha$ follows an exponential increase. In the previous paragraph, the temperature dependence of the FWHM showed an incomplete motional narrowing process in the investigated temperature range. Therefore, relaxation occurs in the rigid lattice limit, where the general weak collision theory is not valid any more (see Chap. 2.2.4).

The spin-spin relaxation rate for strong collision is given by Eq. (2.64):

$$\begin{aligned} \frac{1}{T_2} &= \frac{1}{T_2'} + \frac{2(1-p)}{\tau_{sc}}, \\ \frac{1}{\tau_{sc}} &= \frac{N_v}{N\tau_v} \quad \text{with} \\ \frac{1}{\tau_v} &= \frac{1}{\tau_0} \exp\left(\frac{E_{A1}}{k_B T}\right). \end{aligned} \tag{4.2}$$

The factor N_v/N describes the vacancy concentration, and p is a numerical quantity that depends on the type of motion and the spatial distribution of diffusion vacancies. In the following, p will be set to zero.

The correlation time at infinite temperature is assumed to $\tau_0 \sim 10^{-12}$ s. By using the activation energy of $E_{A1} \sim 0.1$ eV obtained from the linewidth fit in Fig. 4.13 and applying it to Eq. (4.2), the run of $1/T_2^{(\alpha)}$ in Fig. 4.15 can be directly fitted (solid line).

The ground relaxation rate $1/T_2'$ which contains contributions from all other spin-spin relaxation mechanisms can be estimated to be $1/T_2' \sim 575 \text{ s}^{-1}$ and the vacancy concentration accounts to $N_v/N \sim 1.3 \cdot 10^{-7}$.

Even though, this vacancy concentration is unreasonable low, the fit of the exponential increase of $1/T_2$ confirms that both, ^{133}Cs NMR linewidth and $1/T_2$ relaxation behavior of the α line can be properly described by a thermally activated slow-motion diffusion process of the α -line $\text{Cs}^{(\alpha)+}$ ions with an activation energy of $E_{A1} \sim 0.1$ eV.

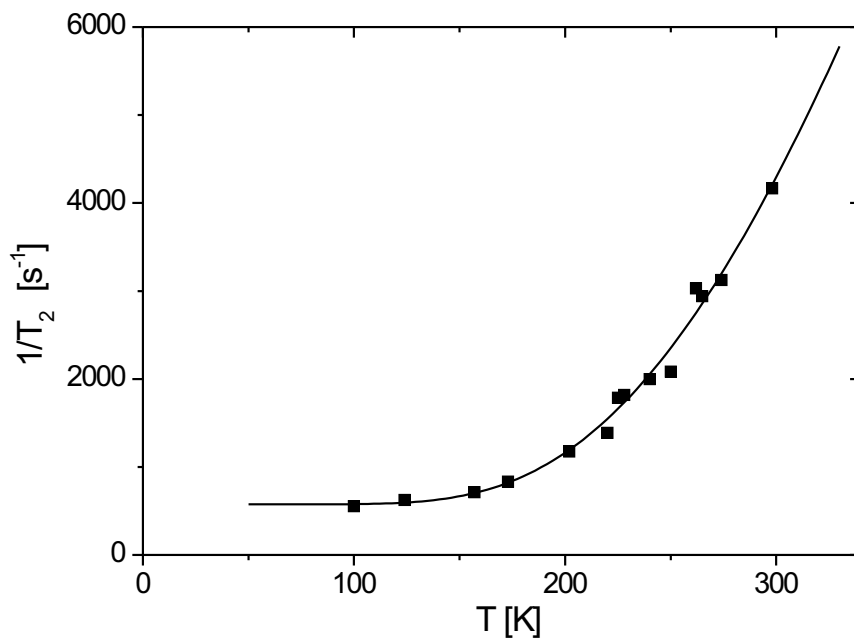


Figure 4.15: Spin-spin relaxation rate of the α -line $1/T_2^\alpha$ as a function of temperature (CsC_{31}). The solid line is a fit using a slow motion relaxation process in the strong collision regime.

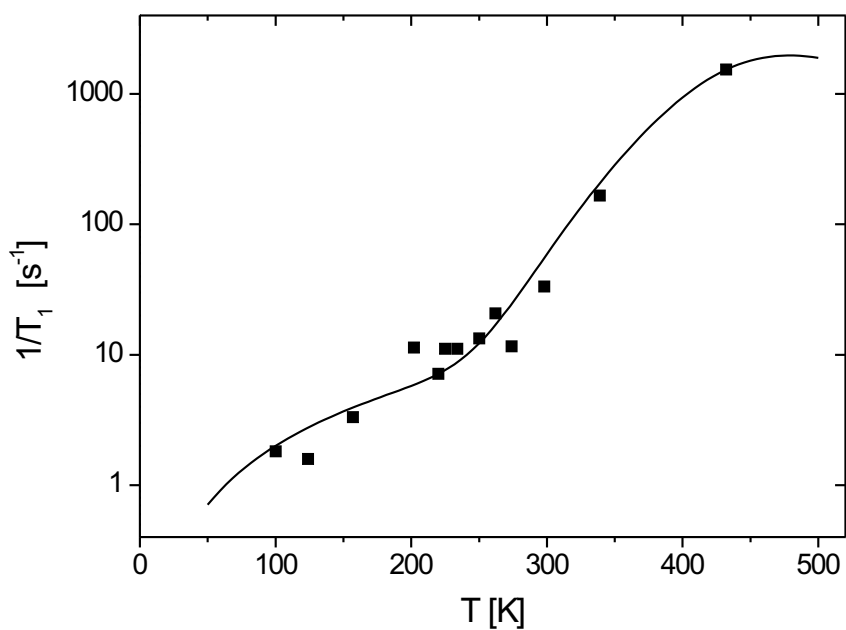


Figure 4.16: Temperature dependence of the α -line spin-lattice relaxation rate $1/T_1^\alpha$ (CsC_{31}). The solid line is a fit assuming a Korringa- and a BPP-type relaxation process.

4.3.6 α -Line, $1/T_1^\alpha$ Relaxation Rate

Fig. 4.16 shows the α -line spin-lattice relaxation rate $1/T_1^\alpha$ versus temperature. At all temperatures, the spin-lattice relaxation follows a biexponential magnetization recovery curve after saturation.

This can be explained by the property of a multi-level spin system of the Cs quadrupolar nuclei. Upon non-selective excitation of the spin system, a multi-exponential relaxation between the different energy levels is always expected [36, 37].

Since both relaxation components show a comparable temperature dependence of $1/T_1^\alpha$, again the best fit of the relaxation behavior as a function of temperature is chosen.

The spin-lattice relaxation in Fig. 4.16 follows an exponential increase extending over three orders of magnitude. It is only possible to fit these data using a combination of two independent relaxation processes,

$$\frac{1}{T_1} = \frac{1}{T_1^{(1)}} + \frac{1}{T_1^{(2)}}. \quad (4.3)$$

- The exponential increase in Fig. 4.16 suggests a relaxation process due to thermally activated dynamics. Since at all temperatures, $\omega_0\tau_c \gg 1$, the spin-lattice relaxation can be treated in the weak-collision regime. In order to fit the data, it is assumed that the spin-lattice relaxation is mainly quadrupolar since Cs nuclei have a large quadrupolar moment. $1/T_1$ for Cs nuclei with spin 7/2 is given by (see Chap. 2.2.3)

$$\begin{aligned} \frac{1}{T_1^{(1)}} &= \frac{2}{5}\omega_Q^2 [J(\omega_0) + 4J(2\omega_0)] && \text{with} \\ J(\omega_0) &= \frac{\tau_c}{1 + \omega_0^2\tau_c^2} && \text{and} \\ \tau_c(T) &= \tau_0 \exp\left(\frac{E_{A2}}{k_B T}\right). \end{aligned} \quad (4.4)$$

- The presence of delocalized electrons on the SWNT suggests a weak orbital overlap with the Cs^(α) nuclei which causes a hyperfine relaxation process

$$\frac{1}{T_1^{(2)}} = mT^\kappa. \quad (4.5)$$

The exponent κ takes a mixture of various hyperfine coupling contributions into account.

Assuming a correlation time at infinite temperature of $\tau_0 \sim 10^{-12}$ s, the spin-lattice relaxation $1/T_1$ can be fitted with an activation energy of $E_{A2} \sim 0.29$ eV and a quadrupolar coupling strength of about $\omega_Q \sim 2\pi \cdot 166$ kHz for the thermally activated relaxation process. The slope for the linear Korringa relaxation process is given by $m = 0.002 \text{ s}^{-1}$ with $\kappa = 1.5$. The fit of $1/T_1^\alpha$ is shown as a solid line in Fig. 4.16.

The quadrupolar coupling strength is comparable with $\omega_Q^{(\alpha)} \sim 2\pi \cdot 150$ kHz obtained from analysis of the α -line spectrum at low temperatures.

The intercalation of Cs alkali metal in the bundles of SWNT was proven by X-ray diffraction measurements [111]. A diffusion of Cs ions in the SWNT bundles should be geometrically restricted to a diffusion parallel and perpendicular to the carbon nanotubes. This suggests, that the higher activation energy $E_{A2} \sim 0.29$ eV of the weak-collision relaxation process corresponds to inter-channel diffusion perpendicular to the SWNT bundle, whereas the lower activation energy $E_{A1} \sim 0.1$ eV of the slow-motion relaxation process corresponds to diffusion along the interstitial channels of the SWNT bundle.

A diffusion perpendicular to the SWNT bundle is highly supposable since the large value of $\omega_Q \sim 2\pi \cdot 166$ kHz indicates drastic changes in the local EFG which is expected for an inter-channel movement of the $\text{Cs}^{(\alpha)+}$ ions. The motion process along the SWNT bundle channels is slow because of a low Cs vacancy concentration along the interstitial channels of the SWNT bundle.

Since the relaxation measurements were performed on the low intercalated sample CsC_{31} , a scenario of weakly hindered Cs diffusion is very likely. However, for higher Cs stoichiometries α -line nuclei diffusion is expected to be strongly hindered. A kind of reduced $\text{Cs}^{(\alpha)+}$ mobility with increasing intercalation level is suggested by the increasing α -line broadening at higher Cs intercalation levels (Fig. 4.12).

A comparable Cs diffusion process was reported for Cs intercalation and diffusion in between adjacent nanotube shells of MWNT [136]. The observed diffusion constant was extremely small compared to Cs diffusion in between adjacent graphene sheets of Cs-GIC. The authors attributed this to the presence of defective MWNT or even to a characteristic of the nanometer scale tubular structures.

4.3.7 β -Line, Spectral Analysis

Fig. 4.17 presents the ^{133}Cs NMR spectrum of CsC_8 at a temperature of $T = 40$ K. The spectrum shows a complex composition of the α - and β -line spectrum with quadrupolar powder pattern lineshapes as well as at least two other additional lines around 1050 ppm and 4450 ppm.

The quadrupolar lineshape of the β -line is well pronounced and will be used in the following to determine the $\text{Cs}^{(\beta)+}$ quadrupolar lineshape parameters.

In order to properly extract both, the β -line quadrupolar coupling constant ω_Q^β as well as the asymmetry parameter η^β , a symmetric β -lineshape was generated by mirroring the paramagnetic part of the spectrum with respect to the maximum of the β -line position.

Fig. 4.18 shows the symmetrized ^{133}Cs NMR β -line of CsC_8 taken at a temperature of $T = 133$ K. The quadrupolar structure can be fitted with a quadrupolar coupling

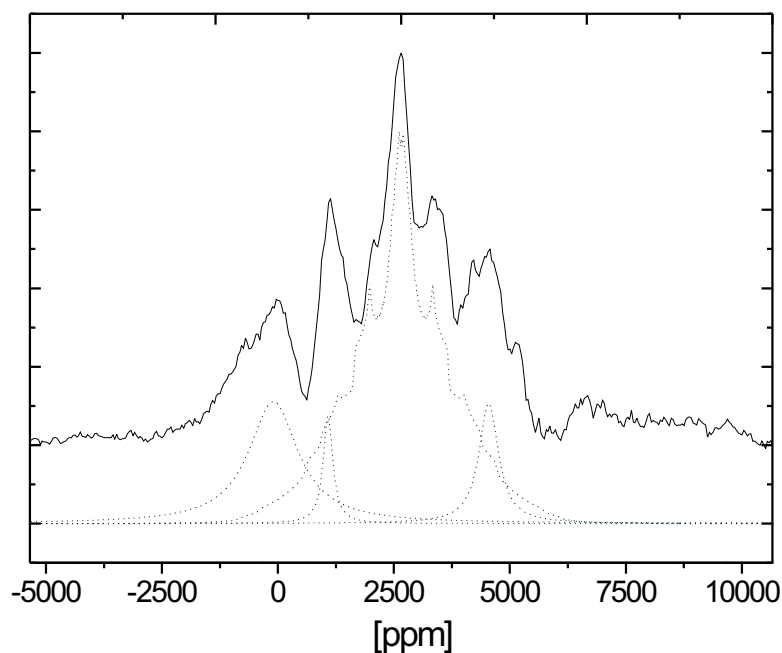


Figure 4.17: ^{133}Cs NMR spectrum of CsC_8 at a temperature of $T = 40$ K and a Larmor frequency of 50.7 MHz. The α -line at 0 ppm is marked by a (\blacklozenge), whereas the paramagnetically shifted β -line is marked by a (\bullet). The dotted lines are fits using a Lorentzian α -line, a quadrupolar powder pattern lineshape for the β -line as well as two additional Lorentzian lines located around 1050 ppm and 4450 ppm. More detailed explanations of these fits are given in the text.

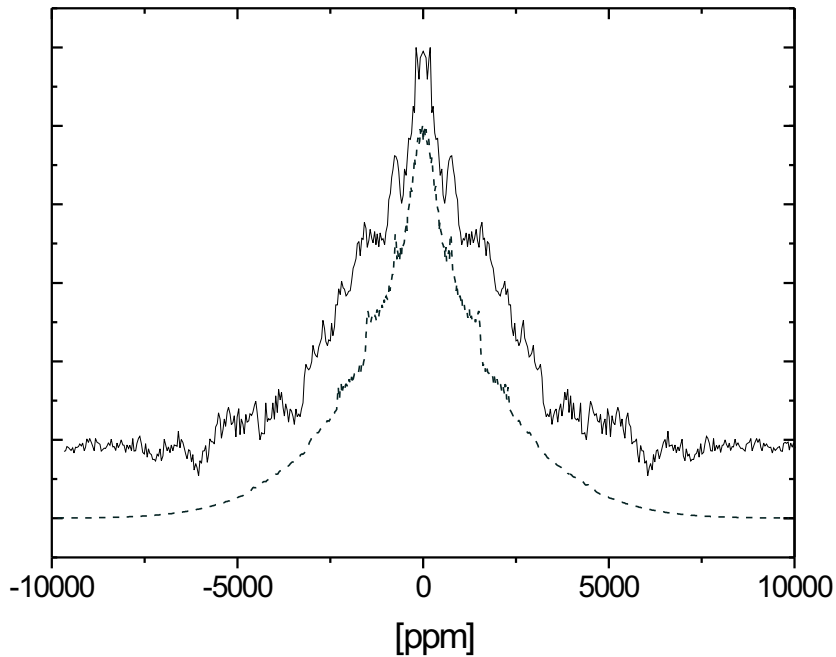


Figure 4.18: Symmetrized β -line ^{133}Cs NMR spectrum of CsC_8 at a temperature of $T = 130$ K and a Larmor frequency of 50.7 MHz. Symmetrization was performed by mirroring the paramagnetic part of the spectrum with respect to the maximum of the β -line position. The dashed lines are a fit assuming a vertically shifted quadrupolar powder pattern lineshape.

constant of about $\omega_Q^\beta \sim 2\pi \cdot 100$ kHz and an asymmetry-parameter of $\eta^\beta \sim 0.3$. In order to fit the complete spectrum in Fig. 4.17, around 0 ppm a Lorentzian α -line was used which is sufficient since its quadrupolar powder pattern is only weakly pronounced. Besides the quadrupolar β -line powder pattern (with the given β -line fit parameters), it is necessary to additionally include two strongly paramagnetically shifted Lorentzian lines located around 1050 ppm and 4450 ppm. The origin of these two additional lines is unknown. However, they indicate the presence of further Cs adsorption sites or further different structural Cs arrangements in the sample.

The temperature dependence of the β -line second moment M_2 is shown in Fig. 4.19. With increasing temperature, M_2 of the β -line is weakly reduced which indicates a slightly thermally activated dynamical behavior of the $\text{Cs}^{(\beta)+}$ ions.

Concurrently the quadrupolar β -line structure is still observable up to temperatures of 460 K. This corresponds to only a weak temperature dependence of the electric field gradient (EFG) at the site of the Cs nuclei.

Both observations can be explained with a highly structural molecular Cs order (Cs

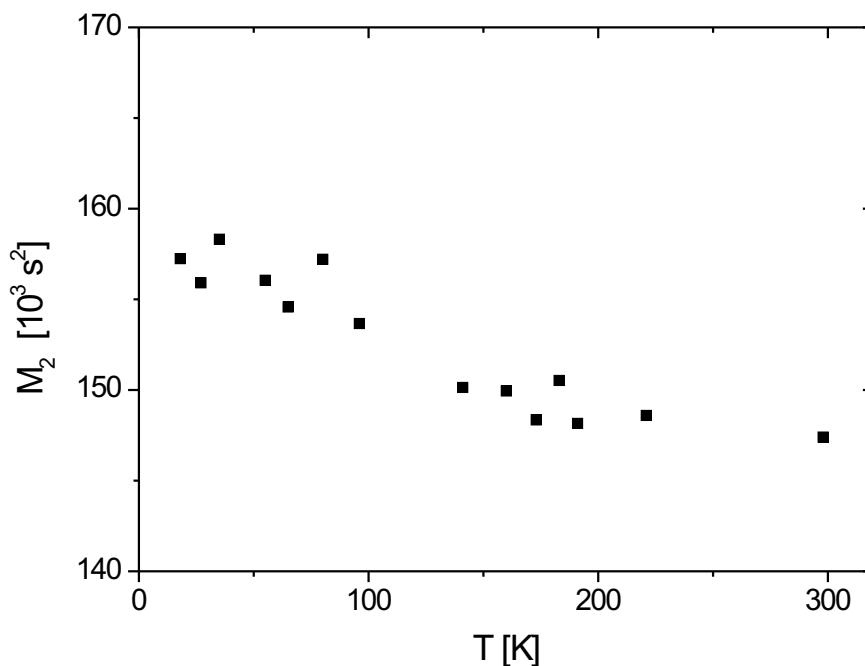


Figure 4.19: The ^{133}Cs NMR second moment M_2 of the β -line in CsC_8 as a function of temperature.

lattice). Possibly the Cs ions occupy well defined atom positions relative to the carbon lattice (e.g. above the centers of the C hexagons). A thermally activated Cs mobility with hopping or diffusion from one site to the other will reduce the linewidth, while the EFG is preserved.

Since spin relaxation is sensitive to molecular dynamics, various ^{133}Cs NMR relaxation measurements on the β -line were carried out.

4.3.8 β -Line, $1/T_1^\beta$ Relaxation Rate

Fig. 4.20 displays the CsC_8 β -line spin-lattice relaxation rate $1/T_1^\beta$ as a function of temperature. The relaxation after saturation follows a biexponential magnetization recovery at all temperatures, as expected for quadrupolar nuclei upon non-selective spectral excitation. One relaxation component is shown in Fig. 4.20. In the investigated temperature range, the spin-lattice relaxation exhibits a linear increase with rising temperature. The linear relaxation behavior suggests a strong hyperfine coupling between Cs nuclei and conduction electrons on the carbon nanotubes. Linear fitting of the data using a hyperfine relaxation process yields $1/T_1 T = 0.53 \text{ s}^{-1}\text{K}^{-1}$.

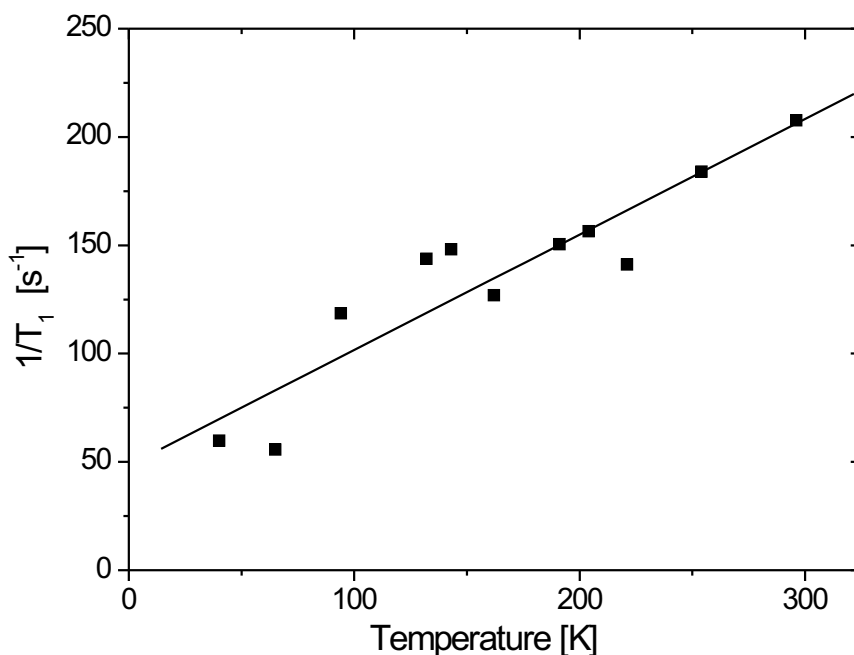


Figure 4.20: Spin-lattice relaxation rate of the β -line $1/T_1^\beta$ as a function of temperature (CsC_8). The solid line is a fit using a hyperfine mediated Korringa relaxation process.

The classical Korringa relation Eq. 2.42 defined in Chap. (2.2.1) correlates isotropic hyperfine mediated spin-lattice relaxation with the corresponding Knight shift:

$$T_1 T K_{iso}^2 = \frac{\hbar}{4\pi k_B} \left(\frac{\gamma_e}{\gamma_n} \right)^2. \quad (4.6)$$

This relation can be used to estimate a Knight shift corresponding to the $1/T_1^{(\beta)}$ relaxation behavior in Fig. 4.20. The motivation to use pure isotropic hyperfine interaction arises from the strong s -character of the involved $\text{Cs}(6s)$ -orbitals, which causes the Fermi-contact like electron-nuclear interaction. By applying Eq. 4.6 to the slope of $1/T_1^\beta$ in Fig. 4.20, the corresponding Knight shift can be calculated to $K_{iso} = 2850$ ppm.

This value is on the order of the observed high temperature β -line Knight shift values (~ 2800 ppm) and thereby confirms the hyperfine coupling as the main origin of the observed β line shifts.

In order to establish isotropic hyperfine interactions, the electron probability density at the Cs nuclei must be non-zero. This suggests a limited charge transfer from Cs to SWNT. In order to estimate the residual amount of charge on the Cs ions, K_{iso} can be compared with the Knight shift of pure Cs metals (~ 14900 ppm). Since the

ratio K_{iso}/K_{metal} is proportional to $|\psi(0)|^2$, roughly a spin density on the Cs nuclei of 20% can be calculated which corresponds to a partial charge transfer.

The charge transfer limitation can be explained by a Cs(6s) - C(2p) hybridization. The result of a charge transfer limitation upon hybridization is compatible with results obtained from first principle calculations [131,142]. Lu et. al [142] theoretically found a charge transfer limitation in potassium intercalated nanotubes. Above a stoichiometry of KC_{27} , the authors claim a preferential C-K hybridization with increasing K intercalation level due to a coupling of the nanotube nearly free electron states (NFE) [151] with the K(4s) orbital, leading to a limitation of the charge transfer. In KC_8 , the amount of transferred charge is calculated to be around 60%, a value that is expected to decrease for Cs intercalation upon its higher hybridization affinity.

4.3.9 β -Line, $1/T_2^{(\beta)}$ Relaxation Rate

The limited electron charge transfer and Cs(6s) - C(2p) hybridization discussed in the previous section correspond to a non vanishing probability density at the position of the Cs nucleus. In addition, the carbon nanotubes behave like a metallic system with delocalized conduction electrons (see Chap. 3.2.2). As a whole, hybridization and delocalized electrons correspond to localized electron states near the Fermi level. The hyperfine interaction of the electron system with the Cs nuclei usually causes Korringa relaxation with very high electron correlation rates which make this kind of relaxation only observable in the spin-lattice relaxation of the nuclear spin system. Contrary to spin-lattice relaxation, spin-spin relaxation is sensitive to slow spin fluctuations.

Fig. 4.21 shows the ^{133}Cs β -line spin-spin relaxation rate $1/T_2^{(\beta)}$ as a function of temperature. Above a temperature of $T = 50$ K, $1/T_2^{(\beta)}$ follows a linear increase with increasing temperature. Below $T = 50$ K, an exponential increase of the spin-spin relaxation rate with decreasing temperature is observable.

The exponential increase at low temperatures is a signature for relaxation due to scalar electron-nuclear coupling with slow electron fluctuations (with low electron correlation rates). The temperature dependence of this type of spin-spin relaxation was discussed in Chap. (2.2.2) and $1/T_2$ is given by

$$\frac{1}{T_2^{(\beta)}} = \frac{A^2}{4} \tau_{1e}. \quad (4.7)$$

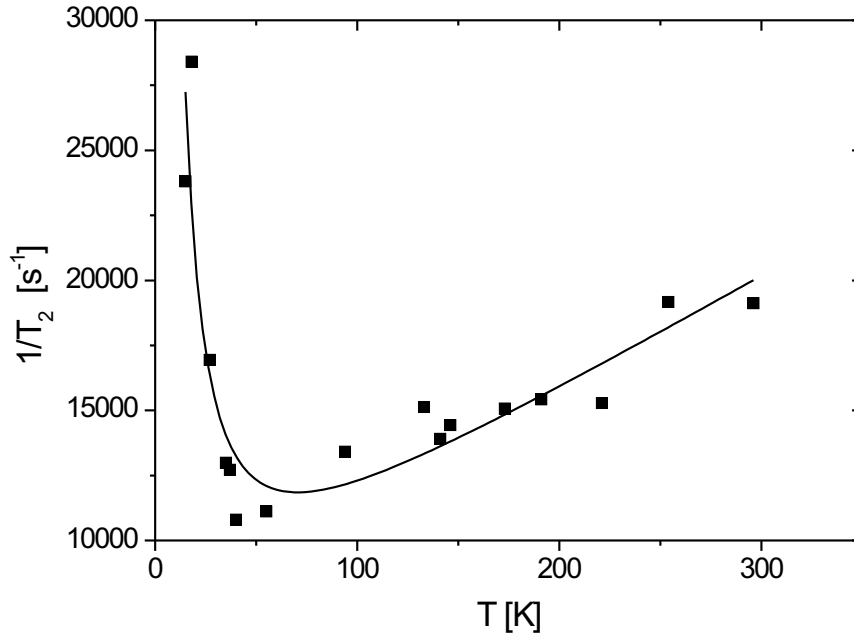


Figure 4.21: Temperature dependence of the ^{133}Cs NMR spin-spin relaxation rate $1/T_2$ for the β -line. The solid line represents a fit assuming a relaxation caused by scalar electron-nuclear coupling, a linear term of unknown source and a constant background relaxation rate.

The electron spin-lattice relaxation behavior is described by [38]

$$\frac{1}{\tau_{1e}} = \frac{1}{\tau_{c0}} \left(\frac{T}{T_0} \right)^\kappa. \quad (4.8)$$

The temperature T_0 can be arbitrarily set to 1 K. Therefore $1/\tau_{c0}$ corresponds to the relaxation rate at $T = 1$ K. The exponent κ includes several additive relaxation mechanisms. One common exponent κ is chosen since it is rather difficult to separately analyze electron spin-lattice relaxations due to direct, Orbach and Raman relaxation processes.

In order to completely describe the temperature dependence of $1/T_2^{(\beta)}$ over the full temperature range, besides a relaxation caused by scalar-nuclear coupling another unknown relaxation mechanism $1/T_1 = m_1T + d_1$ dominating at higher temperatures has to be assumed (m_1 is the slope of a linear relaxation rate increase and d_1 is a constant offset attributed to some background relaxation mechanisms):

$$\begin{aligned} \frac{1}{T_2^{(\beta)}} &= \frac{A_1^2}{4} \tau_{c01} \left(\frac{T}{T_0} \right)^{-\kappa_1} + m_1T + d_1 \\ &\equiv \frac{C}{4} \left(\frac{T}{T_0} \right)^{-\kappa_1} + m_1T + d_1. \end{aligned} \quad (4.9)$$

The fit represented by a solid line in Fig. 4.21 follows the fit parameters $\kappa_1 = 1.43$, a spin-spin coupling strength of $C = A_1^2 \tau_{c01} = 3.8 \cdot 10^6 \text{ s}^{-1}$, a slope $m_1 = 44.6 \text{ K}^{-1} \text{ s}^{-1}$ describing the linear dependence of $1/T_2^{(\beta)}$ above 50 K and a constant offset of $d_1 = 6500 \text{ s}^{-1}$.

In order to estimate the prefactor τ_{c01} , stimulated echo relaxation experiments were carried out. The motivation arises from a comparable sensitivity of $1/T_2$ and $1/T_1^{stim}$ to slow spin fluctuations (see Chap. 2.2.5). The difference though is that $1/T_2$ describes transversal relaxation in the rotating frame, whereas $1/T_1^{stim}$ describes longitudinal relaxation in the rotating frame.

4.3.10 β -Line, Stimulated Echo Relaxation

^{133}Cs stimulated echo relaxation experiments on the β -line (presented in Fig. 4.22) exhibit a relaxation behavior for $1/T_1^{stim}$ comparable to the run of $1/T_2$ in Fig. 4.21. A linear increase of the stimulated echo relaxation rate with increasing temperature is observable above a temperature of $T = 125 \text{ K}$ as is shown in Fig. 4.22. Below $T = 125 \text{ K}$ the spin-lattice relaxation rate $1/T_1^{stim}$ follows an exponential increase with decreasing temperature.

Since both, $1/T_2^{(\beta)}$ and $1/T_1^{stim}$ probe relaxation of the spin-system due to slow spin fluctuations, the same source of is assumed for both, $1/T_1^{stim}$ and $1/T_2^{(\beta)}$.

The scalar spin-lattice relaxation rate $1/T_1$ is given by Eq. (2.51):

$$\frac{1}{T_1} = \frac{2A^2}{3} S(S+1) \left[\frac{\tau_{1e}}{1 + \omega_I^2 \tau_{1e}^2} \right]. \quad (4.10)$$

This equation can also be used to describe spin-lattice relaxation $1/T_1^{stim}$ in the rotating frame.

Using the above defined relaxation due to scalar electron-nuclear coupling, as well as an additional linear relaxation term $\sim m_2 T$ and a constant offset d_2 , the relaxation behavior in Fig. 4.22 can be fitted by

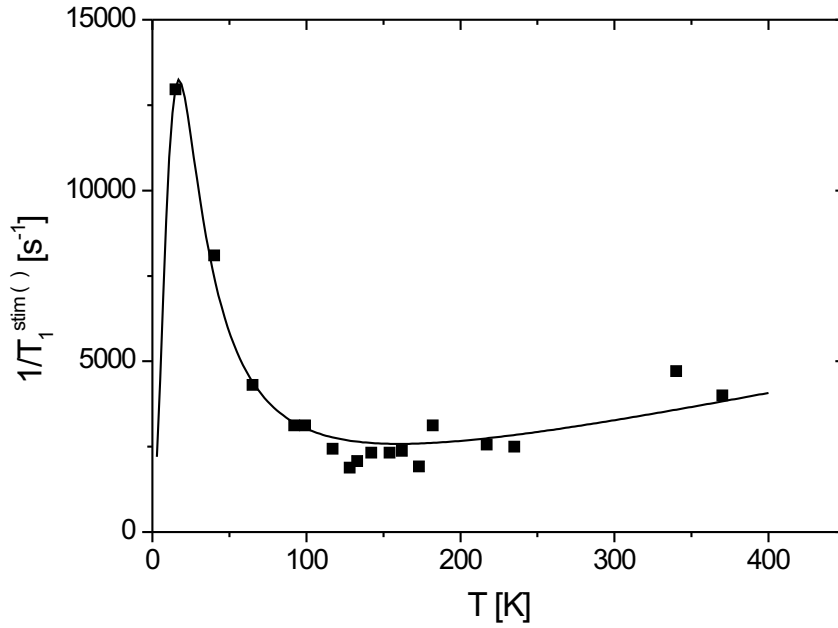


Figure 4.22: Temperature dependence of the ^{133}Cs NMR spin-lattice relaxation rate $1/T_1^{stim}$ for the β -line, obtained from stimulated echo experiments. The solid line represents a fit assuming a scalar electron-nuclear coupling, a linear term of unknown source and a constant background relaxation rate.

$$\begin{aligned} \frac{1}{T_1} &= \frac{A_2^2}{3} \left[\frac{\tau_{1e}}{1 + \omega_I^2 \tau_{1e}^2} \right] + m_2 T + d_2 \quad \text{with} \\ \frac{1}{\tau_{1e}} &= \frac{1}{\tau_{c02}} \left(\frac{T}{T_0} \right)^{\kappa_2}. \end{aligned} \quad (4.11)$$

Since both, $1/T_1^{stim}$ and $1/T_2^{(\beta)}$ are subject to the same relaxation mechanism, τ_{c0} and κ are set to $\tau_{c0} = \tau_{c01} = \tau_{c02}$ and $\kappa = \kappa_1 = \kappa_2$. Solving Eq. (4.9) for τ_{c01} and inserting into in Eq. (4.11) yields

$$\frac{1}{T_1} = \frac{A_1^2 A_2^2 C \left(\frac{T}{T_0} \right)^{-\kappa}}{A_1^4 + 16 \omega_I^2 C^2 \left(\frac{T}{T_0} \right)^{-2\kappa}} + m_2 T + d_2. \quad (4.12)$$

Fitting the stimulated echo $1/T_1^{stim}$ data in Fig. 4.22 results in spin-spin couplings $A_2 = 2\pi \cdot 9.1 \times 10^5 \text{ s}^{-1}$ and $A_1 = 2\pi \cdot 7.5 \times 10^5 \text{ s}^{-1}$ as well as the fit parameters $m_2 = 20 \text{ K}^{-1}\text{s}^{-1}$ and $d_2 = 100 \text{ s}^{-1}$. Finally, the relaxation rate at $T = 1 \text{ K}$ can be calculated to $1/\tau_{c0} = 5.7 \cdot 10^6 \text{ s}^{-1}$.

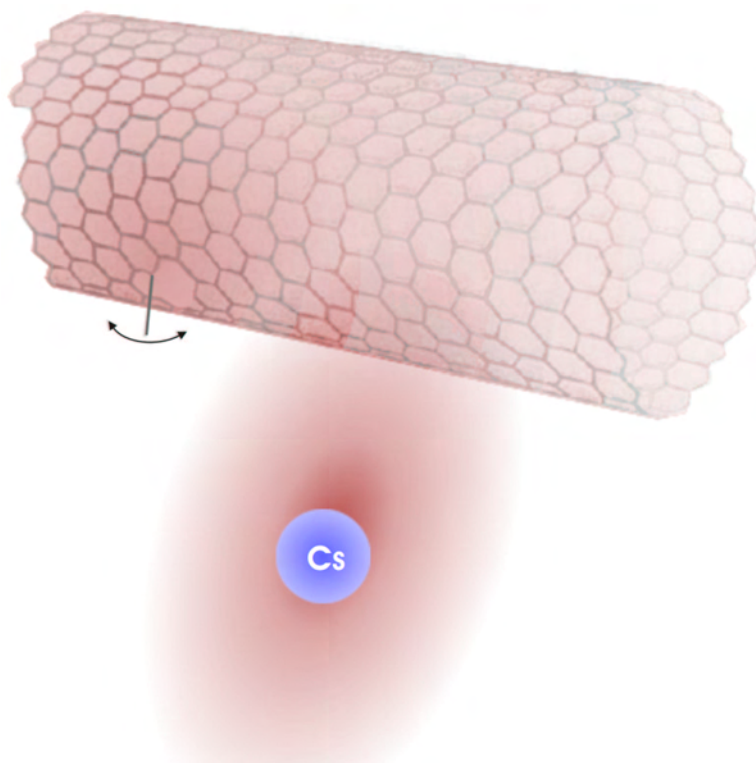


Figure 4.23: Scalar spin-spin coupling between a dangling bond (left) and a Cs atom (right). Spin fluctuations due to defects mediate a fluctuation of the electron states near the Cs atom. The red colored shading represents delocalized electrons on the carbon nanotube as well as electrons in the Cs-C hybridization.

It is important to note, that only for isotropic scalar coupling, A_1 should exactly equal A_2 , which is roughly the case. However, if the two constants would have differed by a larger factor, a relaxation contribution due to anisotropic coupling tensor components would have to be taken additionally into account.

In the following, the source of the observed isotropic scalar electron-nuclear spin coupling is discussed:

The model which is favored here considers thermally assisted fluctuations of unpaired electron spins due to dangling bonds and other defects on a carbon nanotube surface, as illustrated in Fig. 4.23. The presence of dangling bonds on carbon nanotubes is highly supposable, since it is well known that due to the high temperature production process of SWNT many atomic defects in the regular hexagonal carbon structure are induced [217–219].

As derived from ^{133}Cs β -line spin-lattice relaxation measurements, an overlap of the $\text{Cs}(6s)$ and $\text{C}(2p)$ orbitals describes the environment of the β -site Cs nuclei. Fluctuations of electron spins located at a defect couple through the SWNT conduction electrons to the localized electron distribution of the Cs-C hybridization. This corresponds to the observed spin-spin relaxation and stimulated echo decay behavior. This model is supported by the rather small coupling constant of $A_i \sim 2\pi \cdot 1 \times 10^6 \text{ s}^{-1}$. Correspondingly, the distance between the dangling bond and the Cs atom can be on the order of several Å (up to 10-20 Å).

4.3.11 Temperature Dependence of α - and β -Line Shifts

Fig. 4.24 shows the temperature dependence of the α and β line positions. Both α and β line shifts vary by more than 700 ppm in the investigated temperature range. The complex line shift behaviors have to be attributed to a temperature dependence of either the Knight shift or the chemical shift.

Even though, α and β line shifts are not expected to exhibit the same origin, possible sources for Knight- and chemical shift of both lines are jointly discussed here:

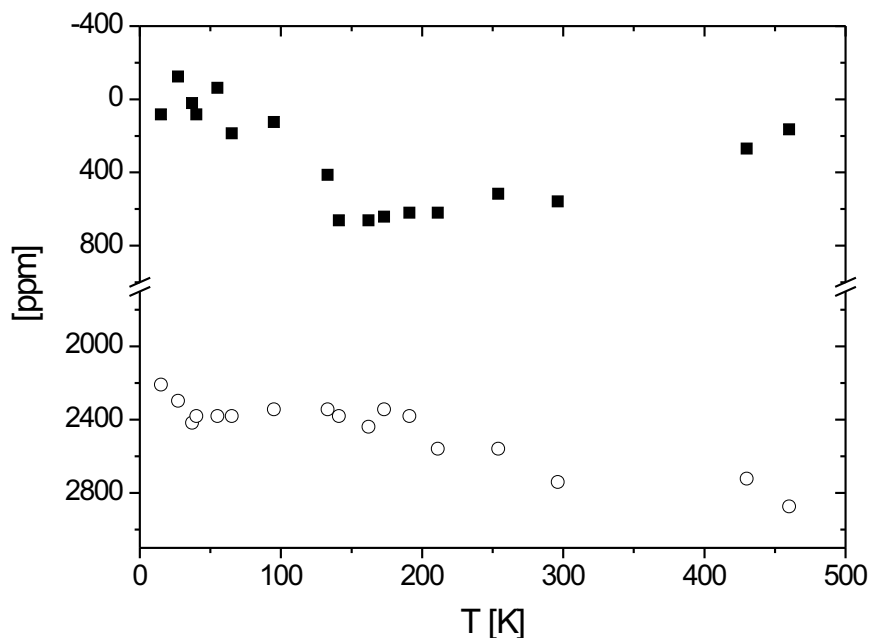


Figure 4.24: Temperature dependence of the α (■) and β (○) line positions extracted from ^{133}Cs NMR spectra (CsC_8).

- **Knight Shift**

The classical Knight shift in metals is given by

$$K = \frac{8}{3}\pi\chi_s \langle |\psi(0)|^2 \rangle = \frac{a_{iso}}{\gamma_n \gamma_e \hbar} \chi_s \quad (4.13)$$

with $\langle |\psi(0)|^2 \rangle$ being the average probability density at the nucleus for all electronic states on the Fermi surface and a_{iso} the isotropic hyperfine coupling constant (see Chap. 2.1.4). Therefore, a temperature dependence of the Knight shift could originate from a temperature dependence of either χ or $\langle |\psi(0)|^2 \rangle$ (or a_{iso}). The spin susceptibility $\langle |\psi(0)|^2 \rangle$ are known to be sensitive to thermal lattice expansions in metallic Cs, where the Cs atoms are densely packed in a bcc-crystal structure [235]. A temperature dependence of a_{iso} was reported for Rb_3C_{60} [102].

In order to draw a simple picture for the Cs arrangement upon intercalation, structural simulations were performed. The carbon nanotube bundle was treated as a fixed triangular lattice of charged cylinders and van-der-Waals and electrostatic interactions were taken into account. For high levels of intercalation the Cs ions appear in a dense packed matter enwrapping the individual nanotubes as illustrated in Fig. 4.25. Probably this structure reflects best the Cs ion arrangement attributed to the β -line. Comparable to thermal lattice expansion in metallic Cs it is imaginable, that a temperature dependent Cs ion lattice expansion upon concurrent retaining of the structural order induces the changes in χ or $\langle |\psi(0)|^2 \rangle$ (or a_{iso}) and therewith a change in K .

In Cs-GIC comparable line shifts were interpreted as a Knight shift variation arising from a reverse electron transfer from the graphitic host back to the Cs nuclei [98]. The authors assumed that in case the Cs nuclei occupy well defined atom positions relative to the carbon lattice, a thermally induced deregistration between Cs and the carbon lattice could be associated with a partial relocalization of the electrons in the s -function.

However, such a relocalization should be rather unlikely. In case of Cs diffusion a breaking up of the Cs-C hybridization and consequently the formation of completely ionized Cs^+ ions is expected rather than an opposite partial electron transfer to the Cs nuclei.

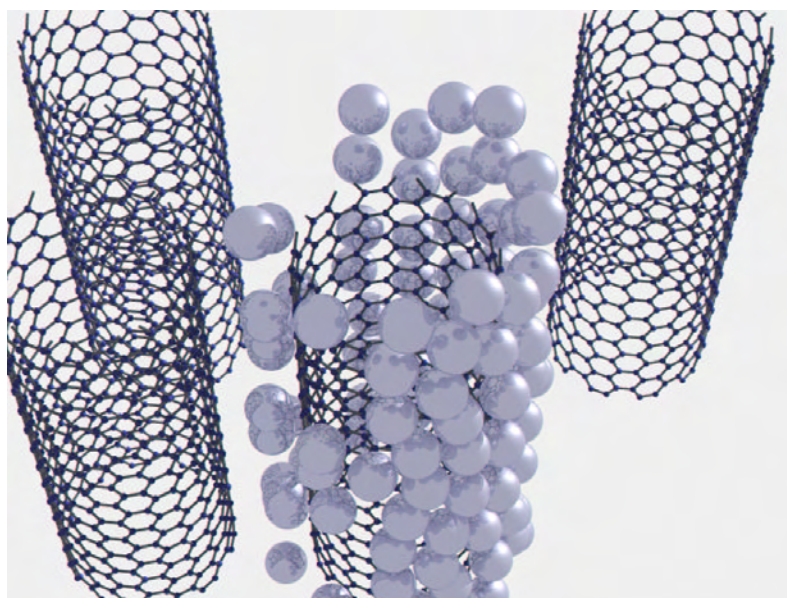


Figure 4.25: Simulation of the structural configuration of Cs-SWNT CsC₈. For clearness only four SWNT forming the triangular nanotube bundle lattice as well as a few Cs ions are shown. The Cs ions cover the nanotubes completely.

- **Chemical Shift**

Chemical shifts of alkali metal compounds are usually substantially smaller than appropriate Knight shifts (<1000 ppm) [4,97]. Even though, they may play an important role in the temperature dependence of the observed Cs line shifts, since structural Cs rearrangements in the system are supposed to drastically change the orbital overlap of neighboring Cs atoms and therefore effect the chemical shifts.

In case of the α -line, due the absence of strong hyperfine couplings, the shift is highly probable a pure chemical shift, whereas for the β -line a combination of Knight- and chemical shifts is conceivable. A quantitative evaluation of the temperature dependence of the α - and β -line can unfortunately not be given.

4.3.12 Comparison with ^{133}Cs NMR of Cs-GIC

Remarkable is the similarity of the ^{133}Cs NMR spectra in Fig. 4.12 with spectra obtained from Cs graphite intercalation compounds (GIC). In the following the present results on intercalated SWNT are compared with measurements on stage I GIC and higher stages ($>I$) GIC [31,97,98].

Stage I Cs-GIC

At room temperature, for pure stage I Cs-GIC (CsC_8) a single NMR line was observed at 2500 ppm. Additionally, at low temperatures, the presence of a quadrupolar line-shape with $\omega_Q \sim 2\pi \cdot 74$ kHz was demonstrated [96,97]. These values of line shift and quadrupolar couplings are comparable to the shift and couplings of the β -line in the Cs intercalated SWNT samples.

However, the temperature dependence of the line shifts in GIC and SWNT are different. In Cs-GIC, with decreasing temperature from 500 K to 300 K the line shifts linearly from 2900 ppm to 2400 ppm, whereas the β -line reaches the 2400 ppm value not until below a temperature of 200 K.

For stage I Cs-GIC, a ^{133}Cs NMR spin-lattice relaxation time $T_1 = 0.3$ s at a temperature of 1.3 K was reported [96]. Extrapolation of the $T_1^{(\beta)}$ relaxation data of Cs-SWNT (CsC_8) to low temperatures yields $T_1^{(\beta)} \sim 0.02$ s around $T \sim 1$ K.

The relaxation and Knight shift data in GIC were explained with a spin density on the Cs nuclei of 20% and thus an incomplete electron charge transfer [96,216]. This increased electron spin density on the Cs nuclei is comparable with the result obtained in Cs intercalated SWNT (CsC_8 , β -line), where the spin density on the Cs nuclei was similarly estimated to 20%.

Higher Stage (> I) Cs-GIC

For pure higher stage Cs-GIC (stage II, III and IV), single quadrupolar shaped ^{133}Cs NMR lines were observed in the shift range between -450 ppm ($T = 10$ K) and +300 ppm ($T = 10$ K, CsC_{24}). For stage II Cs-GIC (CsC_{24}), the temperature dependent spin-lattice relaxation rate extends over 4 orders of magnitude [97], comparable to the observed $T_1^{(\alpha)}$ relaxation dependence in Fig. 4.16.

Therefore, line position and relaxation behavior suggest a structural similarity between higher stage Cs-GIC and Cs-SWNT (low intercalation levels, α -line).

In the case of Cs-GIC (CsC_{24}), the low temperature data were interpreted as Cs atoms being located in symmetric graphitic hexagonal carbon sites with their s -electrons completely transferred to the graphitic lattice. Above 300 K it was suggested, that Cs atoms start to displace from these symmetric sites, recovering part of their s -electrons. These interpretations were supported by various other spectroscopy techniques [97, 236]. As already mentioned, the process of a partial recovery of s -electrons could explain the observed temperature dependence of the β -line shifts in Fig. 4.24.

4.4 Summary and Discussion

SWNT were vapor phase intercalated with Cs by mixing pristine SWNT with a saturation intercalated sample CsC_8 in different ratios. Subsequent vacuum annealing yielded new Cs-SWNT stoichiometries. Analysis of static ^{13}C NMR spectra just before vacuum annealing enabled to estimate the stoichiometries of Cs intercalated SWNT samples.

^{13}C NMR:

- ^{13}C NMR MAS and MAT experiments show the presence of two different types of carbon environments in all intercalated samples. The two carbon environments can be explained with the finite size effect as well as a localized density of states due to Cs ions located close to SWNT. The finite size effect considers the different surface- and 'bulk' response of a SWNT bundle which is dominantly expressed in different bulk- and surface susceptibilities.
- The existence of two kinds of carbon environments is confirmed by ^{13}C NMR spin-lattice relaxation measurements, since the magnetization recovery after saturation always follows a biexponential recovery curve. The ratio of the relaxation components monotonically follows the Cs concentration.
- The temperature dependence of the spin-lattice relaxation rates $1/T_1$ exhibits a Korringa behavior and no signature for semiconducting SWNT is found.
- By analyzing the temperature dependence of the $1/T_1$, the density of states at the Fermi level $n(\varepsilon_F)$ is estimated. With increasing Cs concentration $n(\varepsilon_F)$ increases monotonically. Additionally, the behavior of $n(\varepsilon_F)$ suggests a limitation of the Cs-C electron charge transfer at high intercalation levels.
- A deviation of $1/T_1$ from Korringa law at lower temperatures is explained with localized paramagnetic relaxation due to impurities and defects like dangling bonds. Since the deviation already occurs at a temperature of 150 K, relaxation due to incipient superparamagnetism of the catalyst Rh or the opening of a band gap is rather unlikely.

^{133}Cs NMR

NMR spectra and relaxation measurements indicate the presence of two different types of Cs ions intercalated in the SWNT bundle. The spectra clearly show, that at low intercalation levels first the type of fully ionized $\text{Cs}^{(\alpha)+}$ ions are intercalated, whereas at higher Cs stoichiometries a second type of $\text{Cs}^{(\beta)+}$ ions is additionally intercalated in the SWNT bundle. At room temperature, the corresponding ^{133}Cs NMR lines are shifted to 0 ppm (α -Cs) and 2800 ppm (β -Cs).

Cs α -line

- At low temperatures the rigid-lattice linewidth of the α -line is dominated by quadrupolar interactions with a quadrupolar coupling constant of $\omega_Q^{(\alpha)} \sim 2\pi \cdot 150$ kHz. The $\text{Cs}^{(\alpha)+}$ ions exhibit a weak hyperfine coupling to the SWNT conduction electrons.
- At higher temperatures, ^{133}Cs NMR linewidth- and $1/T_2$ relaxation analysis suggest a thermally activated slow-motion diffusion process of the $\text{Cs}^{(\alpha)+}$ ions along the interstitial channels of the SWNT bundle. The activation energy is estimated to $E_{A1} \sim 0.1$ eV.
- A second weak-collision relaxation process corresponds to an inter-channel diffusion of $\text{Cs}^{(\alpha)+}$ ions perpendicular to the SWNT bundle with an activation energy $E_{A2} \sim 0.29$ eV.

Cs β -line

- The β -line exhibits a quadrupolar structure with a quadrupolar coupling constant of $\omega_Q^\beta \sim 2\pi \cdot 100$ kHz and an asymmetry-parameter of $\eta^\beta \sim 0.3$. The well pronounced quadrupolar lineshape is observable up to high temperatures which indicates a weak temperature dependence of the EFG at the site of the Cs nuclei.
- The temperature dependence of the second moment suggests a slightly thermally activated dynamical behavior of the $\text{Cs}^{(\beta)+}$ ions. Since the EFG is almost temperature independent, a highly structural molecular Cs order has to be assumed. Possibly the $\text{Cs}^{(\beta)+}$ ions occupy well defined atom positions relative to the carbon lattice.

- Korringa relaxation behavior in the investigated temperature range suggests a strong hyperfine coupling between Cs nuclei and conduction electrons on the carbon nanotubes.
- By comparing the β -line shift with the Knight shift of pure Cs metal, a spin density on the nuclei of 20% can be calculated for CsC₈, which corresponds to a partial charge transfer. A highly probable Cs(6s) - C(2p) hybridization explains both, the incomplete charge transfer as well as the observed strong hyperfine couplings.
- Thermally assisted fluctuations of unpaired electron spins located at defects couple through SWNT conduction electrons to the localized electron distribution of the Cs-C hybridization. At low temperatures, spin-spin relaxation and stimulated echo decay behavior are dominated by these fluctuations.

Yet unclear is the spatial distribution of the Cs ions in the SWNT bundles. Conceivable and in agreement with the ¹³C and ¹³³Cs NMR measurements are both, a concentration of Cs ions in the SWNT bundles centre as well as a homogenous distribution of Cs ions across the bundle.

Structural Cs intercalation simulations clearly show that due to energetically reasons Cs adsorption in the central part of a SWNT bundle is more favorable than adsorption on a bundle surface. The additional increase of the bundle lattice constant upon intercalation should provide enough space for all Cs ions to be located inside the SWNT bundle [111].

On the other hand, defects are randomly distributed in a SWNT bundle and it can be assumed that Cs hybridization mainly occurs at reactive defective sites. Therefore, a **homogenous distribution of hybridized Cs^{(β)⁺ ions}** all over the bundle must be expected.

The fully ionized **Cs^{(α)⁺ ions}** are expected to **diffuse throughout the whole SWNT bundle** in a hindered motion process. The presence of the localized Cs^{(β)⁺ ions is probably the main reason for the hindered Cs^{(α)⁺ ions motion process. A hindered motion due to defective nanotubes or an intrinsic effect ascribed to the tubular system structure is rather negligible.}}

Summary

In the present work, nuclear magnetic resonance (NMR) experiments were carried out on Li and Cs intercalated single-walled carbon nanotube (SWNT) bundles. The alkali metals were intercalated in raw SWNT as starting material. The raw nanotubes are supposed to possess closed end caps whereby possible alkali adsorption sites are only provided by the interstitial channels as well as the surface of a carbon nanotube bundle. The interior space of the present SWNT is supposed to be predominantly inaccessible for penetration by alkali atoms.

The goal of the work was to elucidate the intercalation mechanism as well as the dynamical and structural properties of the intercalated system. By performing temperature dependent ^1H , ^7Li , ^{13}C and ^{133}Cs NMR experiments, in particular the following important results were obtained:

Li intercalated SWNT:

- Lithium was chemically intercalated in SWNT bundles by using solutions of aromatic hydrocarbons, the solvating agent tetrahydrofuran (THF) and SWNT. ^{13}C NMR measurements enabled to follow the density of states at the Fermi level for various Li intercalation stoichiometries. Generally, pristine SWNT consist of a mixture of metallic and semiconducting SWNT. Upon intercalation and subsequent Li-C electron charge transfer the Fermi level is tuned. The intercalated system reveals a pure metallic behavior and a signature for semiconducting SWNT cannot be found any more. However, at higher Li intercalation stoichiometries an incomplete electron charge transfer is observed.
- ^7Li NMR experiments show the presence of two types of Li-nuclei with different environments in the SWNT bundles: at low intercalation levels first, completely ionized α -type Li ions are intercalated, whereas at higher stoichiometries a second type of partially ionized β -type Li is adsorbed by the SWNT host.
 - The above sketched charge transfer limitation is explained by the presence of partially ionized $\text{Li}^{(\beta)+}$ ions, which show a hybridization of the $\text{Li}(2s)$ orbitals with the SWNT $\text{C}(2p)$ orbitals. ^7Li NMR demonstrates a remarkable Knight shift for these β -type Li nuclei as well as a strong hyperfine coupling to SWNT conduction electrons.

- The α -type Li^+ ions exhibit a high-temperature dynamical process with an activation energy of $\Delta E \sim 0.4$ eV which is interpreted as a $\text{Li}^{(\alpha)+}$ cation diffusion along the interstitial channels of the SWNT bundles.
- ^1H NMR investigations were carried out in order to investigate the role of the THF solvent molecules. The experiments provide evidence for the existence of two types of inequivalent THF solvent molecules. They are most likely coupled by a thermally activated exchange process with an activation energy of $E_A \sim 0.72$ eV. At temperatures below 300 K, THF molecules are perpendicularly arranged in between adjacent SWNT and exhibit an axial rotation around their dipolar axis with an activation energy of $\Delta E \sim 0.13$ eV. The Li^+ cations are located halfway between adjacent SWNT and pin the oxygen-(THF) atoms to their immediate neighborhood.

Above room temperature, THF molecules detach from the SWNT and start to isotropically rotate and diffuse along the interstitial channels of the SWNT bundles.

Remarkable diamagnetic shifts of the ^1H NMR lines can be explained with an extremely large diamagnetic shielding of the carbon nanotube bundles since the SWNT exhibit highly anisotropic diamagnetic susceptibilities.

Cs intercalated SWNT:

- Various stoichiometries of vapor phase Cs intercalated SWNT bundles were investigated. ^{13}C NMR MAS and MAT experiments show the presence of two different types of carbon environments in all intercalated samples. The two carbon environments can be explained with the finite size effect and therewith the bulk- and surface susceptibility of the SWNT bundles as well as a localized density of states due to Cs ions located close to SWNT.

Comparable to Li intercalation in SWNT, ^{13}C NMR spin-lattice relaxation measurements enabled to determine the density of states at the Fermi level. The increase of the density of states upon intercalation enhances the metallicity of the SWNT system and no semiconducting SWNT are observable any more.

However, at higher intercalation levels a Cs-C electron charge transfer limitation is observed.

- ^{133}Cs NMR measurements indicate the presence of two coexisting types of Cs ions intercalated in the SWNT bundle. At low intercalation levels fully ionized

Cs^{(α)+} ions are exclusively intercalated, whereas at higher Cs stoichiometries a second type of Cs^{(β)+} ions is additionally intercalated in the SWNT bundle.

- The Cs^{(α)+} ions exhibit a thermally activated slow-motion diffusion process along the interstitial channels of the SWNT bundle as well as an inter-channel diffusion perpendicular to the SWNT bundle. The activation energies for both processes are $E_{A1} \sim 0.1$ eV and $E_{A2} \sim 0.29$ eV, respectively.
- The Cs^{(β)+} ions are only subject to a weakly temperature dependence of the electric field gradient at the site of the Cs nuclei which suggests a highly structural molecular Cs. Possibly the Cs⁺ ions occupy well defined atom positions relative to the carbon lattice covering the SWNT fragmentarily. ¹³³Cs NMR Korringa relaxation behavior and Knight shifts suggest a Cs(6s) - C(2p) hybridization for the Cs^{(β)+} ions which explains the observed charge transfer limitation at higher Cs stoichiometries.

Even though, intercalated SWNT and alkali-GIC are different intercalation systems, the apparent resemblance of line positions, line shapes and relaxation data indicate strongly a substantial similarity in structural alkali-carbon arrangement and charge transfer characteristics.

For the case of alkali intercalated SWNT, the present work was able to experimentally confirm for the first time the theoretical predictions of alkali-carbon hybridization at higher alkali intercalation stoichiometries [131, 142].

The results obtained here demand further theoretical calculations and dedicated experimental investigations on intercalated (interstitial bundle channels and nanotube inner-core) SWNT with various molecular species. In particular, intercalation of C₆₀ inside SWNT (peapods, C₆₀@SWNT) has come to attention in the past 5 years [117, 237–241]. Encapsulation of fullerenes in SWNT enables to tune and modify the electronic properties of the nanotube without affecting its atomic structure, which makes it to a promising system for applications in future novel molecular electronic devices [240, 241]. Possibly, further theoretical and experimental work enables finally to understand and control these hybrid structures and the technique of single molecules encapsulation might one day be used to define highly efficient on-carbon-nanotube electronic devices.

Zusammenfassung

Kohlenstoff ist das Element, das mit Abstand am häufigsten in den meisten chemischen Verbindungen vorkommt. Deshalb darf es nicht überraschen, dass auch der elementare Kohlenstoff in zahlreichen Erscheinungsformen auftritt. So sind Diamant (3D) und Graphit (2D) zwei natürliche bekannte kristalline Grundformen aus reinem Kohlenstoff. In den letzten Jahren haben von Graphit abgeleitete Nanostrukturen viel Aufmerksamkeit erregt. So wurden 1986 Harold Kroto von der University of Sussex, Robert Curl und Richard Smalley von der Rice University für die Entdeckung der Fullerene mit dem Nobelpreis für Chemie ausgezeichnet. Fullerene stellen geschlossene hohle Kohlenstoff-Käfige im Nanometermaßstab dar. Das bekannteste Fulleren ist dabei das C_{60} , auch unter dem Namen *Buckminster Fulleren* oder *Buckyball* bekannt. Eine der interessantesten Eigenschaften der Fulleren-Familie ist das Auftreten von Supraleitung in Alkali interkaliertem C_{60} . Fullerid-Supraleiter weisen nach den keramischen Hochtemperatur-Supraleitern die höchsten Sprungtemperaturen auf, was ihnen unter den organischen Supraleitern eine besondere Stellung verleiht.

Seit kurzem wird intensiv an potentiellen medizinischen Anwendungen der Fullerene geforscht. Im Blickpunkt stehen dabei die Entwicklung von spezifischen antibiotischen Strukturen (um z.B. das HIV-Virus zu blockieren), sowie der Einsatz als Kontrastmittel für Röntgen-Untersuchungen und magnetische Bildgebungsverfahren.

Eine weitere Form von Kohlenstoff-Nanostrukturen bilden Carbon Nanotubes (Kohlenstoff-Nanoröhrchen). Sie entsprechen Zylindern aus nahtlos aufgerollten Graphitschichten und damit einem Gitter sp^2 -hybridisierter Kohlenstoffatome. Die Enden der Nanoröhren können mit halbkugeligen Kappen (Fullerenhalbkugeln) abgeschlossen sein. Carbon Nanotubes treten in ein- oder mehrwandiger Form auf und werden daher als *single-walled Nanotubes* (SWNT) oder *multi-walled Nanotubes* (MWNT) bezeichnet. Bei Durchmessern von einem bis zu zwanzig Nanometern erreichen sie eine Länge von einigen hundert Nanometern bis einigen Millimetern. Typischerweise lagern sie sich aufgrund von van der Waals Kräften zu Bündeln von zehn bis hundert Carbon Nanotubes zusammen und bilden dabei ein regelmäßiges Dreiecksgitter.

Carbon Nanotubes wurden in den frühen siebziger Jahren von Morinobu Endo entdeckt. Unglücklicherweise erregten sie erst 1991 nach der Wiederentdeckung durch Sumio Iijima das eigentliche Interesse der Wissenschaft.

Seit diesem Zeitpunkt werden Carbon Nanotubes aufgrund ihrer faszinierenden elektronischen, mechanischen und thermischen Eigenschaften intensiv untersucht. Erwähnenswert sind zum Beispiel die elektronischen Eigenschaften von Carbon Nanotubes. Je nach Chiralität zeigen sie metallischen oder halbleitenden Charakter – als Nanotube-Rohmaterial liegen deshalb metallische und halbleitende Carbon Nanotubes typischerweise in einer Verteilung von 1/3 : 2/3 vor. Bei der Verwendung als eindimensionale Drähte verhalten sie sich Carbon Nanotubes wie ballistische Leiter (d.h. der Widerstand hängt weder vom Querschnitt noch von der Länge ab, *Quantendraht*).

Durch die Interkalation von Alkali Metallen sollte es möglich sein, diese elektronischen Eigenschaften der Carbon Nanotubes weiter zu verändern und anzupassen – im Fall des C₆₀ führte Interkalation zur Entdeckung der Supraleitung in diesem Material.

Die Verwendung von Carbon Nanotubes im Zusammenhang mit dem Alkali Metall Lithium hat in den letzten Jahren im Bezug auf Lithium-Ionen Batterien erheblich an Bedeutung gewonnen. So finden seit der Kommerzialisierung dieser Batterien durch Sony im Jahr 1990 Carbon Nanotubes vermehrten Einsatz als beigemischtetes Material, was die Lebensdauer der Batterien erheblich verlängert. Desweiteren wird intensiv an der Verwendung von Carbon Nanotubes als Batterie-Anoden-Material geforscht.

Die vorliegende Arbeit befasst sich mit der Untersuchung von Lithium und Caesium interkalierten SWNT mittels der Methode der Kernspinresonanz (NMR). Die verwendeten SWNT sind überwiegend mit Endkappen abgeschlossen, da als Ausgangsmaterial chemisch unbehandelte (ungereinigte), Raman-selektierte SWNT verwendet wurden. Es kann daher davon ausgegangen werden, dass die Alkali Metalle aufgrund des Interkalationsprozesses ausschließlich in die SWNT-Kanäle der Nanotube-Bündel, sowie auf deren Oberflächen adsorbiert werden.

Ziel der Arbeit war es, den Interkalationsmechanismus, sowie die dynamischen und strukturellen Eigenschaften der interkalierten Systeme aufzuklären. Zum Einsatz kamen hierbei verschiedene Festkörper-NMR Spektrometer mit Magnetfeldern zwischen 4.2 T und 9.1 T. Unter Anwendung von temperaturabhängigen ¹H, ⁷Li, ¹³C und ¹³³Cs NMR Experimenten wurden im Einzelnen die folgenden wichtigen Erkenntnisse gewonnen:

Li Interkalierte SWNT:

- Bündel von Carbon Nanotubes wurden chemisch mittels Verwendung von verschiedenen aromatischen Kohlenwasserstoffen und dem Lösungsmittel Tetrahydrofuran (THF) interkaliert. Die Zustandsdichte an der Fermi-Energie konnte für die gewonnenen Interkalations-Stöchiometrien über ^{13}C NMR Messungen bestimmt werden. Üblicherweise zeigen ^{13}C NMR Spin-Gitter Relaxationsmessungen an unbehandelten SWNT zwei Relaxationskomponenten im Verhältnis 60%:40%, welche halbleitenden und metallischen SWNT zugeordnet werden. Durch die Interkalation und dem damit verbundenen Li-C Ladungstransfer wird das Fermi-Niveau verschoben, wodurch das System nur noch ein rein metallisches Verhalten zeigt – halbleitende SWNT sind nicht mehr beobachtbar. Allerdings stellt sich bei hohen Li Interkalationsstöchiometrien ein unvollständiger Elektronen-Ladungstransfer ein.
- ^7Li NMR Messungen weisen auf das Vorhandensein zweier unterschiedlicher Arten von interkalierten Li-Ionen mit unterschiedlicher Umgebung hin: Bei niedrigen Li-Stöchiometrien werden zuerst vollständig ionisierte α -Li Ionen interkaliert, wohingegen bei höheren Li-Stöchiometrien eine zusätzliche Interkalation von unvollständig ionisierten β -Li Ionen stattfindet.
 - Diese unvollständig-ionisierten $\text{Li}^{(\beta)+}$ Ionen weisen eine Hybridisierung der $\text{Li}(2s)$ -Orbitale mit den $\text{C}(2p)$ -Orbitalen der SWNT auf. Dies erklärt auch den beobachteten unvollständigen Elektronen-Ladungstransfer. Die ^7Li NMR Linie der $\text{Li}^{(\beta)+}$ Ionen zeigt aufgrund der Hybridisierung sowohl eine sehr starke Knight-Verschiebung, als auch eine starke Hyperfeinkopplung der Li Kerne and das Leitungselektronensystem der SWNT.
 - Die Dynamik der α -Li Ionen ist stark temperaturabhängig – bei höheren Temperaturen findet eine Diffusion der $\text{Li}^{(\alpha)+}$ Kationen in den SWNT-Kanälen der Nanotube-Bündel statt. Die Aktivierungsenergie für diesen Bewegungsprozess beträgt $\Delta E \sim 0.4$ eV.
- Da die Li interkalierten SWNT unter Verwendung des Lösungsmittels THF hergestellt wurden, muss von einer Kointerkalation dieser THF Moleküle ausgegangen werden. Um die Eigenschaften der THF Moleküle im interkalierten System aufzuklären, wurden ^1H NMR Experimente durchgeführt.

Diese weisen auf zwei unterschiedliche Konfigurationen von THF Molekülen hin, welche über einen thermisch aktivierten Austauschprozess gekoppelt sind. Die

Aktivierungsenergie für diesen Austauschprozess beträgt $E_A \sim 0.72$ eV. Unterhalb einer Temperatur von 300 K scheinen die flachen THF Moleküle senkrecht zu den Oberflächen der Nanotubes angeordnet zu sein. Sie führen dabei eine axiale Rotation um ihre dipolare Sauerstoff-Achse mit einer Aktivierungsenergie von $\Delta E \sim 0.13$ eV durch. Durch die starke elektrostatische Wechselwirkung zwischen den elektronegativen THF-Sauerstoffatomen und den positiv geladenen $\text{Li}^{(\beta)+}$ Kationen befinden sich die Kationen zwischen benachbarten SWNT und in unmittelbarer Umgebung der THF Moleküle. Oberhalb von 300 K lösen sich die Moleküle von den SWNT und beginnen dabei isotrop zu rotieren. Zusätzlich findet eine Diffusion entlang der Kanäle der SWNT-Bündel statt.

Bemerkenswert ist die diamagnetische Verschiebung der ^1H NMR Linien im Spektrum, was auf eine starke diamagnetische Abschirmung der SWNT-Bündel hinweist. Der Grund für die Abschirmung ist eine hohe anisotrope diamagnetische Suszeptibilität der SWNT.

Cs Interkalierte SWNT:

- Cs wurde über die Dampfphase in SWNT-Bündel interkaliert. Um verschiedene Stöchiometrien kontrolliert herzustellen, wurde sättigungsinterkalierte SWNT (CsC_8) mit unbehandelten SWNT in verschiedenen Verhältnissen gemischt. Durch Erhitzen der Mischungen wurde Cs deinterkaliert und über die gesamte Probe verteilt. Anschließendes Abkühlen führte wiederum zur Re-Interkalation in der gesamten Probe und damit zur Entstehung neuer (niedrigerer) Cs-SWNT Stöchiometrien. Über ^{13}C NMR vor dem Erhitzen der Proben war es möglich, die Stöchiometrien der Proben aus dem Verhältnis der verschiedenen Linienintensitäten für SWNT Rohmaterial und CsC_8 zu bestimmen.

^{13}C NMR MAS und MAT Experimente konnten in allen interkalierten Proben (d.h. nach dem Erhitzen und vollständiger Re-Interkalation) zwei Arten von Kohlenstoff-Umgebungen nachweisen. Das Auftreten zweier unterschiedlicher Umgebungen ist dabei sowohl mit dem *Finite-Size Effekt* der SWNT-Bündel, als auch über eine lokalisierte Zustandsdichte erklärbar: Die Lokalisierte Zustandsdichte hat ihre Ursache in Cs-Ionen, die sich sehr dicht an der SWNT Oberfläche befinden; der Finite-Size Effekt zieht die endliche Größe der SWNT-Bündel in Betracht, wodurch unterschiedliche Suszeptibilitäten an der Bündel-Oberfläche im Vergleich zum Inneren eines SWNT-Bündels berücksichtigt werden müssen.

Über ^{13}C NMR Spin-Gitter Relaxationsmessungen konnte der Verlauf der Zustandsdichte an der Fermi-Energie in Abhängigkeit von der Cs Stöchiometrie bestimmt werden. Es zeigt sich, dass durch die Interkalation der metallische Charakter des Systems zunimmt – halbleitende SWNT sind, wie schon im Fall der Li Interkalation, nicht mehr beobachtbar.

Ebenso wie im Fall der Li Interkalation ergibt sich bei hohen Interkalationsstufen eine Begrenzung des Cs-C Elektronen-Ladungsübertrages.

- ^{133}Cs NMR konnte in Abhängigkeit der Cs-Stöchiometrie zwei koexistierende Arten von Cs-Ionen nachweisen. Bei niedrigen Interkalationsstufen werden ausschließlich α -Cs Ionen interkaliert, wohingegen bei höheren Cs Stöchiometrien die Interkalation einer zweiten Art von β -Cs Ionen stattfindet.
 - Die vollständig ionisierten $\text{Cs}^{(\alpha)+}$ Kationen führen eine langsame thermisch aktivierte Diffusion entlang der Kanäle der SWNT-Bündel, sowie einen zweiten Diffusionsprozess senkrecht zu diesen Kanälen durch. Die Aktivierungsenergien für beide Prozesse betragen $E_{A1} \sim 0.1$ eV beziehungsweise $E_{A2} \sim 0.29$ eV
 - Der elektrische Feldgradient am Ort der $\text{Cs}^{(\beta)+}$ Ionen weist lediglich eine schwache Temperaturabhängigkeit auf, was auf eine hohe molekulare Cs-Ordnung hinweist. Es ist denkbar, dass die $\text{Cs}^{(\beta)+}$ Ionen definierte Gitterplätze relativ zum hexagonalen Kohlenstoffgitter der SWNT einnehmen. Es ist jedoch von einer lückenhaften Bedeckung der SWNT Oberfläche auszugehen.

Das ^{133}Cs NMR Korringa-Relaxationsverhalten, sowie die starke Knight-Verschiebung der β -Linie lassen eine $\text{Cs}(6s) - \text{C}(2p)$ Hybridisierung der $\text{Cs}^{(\beta)+}$ Ionen mit den C Atomen der SWNT vermuten. Diese Hybridisierung erklärt schließlich auch die beobachtete Begrenzung des Cs-C Elektronen-Ladungsübertrages bei höheren Cs-Stöchiometrien.

Alkali interkalierte SWNT und Alkali-interkalierter Graphit (GIC) weisen bezüglich NMR Linienlagen, Linienformen und Relaxationsdaten erstaunliche Ähnlichkeiten auf. Beide Systeme gleichen sich sehr stark in der Anordnung der Alkali Ionen relativ zum Kohlenstoffgitter, als auch in den Eigenschaften des Alkali-Kohlenstoff Ladungsübertrages.

In dieser Arbeit konnte zum ersten Mal experimentell die theoretisch vorhergesagte Alkali-Kohlenstoff-Hybridisierung bei höheren Alkali-Stöchiometrien nachgewiesen werden [131, 142].

Neben der Interkalation von Alkali-Metallen in den Kanälen der SWNT-Bündel gewinnt die Interkalation anderer Moleküle in SWNT zunehmend an Bedeutung. Insbesondere hat in den vergangenen 5 Jahren die Interkalation von C_{60} in den inneren Hohlraum von offenen SWNT (Hybridstruktur) große Aufmerksamkeit erregt [117, 237–241]. Der Vorteil der Interkalation von Molekülen im Inneren einer SWNT liegt darin, die elektronischen Eigenschaften dieser Nanotube zu verändern, gleichzeitig jedoch nach Außen hin die atomare Struktur beizubehalten. Dies eröffnet neue Möglichkeiten für Anwendungen in molekularen elektronischen Schaltungen [240, 241]. Die in dieser Arbeit gewonnenen Erkenntnisse regen dazu an, durch weitere theoretische Berechnungen und entsprechende Experimente diese neuartigen Hybridstrukturen verstehen und kontrollieren zu können. Vielleicht bilden diese Strukturen eines Tages die Basis für hoch effiziente elektronische Schaltungen mit Hilfe von Carbon Nanotubes.

Bibliography

- [1] H. Kroto, J. Heath, S. O'Brien, R. Curl and R. Smalley, *Nature* **318**, 162 (1985).
- [2] R. Haddon, A. F. Hebard, M. J. Rosseinsky, D. W. Murphy, S. J. Duclos, B. Lyons, B. Miller, J. M. Rosamilia, R. M. Fleming, A. R. Kortan, H. Glarum, A. V. Makhija, A. J. Muller, R. H. Eick, S. M. Zahurak, R. Tycko, G. Dabbagh and F. A. Thiel, *Nature* **350**, 320 (1991).
- [3] C. H. Pennington, V. A. Stenger, C. H. Recchia, C. Hahm, K. Gorny, V. Nandor, D. R. Buffinger, S. M. Lee and R. P. Ziebarth, *Phys. Rev. B* **53**, R2967 (1996).
- [4] C. H. Pennington and V. A. Stenger, *Rev. Mod. Phys.* **68**, 855 (1996).
- [5] A. Ramirez, *Supercond. Rev.* **1**, 1 (1994).
- [6] G. Zimmer, K. F. Thier, M. Mehring and F. Rachdi, *Appl. Magn. Res.* **11**, 263 (1996).
- [7] V. Buntar and H. W. Weber, *Supercond. Sci. Tech.* **9**, 599 (1996).
- [8] R. A. Freitas, *NanoNews-Now* **3** (2003).
- [9] M. Kralj and K. Pavelic, *EMBO J.* **4**, 1008 (2003).
- [10] J. Gorman, *Science News Online* **162**, 26 (2002).
- [11] M. Endo, A. Oberlin and T. Koyama, *J. Cryst. Growth* **32**, 335 (1976).
- [12] S. Iijima, *Nature* **354**, 56 (1991).
- [13] M. Endo, C. Kim, K. Nishimura, T. Fujino and K. Miyashita, *Carbon* **38**, 183 (2000).
- [14] J. Tirado, *Mater. Sci. Eng.* **40**, 103 (2003).
- [15] B. Gao, A. Kleinhammes, X. P. Tang, C. Bower, L. Fleming, Y. Wu and O. Zhou, *Chem. Phys. Lett.* **307**, 153 (1999).
- [16] M. S. Dresselhaus and G. Dresselhaus, *Adv. Phys.* **30**, 139 (1981).
- [17] P. Lauginie, A. Messaoudi and J. Conard, *Synth. Met.* **56**, 3002 (1993).

- [18] F. Beguin, B. Gonzalez, J. Conard, H. Estrade-Szwarckopf D. Guerard, *Synth. Met.* **12**, 187 (1985).
- [19] J. Conard, A. Messaoudi, F. Beguin and V. Nalimova, *J. Phys. Chem. Solids* **55**, 787 (1994).
- [20] A. Abragam, *Principles of Nuclear Magnetism*, Oxford University Press, Oxford, 1989.
- [21] J. K. M. Sanders and B. K. Hunter, *Modern NMR Spectroscopy*, Oxford University Press, Oxford, New York, Tokyo, 1987.
- [22] C. P. Slichter, *Principles of Magnetic Resonance*, Springer, Berlin, Heidelberg, 1990.
- [23] M. Mehring and A. Weberruß, *Object-Oriented Magnetic Resonance*, Academic Press, San Diego, San Francisco, New York, Boston, London, Sydney, Tokyo, 2001.
- [24] M. Mehring, *Principles of High Resolution NMR in Solids*, Springer, Berlin, Heidelberg, 1983.
- [25] J. Herzfeld and A. Berger, *J. Chem. Phys.* **73**, 6021 (1980).
- [26] A. Bax, N. M. Szeverenyi and G. E. Maciel, *J. Magn. Reson.* **52**, 147 (1982).
- [27] J. Z. Hu, W. Wang, F. Liu, M. S. Solum, D. W. Alderman, R. J. Pugmire and D. M. Grant, *J. Magn. Reson., Series A* **113**, 210 (1995).
- [28] Z. Gan and R. R. Ernst, *J. Magn. Reson., Series A* **123**, 140 (1996).
- [29] M. Mehring, *Appl. Magn. Reson.* **3**, 383 (1992).
- [30] Y. Maniwa, N. Sato, H. Tou, K. Kikuchi, S. Suzuki, Y. Achiba, M. Kosaka and K. Tanigaki, *Phys. Rev. B* **58**, 12433 (1998).
- [31] P. Lauginie and J. Conard, *Mol. Cryst. Liq. Cryst.* **245**, 19 (1994).
- [32] Y. Maniwa, D. Sugiura, K. Kume, K. Kikuchi, S. Suzuki, Y. Achiba, I. Hirokawa, K. Tanigaki, H. Shimoda and Y. Iwasa, *Phys. Rev. B* **54**, R6861 (1996).
- [33] V. P. Antropov, I. I. Mazin, O. K. Andersen, A. I. Liechtenstein and O. Jepsen, *Phys. Rev. B* **47**, 12373 (1993).

- [34] C. Goze-Bac, S. Latil, P. Lauginie, V. Jourdain, J. Conard, L. Duclaux, A. Rubio and P. Bernier, *Carbon* **40**, 1825 (2002).
- [35] M. Mehring and O. Kanert, *Z. f. Naturforsch.* **24a**, 768 (1969).
- [36] D. Freude and J. Haase, *Quadrupole Effects in Solide-State Nuclear Magnetic Resonance*, volume 29 of *NMR Basic Principles and Progress*, Springer, Berlin, Heidelberg, 1993.
- [37] M. Mehring, F. Rachdi and G. Zimmer, *Philos. Mag. B* **70**, 787 (1994).
- [38] A. Abragam and B. Bleaney, *Electron Paramagnetic Resonance of Transition Ions*, Oxford University Press, Oxford, 1970.
- [39] N. Bloembergen, E. M. Purcell and R. V. Pound, *Phys. Rev.* **73**, 679 (1948).
- [40] D. C. Ailion and C. P. Slichter, *Phys. Rev.* **137**, A235 (1965).
- [41] D. C. Ailion and P.-P. Ho, *Phys. Rev.* **168**, 662 (1968).
- [42] D. Ailion, NMR and Ultraslow Motions, in *Advances in Magnetic Resonance*, J. S. Waugh [eds.], volume 5, pages 177, Academic Press, New York, London, 1971.
- [43] C. P. Slichter and D. Ailion, *Phys. Rev.* **135**, A1099 (1964).
- [44] D. A. Erilov, R. Bartucci, R. Guzzi, D. Marsh, S. A. Dzuba and L. Sportelli, *J. Phys. Chem. B* **108**, 4501 (2004).
- [45] S. A. Dzuba, E. P. Kirilina, E. S. Salnikov and L. V. Kulik, *J. Chem. Phys.* **122**, 094702 (2005).
- [46] N. S. Sullivan, M. Devoret and D. Estève, *Phys. Rev. B* **30**, 4935 (1984).
- [47] L. V. Kulik, I. A. Grigor'ev, E. S. Salnikov, S. A. Dzuba and Y. D. Tsvetkov, *J. Phys. Chem. A* **107**, 3692 (2003).
- [48] N. S. Sullivan, D. Esteve and M. Devoret, *J. Phys. C: Solid State Physics* **15**, 4895 (1982).
- [49] M. S. Dresselhaus, G. Dresselhaus and R. Saito, Physics of Carbon Nanotubes, in *Carbon Nanotubes*, M. Saito, S. Iijima and M. S. Dresselhaus [eds.], pages 27, Pergamon, New York, 1996.

-
- [50] M. S. Dresselhaus, R. Saito and G. Dresselhaus, *Physical Properties of Carbon Nanotubes*, Imperial College Press, London, 1999.
- [51] P. L. McEuen, C. Schönberger, L. Forro, H. Dai, W. A. de Heer and R. Martel, Carbon nanotubes, 2000, Special Issue.
- [52] J. Bernholc, D. Brenner, M. Buongiorno Nardelli, V. Meunier and C. Roland, *Annu. Rev. Mater. Res.* **32**, 347 (2002).
- [53] J. Robertson, *Materials Today* **7**, 46 (2004).
- [54] R. H. Baughman, A. A. Zakhidov and W. A. de Heer, *Science* **297**, 787 (2002).
- [55] M. Dresselhaus, G. Dresselhaus and A. Jorio, *Annu. Rev. Mater. Res.* **34**, 247 (2004).
- [56] P. Petit and A. Loiseau, *Comptes Rendus Physique* **4**, 967 (2003).
- [57] M. Terrones, *Annu. Rev. Mater. Res.* **33**, 419 (2003).
- [58] M. Endo, T. Hayashi, Y. A. Kim, M. Terrones and M. S. Dresselhaus, *Philos. Transact. Ser. A: Math. Phys. Eng. Sci.* **362**, 2223 (2004).
- [59] S. J. Tans, A. R. M. Verschueren and C. Dekker, *Nature* **393**, 49 (1998).
- [60] V. Derycke, R. Martel, J. Appenzeller and P. Avouris, *Nano Lett.* **1**, 453 (2001).
- [61] S. J. Wind, J. Appenzeller, R. Martel, V. Derycke and P. Avouris, *Appl. Phys. Lett.* **80**, 3817 (2002).
- [62] J. Guo, M. Lundstrom and S. Datta, *Appl. Phys. Lett.* **80**, 3192 (2002).
- [63] W. Hoenlein, F. Kreupl, G. S. Duesberg, A. P. Graham, M. Liebau, R. Seidel and E. Unger, *Mater. Sci. Eng. C* **23**, 663 (2003).
- [64] G. S. Duesberg, A. P. Graham, M. Liebau, R. Seidel, E. Unger, F. Kreupl and W. Hoenlein, *Nano Lett.* **3**, 257 (2003).
- [65] A. Bachtold, P. Hadley, T. Nakanishi and C. Dekker, *Science* **294**, 1317 (2001).
- [66] G. Maruccio, R. Cingolani and R. Rinaldi, *J. Mater. Chem.* **14**, 542 (2004).
- [67] R. H. Baughman, C. Cui, A. A. Zakhidov, Z. Iqbal, J. N. Barisci, G. M. Spinks, G. G. Wallace, A. Mazzoldi, D. De Rossi, A. G. Rinzler, O. Jaschinski, S. Roth and M. Kertesz, *Science* **284**, 1340 (1999).

- [68] R. H. Baughman, *Science* **300**, 268 (2003).
- [69] A. B. Dalton, S. Collins, E. Munoz, J. M. Razal, V. H. Ebron, J. P. Ferraris, J. N. Coleman, B. G. Kim and R. H. Baughman, *Nature* **423**, 703 (2003).
- [70] T. Kar, J. Pattanayak and S. Scheiner, *J. Phys. Chem. A* **105**, 10397 (2001).
- [71] M. Schmid, *Untersuchungen an Wasserstoff in Carbon Nanotubes*, Diplomarbeit, Universität Stuttgart, 2001.
- [72] C. Journet, W. K. Maser, P. Bernier, A. Loiseau, M. L. d. l. Chapelle, S. Lefrant, P. Deniard, R. Lee and J. E. Fischer, *Nature* **388**, 756 (1997).
- [73] A. Thess, R. Lee, P. Nikolaev, H. Dai, P. Petit, J. Robert, C. Xu, Y. H. Lee, S. G. Kim, A. G. Rinzler, D. T. Colbert, G. E. Scuseria, D. Tomanek, J. E. Fischer and R. E. Smalley, *Science* **273**, 49 (1996).
- [74] H. Dai, Y. Li, D. Mann, M. Rolandi, W. Kim, A. Ural, S. Hung, A. Javey, J. Cao, D. Wang, E. Yenilmez, Q. Wang, J. F. Gibbons and Y. Nishi, *Nano Lett.* **4**, 317 (2004).
- [75] Y. Saito, Y. Tani, N. Miyagawa, K. Mitsushima, A. Kasuya and Y. Nishina, *Chem. Phys. Lett.* **294**, 593 (1998).
- [76] G. S. Duesberg, W. Blau, H. J. Byrne, J. Muster, M. Burghard and S. Roth, *Synth. Met.* **103**, 2484 (1999).
- [77] S. Bandow, S. Asaka, X. Zhao and Y. Ando, *Appl. Phys. A* **67**, 23 (1998).
- [78] K. B. Shelimov, R. O. Esenaliev, A. G. Rinzler, C. B. Huffman and R. E. Smalley, *Chem. Phys. Lett.* **282**, 429 (1998).
- [79] Y. L. Lee, Y. S. Park, Y. C. Choi, K. S. Kim, D. C. Chung, D. J. Bae, K. H. An, S. C. Lim and X. Y. Zhu, *Carbon* **39**, 655 (2001).
- [80] R. C. Haddon, M. E. Itkis, D. E. Perea, S. Niyogi, S. M. Rickard, M. A. Hamon, H. Hu and B. Zhao, *Nano Lett.* **3**, 309 (2003).
- [81] U. Dettlaff-Weglikowska, J. Wang, J. Liang and S. Roth, Protocol for Quality Control of Bulk Single Wall Carbon Nanotube Materials, in *International Winterschool on Electronic Properties of Novel Materials*, H. Kuzmany, J. Fink, M. Mehring and S. Roth [eds.], volume In Print, Kirchberg, Austria, 2005, American Institute of Physics.

- [82] J. Zhang, H. L. Zou, Q. Qing, Y. L. Yang, Q. W. Li, Z. F. Liu, X. Y. Guo and Z. L. Du, *J. Phys. Chem. B* **107**, 3712 (2003).
- [83] M. J. O'Connell, S. M. Bachilo, C. B. Huffman, V. C. Moore, M. S. Strano, E. H. Haroz, K. L. Rialon, P. J. Boul, W. H. Noon, C. Kittrell, J. Ma, R. H. Hauge, R. B. Weisman and R. E. Smalley, *Science* **297**, 593 (2002).
- [84] D. Guerard and A. Herold, *Carbon* **13**, 337 (1975).
- [85] J. Conard and H. Estrade, *Mater. Sci. Eng.* **31**, 173 (1977).
- [86] G. Roth, K. Luders, P. Pfluger and H.-J. Guntherodt, *Solid State Commun.* **39**, 423 (1981).
- [87] P. Lauginie, *Synth. Met.* **23**, 311 (1988).
- [88] A. Schirmer and P. Heitjans, *Z. f. Naturforsch.* **50**, 643 (1995).
- [89] C.-C. Wan, H.-H. Lee and Y.-Y. Wang, *J. Power Sources* **113**, 285 (2003).
- [90] J. Conard and P. Lauginie, Lithium NMR in Lithium-Carbon Solid State Compounds, in *New Trends in Intercalation Compounds for Energy Storage*, C. Julien, J. Pereira-Ramos and A. Momchilov [eds.], pages 77, Kluwer Academic Publishers, 2002.
- [91] H. Estrade, J. Conard, P. Lauginie, P. Heitjans, F. Fujara, W. Buttler, G. Kiese, H. Ackermann and D. Guerard, *Physica B & C* **99**, 531 (1980).
- [92] O. Tanaike and M. Inagaki, *Carbon* **35**, 831 (1997).
- [93] L. Facchini, M. Quinton and A. Legrand, *Physica B* **99**, 525 (1980).
- [94] J. Conard, M. Gutierrez-Le Brun, P. Lauginie and H. Estrade-Szwarckopf, *Synth. Met.* **2**, 227 (1980).
- [95] J. Conard, H. Estrade, P. Lauginie, H. Fuzellier, G. Furdin and R. Vasse, *Physica B & C* **99**, 521 (1980).
- [96] G. P. Carver, *Phys. Rev. B* **2**, 2284 (1970).
- [97] H. Estrade-Szwarckopf, J. Conard, P. Lauginie, J. V. d. Klink, D. Guerard and P. Lagrange, ^{133}Cs NMR Studies of Cesium GIC, in *Physics of Intercalation Compounds*, volume 38, pages 274, Springer series in Solid State Science, 1981.

- [98] H. Estrade-Szwarczkopf, J. Conard, P. Lauginie, J. V. d. Klink, D. Guerard, P. Lagrange, F. Rousseaux, A. Maaroufi and G. Hermann, Cesium State, Thermal Evolution in CsC₂₄, in *Material Research Society Symposium Proceedings*, volume 20, pages 369, Elsevier Science Publishing Co., Inc., 1983.
- [99] R. Tycko, *J. Phys. Chem. Solids* **54**, 1713 (1993).
- [100] J. Dettmann, *Fullerene: Die Bucky-Balls Erobern die Chemie*, Birkhäuser, Basel, Boston, Berlin, 1994.
- [101] C. Goze-Bac, M. Apostol, F. Rachdi and M. Mehring, *Phys. Rev. B* **52**, 51 (1995).
- [102] G. Zimmer, *Kernspinresonanzuntersuchungen zu Elektronischen and Dynamischen Eigenschaften von Alkalifulleriden*, Thesis, Universität Stuttgart, 1995.
- [103] C. Goze Bac, *Contribution a L'etude du Fullerene C60 et Derives: Etudes RMN et RPE*, Thesis, Universite Montpellier II, 1996.
- [104] C. Bower, S. Suzuki, K. Tanigaki and O. Zhou, *Appl. Phys. A* **67**, 47 (1998).
- [105] G. Gao, T. Çagin and W. A. Goddard, *Phys. Rev. Lett.* **80**, 5556 (1998).
- [106] O. Chauvet, G. Baumgartner, M. Carrard, W. Bacsa, D. Ugarte, W. A. d. Heer and L. Forró, *Phys. Rev. B* **53**, 13996 (1996).
- [107] L. Grigorian, K. Williams, S. Fang, G. Sumanasekera, A. Loper, E. Dickey, S. Pennycook and P. Eklund, *Phys. Rev. Lett.* **80**, 5560 (1998).
- [108] L. Grigorian, G. Sumanasekera, r. A. Lope, S. Fang, J. Allen and P. Eklund, *Phys. Rev. B* **58**, R4195 (1998).
- [109] R. J. Klingler, R. E. G. II, G. Sandía, C. S. Johnson, L. G. Scanlonb and J. W. Rathke, *J. Power Sources* **89**, 237 (2000).
- [110] L. Duclaux, *Carbon* **40**, 1751 (2002).
- [111] L. Duclaux, J. Salvetat, P. Lauginie, T. Cacciaguera, A. Fauge're, C. Goze-Bac and P. Bernier, *J. Phys. Chem. Solids* **64**, 571 (2003).
- [112] G. H. Jeong, A. A. Farajian, R. Hatakeyama, T. Hirata, T. Yaguchi, K. Tohji, H. Mizuseki and Y. Kawazoe, *Phys. Rev. B* **111**, 075410 (2003).

- [113] G. H. Jeong, R. Hatakeyama, T. Hirata, K. Tohji, K. Motomiya, T. Yaguchi and Y. Kawazoe, *Chem. Comm.*, 152 (2003).
- [114] G.-H. Jeong, A. A. Farajian, T. Hirata, R. Hatakeyama, K. Tohji, T. M. Briere, H. Mizuseki and Y. Kawazoe, *Thin Solid Films* **435**, 307 (2003).
- [115] X. Fan, E. C. Dickey, P. Eklund, K. A. Williams, L. Grigorian, R. Buczko, S. T. Pantelides and S. J. Pennycook, *Phys. Rev. Lett.* **84**, 4621 (2000).
- [116] M. Bockrath, J. Hone, A. Zettl, P. L. McEuen, A. G. Rinzler and R. E. Smalley, *Phys. Rev. B* **61** (2000).
- [117] T. Pichler, A. Kukovecz, H. Kuzmany and H. Kataura, *Synth. Met.* **135**, 717 (2003).
- [118] S. Suzuki, F. Maeda, Y. Watanabe and T. Ogino, *Phys. Rev. B* **67**, 115418 (2003).
- [119] J. R. Dahn, T. Zheng, Y. Liu and J. S. Xue, *Science* **270**, 590 (1995).
- [120] J. E. Fischer, *Acc. Chem. Res.* **35**, 1079 (2002).
- [121] N. Bendiab, A. Righi, E. Anglaret, J. L. Sauvajol, L. Duclaux and F. Béguin, *Chem. Phys. Lett.* **339**, 305 (2001).
- [122] N. Bendiab, L. Spina, A. Zahab, P. Poncharal, C. Marlière, J. L. Bantignies, E. Anglaret and J. L. Sauvajol, *Phys. Rev. B* **63**, 153407 (2001).
- [123] Z.-h. Yang and H.-q. Wu, *Solid State Ionics* **143**, 173 (2001).
- [124] E. C. T. Harley and L. E. McNeil, *J. Phys. Chem. Solids* **65**, 1711 (2004).
- [125] P. Petit, C. Mathis, C. Journet and P. Bernier, *Chem. Phys. Lett.* **305**, 370 (1999).
- [126] H. Shimoda, B. Gao, X. P. Tang, A. Kleinhammes, L. Fleming, Y. Wu and O. Zhou, *Phys. Rev. Lett.* **88**, 015502 (2002).
- [127] H. Shimoda, B. Gao, X. P. Tang, A. Kleinhammes, L. Fleming, Y. Wu and O. Zhou, *Physica B* **323**, 133 (2002).
- [128] G. Maurin, F. Henn, B. Simon, J. F. Colomer and J. B. Nagy, *Nano Lett.* **1**, 75 (2001).

- [129] F. Leroux, K. Metenier, S. Gautier, E. Frackowiak, S. Bonnamy and F. Beguin, *J. Power Sources* **81-82**, 317 (1999).
- [130] X. Liu, T. Pichler, M. Knupfer and J. Fink, *Phys. Rev. B* **67**, 125403 (2003).
- [131] C. Jo, C. Kim and Y. H. Lee, *Phys. Rev. B* **65**, 035420 (2002).
- [132] I. Mukhopadhyay, S. Kawasaki, F. Okino, A. Govindaraj, C. N. R. Rao and H. Touhara, *Physica B* **323**, 130 (2002).
- [133] H.-C. Shin, M. Liu, B. Sadanadan and A. M. Rao, *J. Power Sources* **112**, 216 (2002).
- [134] Z. Yang, Y. Zhou, S. Sang, Y. Feng and H. Wu, *Mater. Chem. Phys.* **89**, 295 (2005).
- [135] J. T. Ye, Z. M. Li, Z. K. Tang and R. Saito, *Phys. Rev. B* **67**, 113404 (2003).
- [136] S. Suzuki, Y. Watanabe, T. Ogino, S. Heun, L. Gregoratti, A. Barinov, B. Kaulich, M. Kiskinova, W. Zhu, C. Bower and O. Zhou, *J. Appl. Phys.* **92**, 7527 (2002).
- [137] M. Schmid, M. Mehring, S. Roth, P. Bernier and C. Goze-Bac, *Mater. Res. Soc. Symp. Proc.* **772**, M.3.4.1 (2003).
- [138] M. Schmid, C. Goze-Bac, M. Mehring, S. Roth and P. Bernier, ^{13}C NMR Investigations of the Metallic State of Li Intercalated Carbon Nanotubes, in *Electronic Properties of Novel Materials – Molecular Nanostructures*, H. Kuzmany, J. Fink, M. Mehring and S. Roth [eds.], volume 685, pages 131–134, Kirchberg, Austria, 2003, American Institute of Physics.
- [139] M. H. Cohen and F. Reif, Quadrupole Effects in Nuclear Magnetic Resonance Studies of Solids, in *Solid State Physics*, F. Seitz and D. Turnbull [eds.], volume 5, pages 321–438, New York, 2004, Academic Press.
- [140] M. Schmid, C. Goze-Bac, M. Mehring, S. Roth and P. Bernier, NMR on Cesium Intercalated Carbon Nanotubes, in *Electronic Properties of Novel Materials – Molecular Nanostructures*, H. Kuzmany, J. Fink, M. Mehring and S. Roth [eds.], volume 723, pages 181–184, Kirchberg, Austria, 2004, American Institute of Physics.

- [141] L. Petaccia, A. Goldoni, S. Lizzit and R. Larciprete, *J. Electron Spectrosc. Relat. Phenom.* **144-147**, 793 (2005).
- [142] J. Lu, S. Nagase, S. Zhang and L. Peng, *Phys. Rev. B* **69**, 205304 (2004).
- [143] H. J. Liu and C. T. Chan, *Solid State Commun.* **125**, 77 (2003).
- [144] Y. Liu, H. Yukawa and M. Morinaga, *Comp. Mat. Sci.* **30**, 50 (2004).
- [145] A. Udomvech, T. Kerdcharoen and T. Osotchan, *Chem. Phys. Lett.* **406**, 161 (2005).
- [146] A. A. Farajian, K. Ohno, K. Esfarjani, Y. Maruyama and Y. Kawazoe, *J. Chem. Phys.* **111**, 2164 (1999).
- [147] J. L. Yang, H. J. Liu and C. T. Chan, *Phys. Rev. B* **64**, 085420 (2001).
- [148] J. Choi, I. A. Samayoa, S. C. Lim, C. Jo, Y. C. Choi, Y. H. Lee and P. A. Dowben, *Phys. Lett. A* **299**, 601 (2002).
- [149] V. Meunier, J. Kephart, C. Roland and J. Bernholc, *Phys. Rev. Lett.* **88**, 075506 (2002).
- [150] T. Miyake and S. Saito, *Physica B* **323**, 219 (2002).
- [151] T. Miyake and S. Saito, *Phys. Rev. B* **65**, 165419 (2002).
- [152] X. Duan, B. Akdim and R. Pachter, *Appl. Surf. Sci.* **243**, 11 (2005).
- [153] J. W. Kang and H. J. Hwang, *Nanotechnology* **15**, 115 (2004).
- [154] J. W. Kang and H. J. Hwang, *J. Phys. Soc. Jpn.* **73**, 738 (2004).
- [155] V. Margulis, E. Muryumin and O. Tomilin, *Physica B* **353**, 314 (2004).
- [156] J. J. Zhao, J. Han and J. P. Lu, *Phys. Rev. B* **65**, 193401 (2002).
- [157] J. Zhao, A. Buldum, J. Han and J. P. Lu, *Phys. Rev. Lett.* **85**, 1706 (2000).
- [158] C. Garau, A. Frontera, D. Quinonero, A. Costa, P. Ballester and P. M. Deya, *Chem. Phys. Lett.* **374**, 548 (2003).
- [159] C. Garau, A. Frontera, D. Quinonero, A. Costa, P. Ballester and P. M. Deya, *Chem. Phys.* **297**, 85 (2004).

- [160] S. B. Fagan, S. Guerini, J. M. Filho and V. Lemos, *Microelectronics Journal* **36**, 499 (2005).
- [161] P. Petit, E. Jouguelet and C. Mathis, *Chem. Phys. Lett.* **318**, 561 (2000).
- [162] A. S. Claye, J. E. Fischer, C. B. Huffman, A. G. Rinzler and R. E. Smalley, *J. Electrochem. Soc.* **147**, 2845 (2000).
- [163] R. E. Gerald, J. Sanchez, C. S. Johnson, R. J. Klingler and J. W. Rathke, *J. Phys.: Condens. Matter* **13**, 8269 (2001).
- [164] F. Henn, G. Maurin, B. Simon, J. F. Colomer and J. B. Nagy, *Nano Lett.* **1**, 75 (2001).
- [165] Y.-O. Kim and S.-M. Park, *J. Electrochem. Soc.* **148**, A194 (2001).
- [166] Y. H. Lee, K. H. An, W. S. Kim, Y. S. Park, J.-M. Moon, D. J. Bae, S. C. Lim and Y. S. Lee, *Adv. Funct. Mat.* **11**, 387 (2001).
- [167] Z.-h. Yang and H.-q. Wu, *Chem. Phys. Lett.* **343**, 235 (2001).
- [168] G. Sandí, K. A. Carrado, R. E. Winans, C. S. Johnson and R. Csencsits, *J. Electrochem. Soc.* **146**, 3644 (1999).
- [169] Y. Jung, M. C. Suh, H. Lee, M. Kim, S. I. Lee, S. C. Shim and J. Kwak, *J. Electrochem. Soc.* **144**, 4279 (1997).
- [170] K. Moriguchi, Y. Itoh, S. Munetoh, K. Kamei, M. Abe, A. Omaru and M. Nagamine, *Physica B* **323**, 127 (2002).
- [171] S. Hayes, R. Guidotti, W. Even, P. Hughes and H. Eckert, *J. Phys. Chem. A* **107**, 3866 (2003).
- [172] G. X. Wang, J.-h. Ahn, J. Yao, M. Lindsay, H. K. Liu and S. X. Dou, *J. Power Sources* **119-121**, 16 (2003).
- [173] G. Maurin, C. Bousquet, F. Henn, P. Bernier, R. Almairac and B. Simon, *Chem. Phys. Lett.* **312**, 14 (1999).
- [174] K. Fredenhagen and G. Cadenbach, *Z. Anorg. Allg. Chem.* **158**, 249 (1926).
- [175] J. Kong, C. Zhou, E. Yenilmez and H. Daia, *Appl. Phys. Lett.* **77**, 3977 (2000).

- [176] T. Pichler, M. Sing, M. Knupfer, M. S. Golden and J. Fink, *Solid State Commun.* **109**, 721 (1999).
- [177] R. Lee, H. Kim, J. E. Fischer, A. Thess and R. E. Smalley, *Nature* **388**, 255 (1997).
- [178] S. Suzuki, C. Bower and O. Zhou, *Chem. Phys. Lett.* **285**, 230 (1998).
- [179] A. S. Claye, N. M. Nemes, A. Jánossy and J. E. Fischer, *Phys. Rev. B* **62**, R4845 (2000).
- [180] R. Saito, M. S. Dresselhaus and G. Dresselhaus, *Phys. Rev. B* **61**, 2981 (2000).
- [181] J. P. Issi, L. Langer, J. Heremans and C. H. Olk, *Carbon* **33**, 941 (1995).
- [182] R. Saito, M. Fujita, G. Dresselhaus and M. S. Dresselhaus, *Appl. Phys. Lett.* **60**, 2204 (1992).
- [183] P. Lambin, *Comptes Rendus Physique* **4**, 1009 (2003).
- [184] S. Ghosh, P. V. Teredesai and A. K. Sood, *Pure Appl. Chem.* **74**, 1719 (2002).
- [185] J. W. G. Wilder, L. C. Venema, A. G. Rinzler, R. E. Smalley and C. Dekker, *Nature* **391**, 59 (1998).
- [186] M. Bockrath, D. H. Cobden, J. Lu, A. G. Rinzler, R. E. Smalley, L. Balents and P. L. McEuen, *Nature* **397**, 598 (1999).
- [187] K. Schönhammer, *J. Phys.: Condens. Matter* **14**, 12783 (2002).
- [188] J. Voit, *Rep. on Prog. in Phys.* **58**, 977 (1995).
- [189] N. . Nygard, D. H. Cobden, M. Bockrath, P. L. McEuen and P. E. Lindelof, *Appl. Phys. A* **69**, 297 (1999).
- [190] H. Yoshioka, *J. Phys. Chem. Solids* **63**, 1281 (2002).
- [191] H. Ishii, H. Kataura, H. Shiozawa, H. Yoshioka, H. Otsubo, Y. Takayama, T. Miyahara, S. Suzuki, Y. Achiba, M. Nakatake, T. Narimura, M. Higashiguchi, K. Shimada, H. Namatame and M. Taniguchi, *Nature* **426**, 540 (2003).
- [192] H. Rauf, T. Pichler, M. Knupfer, J. Fink and H. Kataura, *Phys. Rev. Lett.* **93**, 096805 (2004).

- [193] X.-P. Tang, A. Kleinhammes, H. Shimoda, L. Fleming, K. Y. Bennoune, S. Sinha, C. Bower, O. Zhou and Y. Wu, *Science* **288**, 492 (2000).
- [194] C. Goze-Bac, P. Bernier, S. Latil, V. Jourdain, A. Rubio, S. H. Jhang, S. W. Lee, Y. W. Park, M. Holzinger and A. Hirsch, *Curr. Appl. Phys.* **1**, 149 (2001).
- [195] C. Goze-Bac, S. Latil, L. Vaccarini, P. Bernier, P. Gaveau, S. Tahir, V. Micholet, R. Aznar, A. Rubio, K. Metenier and F. Beguin, *Phys. Rev. B* **63**, 100302 (2001).
- [196] S. Latil, C. Goze-Bac, L. Henrard, P. Bernier and A. Rubio, *Phys. Rev. Lett.* **86**, 3160 (2001).
- [197] S. Hayashi, F. Hoshi, T. Ishikura, M. Yumura and S. Ohshima, *Carbon* **41**, 3047 (2003).
- [198] H. Geng, X. Zhang, S. Mao, A. Kleinhammes, H. Shimoda, Y. Wu and O. Zhou, *Chem. Phys. Lett.* **399**, 109 (2004).
- [199] A. Kitaygorodskiy, W. Wang, S.-Y. Xie, Y. Lin, K. A. S. Fernando, X. Wang, L. Qu, B. Chen and Y.-P. Sun, *J. Am. Chem. Soc.* **127**, 7517 (2005).
- [200] K. Lee, K. Kang, B. Mean, M. Lee, J.-K. Jung, K.-S. Ryu and Y. Hee Lee, *Physica B* **359-361**, 1412 (2005).
- [201] M. Schmid, S. Krämer, M. Mehring, S. Roth, M. Haluska and P. Bernier, Hydrogen in Fragmented Carbon Nanotubes: ^1H -NMR, in *Electronic Properties of Novel Materials – Molecular Nanostructures*, H. Kuzmany, J. Fink, M. Mehring and S. Roth [eds.], volume 591, pages 598–601, Kirchberg, Austria, 2001, American Institute of Physics.
- [202] M. Schmid, C. Goze-Bac, S. Krämer, M. Mehring, S. Roth and P. Bernier, NMR Investigations of Hydrogen in Carbon Nanotubes, in *Electronic Properties of Novel Materials – Molecular Nanostructures*, H. Kuzmany, J. Fink, M. Mehring and S. Roth [eds.], volume 633, pages 593–596, Kirchberg, Austria, 2002, American Institute of Physics.
- [203] A. Kleinhammes, S.-H. Mao, X.-J. Yang, X.-P. Tang, H. Shimoda, J. P. Lu, O. Zhou and Y. Wu, *Phys. Rev. B* **68**, 075418 (2003).
- [204] M. Schmid, S. Krämer, C. Goze-Bac, M. Mehring, S. Roth and P. Bernier, *Synth. Met.* **135**, 727 (2003).

- [205] I. Yu, J. Lee and S. Lee, *Physica B: Condensed Matter* **329-333**, 421 (2003).
- [206] T. Pietrass and K. Shen, *J. Phys. Chem. B* **108**, 9937 (2004).
- [207] K. Fu, H. Li, B. Zhou, A. Kitaygorodskiy, L. F. Allard and Y.-P. Sun, *J. Am. Chem. Soc.* **126**, 4669 (2004).
- [208] K. Shen and T. Pietraß, *Appl. Phys. Lett.* **84**, 1567 (2004).
- [209] S. Latil, *Le Magnétisme Des Nanotubes: Une Approche Théorique*, Thesis, Université Montpellier II, 2001.
- [210] J. Mintmire and C. White, *Appl. Phys. A* **67**, 65 (1998).
- [211] N. Bendiab, E. Anglaret, J.-L. Bantignies, A. Zahab, J. L. Sauvajol, P. Petit, C. Mathis and S. Lefrant, *Phys. Rev. B* **64**, 245424 (2001).
- [212] J.-L. Sauvajol, N. Bendiab, E. Anglaret and P. Petit, *Comptes Rendus Physique* **4**, 1035 (2003).
- [213] F. Beguin, H. Estrade-Szwarckopf, J. Conard, P. Lauginie, P. Marceau, D. Guerard and L. Facchini, *Synth. Met.* **7**, 77 (1983).
- [214] M. Inagaki and O. Tanaïke, *Carbon* **39**, 1083 (2001).
- [215] C. Herold, A. Herold and P. Lagrange, *Solid State Sciences* **6**, 125 (2004).
- [216] P. Lauginie, *Statut de L'électron de Conduction dans les Composés d'intercalation Graphite-Metal Alcalin: Le dit de la Résonance Magnétique*, Thesis, University of Paris-Sud, centre d'Orsay, 1988.
- [217] J. Charlier, T. W. Ebbesen and P. Lambin, *Phys. Rev. B* **53**, 11108 (1996).
- [218] H. J. Choi, J. Ihm, S. G. Louie and M. L. Cohen, *Phys. Rev. Lett.* **84**, 2917 (2000).
- [219] A. J. Lu and B. C. Pan, *Phys. Rev. Lett.* **92**, 105504 (2004).
- [220] S. Burnet, T. Yonezawa and J. J. v. d. Klink, *J. Phys.: Condens. Matter* **14**, 7135 (2002).
- [221] A. J. Cox, J. G. Louderback and L. A. Bloomfield, *Phys. Rev. Lett.* **71**, 923 (1993).

- [222] A. J. Cox, J. G. Louderback, S. E. Apsel and L. A. Bloomfield, *Phys. Rev. B* **49**, 12295 (1994).
- [223] F. Simon, Talk at IWEPNM'05, Kirchberg, Austria, 2005.
- [224] P. Delaney, H. J. Choi, J. Ihm, S. G. Louie and M. L. Cohen, *Nature* **391**, 466 (1998).
- [225] E. Durgun, S. Dag, S. Ciraci and O. Gulseren, *J. Phys. Chem. B* **108**, 575 (2004).
- [226] T. Pichler, Talk at IWEPNM'05, Kirchberg, Austria, 2005.
- [227] M. Ichida, S. Mizuno, Y. Tani, Y. Saito and A. Nakamura, *J. Phys. Soc. Jpn.* **68**, 3131 (1999).
- [228] K. Tatsumi, J. Conard, M. Nakahara, S. Menu, P. Lauginie, Y. Sawada and Z. Ogumi, *Chem. Comm.* **7**, 687 (1997).
- [229] J. Conard, From Intercalation Compounds to Inserted Clusters: Li in Carbon Superanodes for Secondary Batteries, in *New Trends in Intercalation Compounds for Energy Storage*, C. Julien, J. Pereira-Ramos and A. Momchilov [eds.], pages 63, Kluwer Academic Publishers, 2002.
- [230] A. G. Anderson and A. G. Redfield, *Phys. Rev.* **116**, 583 (1959).
- [231] P. Yu, B. N. Popov, J. A. Ritter and R. E. White, *J. Electrochem. Soc.* **146**, 8 (1999).
- [232] C. A. Vincent, *Chem. Br.* **25**, 391 (1989).
- [233] M. Armand, *Adv. Mater. (Weinheim, Fed. Repub. Ger.)* **2**, 278 (1990).
- [234] H. S. Gutowsky and B. R. McGarvey, *J. Chem. Phys.* **20**, 1472 (1952).
- [235] B. R. McGarvey and H. S. Gutowsky, *J. Chem. Phys.* **21**, 2114 (1953).
- [236] H. Estrade-Szwarckopf, B. Rousseau, M. Malki, P. Lauginie, J. Conard, P. Lagrange and D. Guerard, *Synth. Met.* **12**, 401 (1985).
- [237] B. W. Smith, M. Monthieux and D. E. Luzzi, *Chem. Phys. Lett.* **315**, 31 (1999).
- [238] K. Hirahara, K. Suenaga, S. Bandow, H. Kato, T. Okazaki, H. Shinohara and S. Iijima, *Phys. Rev. Lett.* **85**, 5384 (2000).

- [239] M. Hodak and L. A. Girifalco, *Phys. Rev. B* **67**, 075419 (2003).
- [240] D. J. Hornbaker, S.-J. Kahng, S. Misra, B. W. Smith, A. T. Johnson, E. J. Mele, D. E. Luzzi and A. Yazdani, *Science* **295**, 828 (2002).
- [241] C. L. Kane, E. J. Mele, A. T. Johnson, D. E. Luzzi, B. W. Smith, D. J. Hornbaker and A. Yazdani, *Phys. Rev. B* **66**, 235423 (2002).
- [242] K. Lee, K. H. Kang, B. J. Mean, M. Lee, J.-K. Jung, K.-S. Ryu and Y. Hee Lee, *Physica B* **359-361**, 1412 (2005).

List of Figures

1.1	Structural transition from graphene to SWNT	2
1.2	Graphene structure with wrapping vector	3
1.3	Schematics of a zigzag, armchair and chiral SWNT	3
1.4	SEM of SWNT bundles	5
1.5	Energy dispersion relation of graphene	7
1.6	Electronic density of states	9
1.7	GIC staging sequences	11
2.1	MAT pulse sequence	15
2.2	Transferred hyperfine coupling	18
2.3	sp^2 -hybridization	20
2.4	Spin echo pulse sequence	24
2.5	Quadrupolar echo amplitudes	25
2.6	^{13}C MAS and static NMR spectra of SWNT	36
2.7	^{13}C proton decoupled MAS spectrum of purified SWNT	38
2.8	Deconvolution of ^{13}C 126 ppm isotropic SWNT line	39
2.9	SWNT CSA tensor	40
3.1	^{13}C NMR spectra of intercalated SWNT	43
3.2	^{13}C NMR CSA tensor components	44
3.3	^{13}C NMR isotropic shifts	44
3.4	^{13}C NMR magnetization recovery for LiC_6	47
3.5	^{13}C NMR spin lattice relaxation rates for LiC_x	47
3.6	^7Li NMR spectrum of LiC_{10}	54
3.7	^7Li NMR spectra evolution during magnetization recovery	55
3.8	^7Li NMR $1/T_1$ relaxation rate of LiC_{10}	58
3.9	^1H NMR spectra of LiC_7	60
3.10	Ratio of broad and narrow ^1H NMR line	61
3.11	^1H NMR $1/T_1$ relaxation rate of LiC_7	63
3.12	THF-rotation in graphite	65
3.13	SWNT-Li-THF configuration	66
4.1	^{13}C NMR spectra of pristine SWNT and CsC_8 before annealing	74
4.2	^{13}C NMR spectra of Cs intercalated SWNT	75
4.3	2D- ^{13}C NMR spectrum, pristine SWNT	77

4.4	Isotropic ^{13}C NMR spectrum, pristine SWNT	78
4.5	2D- ^{13}C NMR spectrum, CsC_{30}	79
4.6	Isotropic ^{13}C NMR spectrum, CsC_{30}	79
4.7	Stoichiometry dependence of $1/T_{1b}$ fraction	80
4.8	^{13}C NMR, temperature dependence of spin-lattice relaxation for CsC_8	82
4.9	$n(\varepsilon_F)$ for various samples CsC_x	83
4.10	^{133}Cs NMR nutation for CsC_{30}	85
4.11	^{133}Cs NMR $\pi/2 - \beta$ experiment for CsC_{30}	86
4.12	^{133}Cs NMR spectra	87
4.13	α -line FWHM temperature dependence	88
4.14	^{133}Cs NMR spectrum of CsC_{31} at $T = 100$ K	89
4.15	$1/T_2^\alpha$ temperature dependence	91
4.16	$1/T_1^\alpha$ temperature dependence	91
4.17	^{133}Cs NMR spectrum of CsC_8 at $T = 40$ K	94
4.18	Symmetrized ^{133}Cs NMR spectrum of CsC_8 at $T = 130$ K, β -line . . .	95
4.19	Second moment of CsC_8 vs. temperature, β -line	96
4.20	$1/T_1^\beta$ temperature dependence	97
4.21	^{133}Cs NMR $1/T_2$ relaxation, β -line	99
4.22	^{133}Cs NMR $1/T_1^{stim}$ relaxation, β -line	101
4.23	Scalar spin-spin coupling	102
4.24	Temperature dependence of ^{133}Cs NMR line positions	103
4.25	Schematics, structural simulation of Cs-SWNT CsC_8	105

List of Tables

2.1	Quadrupolar spin signal parameters	22
2.2	Quadrupolar echo positions	26
2.3	Stimulated echo phase cycling scheme	35
3.1	Shift values for LiC_x	46
3.2	CSA tensor analysis for LiC_x	52
3.3	Ratios of α and β sites in LiC_x	57

Lebenslauf

Name: Michael Schmid
Geburtsdatum: 27.04.1974
Geburtsort: Horb-Mühlingen
Eltern: Klaus-Peter Schmid und Ruth Schmid, geb. Pfrommer
Familienstand: verheiratet seit 10. Oktober 2003

Schulbildung:

1981 – 1985 Grundschule Murr
1985 – 1994 Otto-Hahn-Gymnasium, Ludwigsburg
Juni 1994 Abitur

Zivildienst:

1994 – 1995 NABU-Landesgeschäftsstelle in Kornwestheim

Wissenschaftliche Ausbildung:

1995 – 2001 Physikstudium an der Universität Stuttgart
1997 – 2000 Tätigkeit als wissenschaftliche Hilfskraft
am Max-Planck Institut Stuttgart
2001 Studienabschluss, Diplomarbeit “Untersuchungen an Wasserstoff
in Carbon Nanotubes: $^1\text{H-NMR}$ ”
2001 – 2005 Dissertation am 2. Physikalischen Institut
der Universität Stuttgart,
davon ein Jahr Forschungsaufenthalt
in Montpellier, Frankreich

Danksagung. . .

Ich möchte mich bei allen sehr herzlich bedanken, die zum Gelingen dieser Arbeit beigetragen haben. Ein besonderer Dank geht dabei an

- Herrn Prof. Dr. M. Mehring. Sie haben es ermöglicht, durch viele sehr beeindruckende Diskussionen und Anregungen diesem Projekt zu einem Erfolg zu verhelfen.
- Herrn Dr. habil. S. Roth für die Aufnahme am Max-Planck-Institut. Viele Gespräche haben fruchtbare und motivierende Ideen hervorgebracht. Insbesondere möchte ich mich auch für die finanzielle Unterstützung auf den vielen Reisen und der Ermöglichung der Zusammenarbeit mit der Universität Montpellier bedanken!
- Herrn Dr. C. Goze-Bac für die Kooperation und Hilfsbereitschaft. Du hast es durch Deine humorvolle Art immer wieder geschafft, unsere gemeinsame Arbeit motiviert voranzutreiben!
- Herrn Prof. Dr. H. Schweizer für die Übernahme des Mitberichtes.
- Frau U. Offenbeck für die stete Freundlichkeit und Herzlichkeit. Es ist schön jeden Morgen einem lächelnden Menschen zu begegnen...
- Herrn A. Heidebrecht für eine schöne gemeinsame Zeit im Labor, sowie die immer wieder imponierenden Gespräche auf allen Gebieten der Physik.
- Herrn Dr. S. Krämer, der mich insbesondere zu Beginn dieser Arbeit mit großem Fleiß und Eifer bei den Experimenten unterstützt hat.
- meine jetzigen und früheren Kollegen am 2. Physikalischen Institut, insbesondere Dr. A. Grupp, Dr. S. Knorr, Dr. H.-J. Kümmerer, Dr. J. Mende, H. Neumann, Prof. Dr. H. Paus, Dr. J. Rahmer und Dr. W. Scherer.
- meine Kollegen des MPI ("4C11"), insbesondere J. Chech, Dr. U. Dettlaff, Dr. M. Haluska, Dr. J. Meyer, J. Muster, D. Obergfell, S. Sahakalkan, M. Schmid, V. Siegle und Prof. Dr. V. Skakalova. Ein spezielles Dankeschön geht an das Team von B. Hornbostel und M. Kaempgen, die mit ihrem fröhlichen Charakter immer wieder für eine heitere Atmosphäre im Laboralltag gesorgt haben.
- meine Kollegen des LCVN Montpellier.
- die Mitarbeiter der mechanischen und der glastechnischen Werkstatt der Universität Stuttgart.

- die Mitarbeiter der Tieftemperatur-Abteilung, insbesondere Herrn J. Maurer für die vielen entspannenden Gespräche während dem Füllen unserer “Dicken Berta”.
- meine Eltern, denn Ihr habt mir durch Eure starke Unterstützung diese Arbeit ermöglicht.
- meine Frau Teresa für ihre Liebe, der Toleranz und ihrem Verständnis dafür, dass sie mich in den vergangenen Jahren oft aufgrund meiner Forschungstätigkeit entbehren musste.

